

NATIONAL & INTERNATIONAL SCIENTIFIC EVENTS

17th World Conference on Continuing Engineering Education (IACEE 2020)

Venue: NTNU Campus
Location: Trondheim, Norway

Begins: May 26, 2020
Ends: May 29, 2020

14th Mediterranean Congress of Chemical Engineering

Venue: Gran Via Venue
Location: Barcelona, Spain

Begins: June 2, 2020
Ends: June 5, 2020

34th European Composite Materials Congress

Venue: Viking Line Terminal
Location: Stockholm, Sweden

Begins: June 9, 2020
Ends: June 11, 2020

The 49th International Congress and Exposition on Noise Control Engineering

Venue: Convention and Exhibition Center
Location: Seoul, Korea

Begins: August 23, 2020
Ends: August 26, 2020

36th European and 12nd International Peptide Symposium

Venue: Hotel Meliá Sitges
Location: Barcelona, Spain

Begins: August 30, 2020
Ends: September 04, 2020

FISITA World Congress 2020

Venue: O₂ Universum
Location: Prague, Czech Republic

Begins: September 14, 2020
Ends: September 18, 2020

14th International Conference on Hydrosience and Engineering

Venue: Radisson Blu Resort & Spa
Location: Cesme, Turkey

Begins: September 22, 2020
Ends: September 25, 2020

46th Annual Conference of the IEEE Industrial Electronics Society-IECON 2020

Venue: Marina Bay Sands Expo and Convention Centre
Location: Malaysia

Begins: October 18, 2020
Ends: October 21, 2020

23rd International Conference on Electrical Machines and Systems (ICEMS2020)

Venue: ACT CITY Hamamatsu
Location: Hamamatsu, Japan

Begins: November 24, 2020
Ends: November 27, 2020

73rd Annual Session of Indian Institute of Chemical Engineers (CHEMCON2020)

Venue: Institute of Minerals & Materials Technology
Location: Bhubaneswar, India

Begins: December 27, 2020
Ends: December 30, 2020

39th IEEE International Conference on Consumer Electronics (ICCE 2021)

Location: Las Vegas, USA

Begins: January 10, 2021
Ends: January 12, 2021

8th International Conference on Geological and Civil Engineering (ICGCE 2021)

Location: Tokyo, Japan

Begins: January 28, 2021
Ends: January 30, 2021

HITTITE

JOURNAL OF SCIENCE & ENGINEERING

HJSE Official Journal of Hitit University Volume 7, Issue 1, 2020 www.hjse.hitit.edu.tr



HJSE Official Journal of Hitit University Volume 7, Issue 1, 2020 www.hjse.hitit.edu.tr



Abstracted & Indexed in:

TR Dizin Mühendislik ve Temel Bilimler Veri Tabanı | CrossRef | Google Scholar | MIP Database | StuartxChange | ResearchBib | Scientific Indexing Services (SIS)

HITTITE

Volume 7, Issue 1, 2020

www.hjse.hitit.edu.tr

The Influence of Grinding Parameters of Talc on Water-Based Paint Properties: Application of Multivariate Regression Analysis 01-06

Murat Muduroglu, Muhammed Fatih Can and Baris Ergul

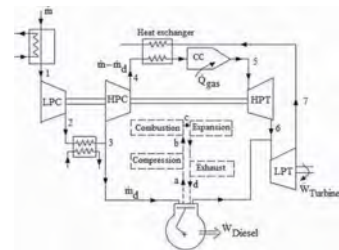
In this study, the influence of grinding parameters of talc sample in the conventional ballmill on water-based paint properties was investigated, and the results obtained from the experiments were statistically modeled.



Thermodynamic Analysis of Effects of the Inlet Air Cooling on Cycle Performance in Combined Brayton-Diesel Cycle 07-16

Betül Sarac and Teoman Ayhan

In the present study, the effects of inlet air cooling on compound cycle performance in a diesel gas turbine engine system where waste heat is used in the composite power system in the sustainable energy system were investigated thermodynamically.



Comparison of Thermal Performance of Newly Produced Lightweight Wall and Roof Elements for Energy-efficient Buildings 17-26

Hasan Oktay, Recep Yumrutas and Zeki Argunhan

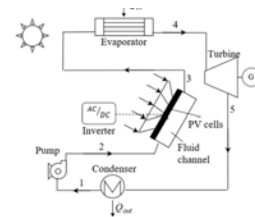
In this study, both experimental and theoretical investigations are performed to obtain new concrete types with high thermal insulating characteristics for energy-efficient buildings.



Using the Low Concentrated Photovoltaic Module as a Preheater in an Organic Rankine Cycle 27-33

Burak Kursun

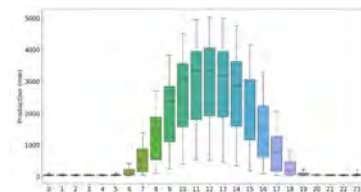
In this study, the effect of using a low concentrating photovoltaic thermal system as a preheater before the evaporator in the organic Rankine cycle (ORC) was investigated.



Solar Power Prediction with an Hour-based Ensemble Machine Learning Method 35-40

Seyda Ertekin

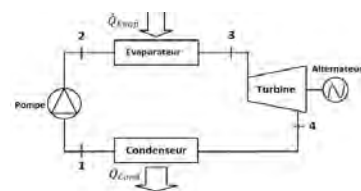
In this study we proposed an ensemble method which gives competitive prediction performance for solar power production.



An Energy Investigation of An Organic Rankine Cycle Utilizing Three Organic Fluids 41-44

Rabah Touaibi, Hasan Koten and Ozlem Boydak

This study presents an energy study of an Organic Rankine Cycle (ORC) by comparing three organic fluids.



The Influence of Grinding Parameters of Talc on Water-Based Paint Properties: Application of Multivariate Regression Analysis 45-49

Gulcin Alp Avci, Emre Avci, Gizem Ozluk Cilak and Sule Coskun Cevher

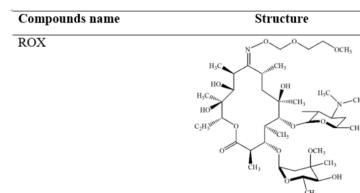
In this study, the ethanol and water (ultra-pure) extracts of galangal and ginger are used to determine the antimicrobial and antioxidant properties.



Stress Degradation Studies of Macrolide Antibiotics "Roxithromycin, Tilmicosin and Tylosin" by Using HPLC 51-54

Bediha Akmese

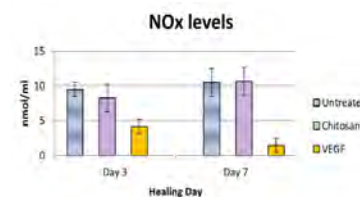
In this study, the degradation pro-files of macrolide antibiotics "roxithromycin (ROX), tilmicosin (TIL) and tylosin (TYL)" under varied stress conditions were investigated.



Some Serum Oxidative Parameters in Normoglycemic Rats: Vascular Endothelial Growth Factor (VEGF) Application 55-59

Kaan Kaltalioglu and Sule Coskun Cevher

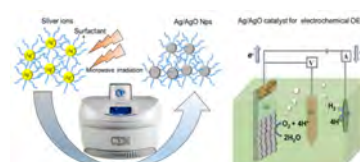
In this study, the effect of VEGF application on some serum parameters during wound healing process were investigated.



Microwave Assisted Green Synthesis of Ag/AgO Nanocatalyst as An Efficient OER Catalyst in Neutral Media 61-65

Gokhan Elmaci

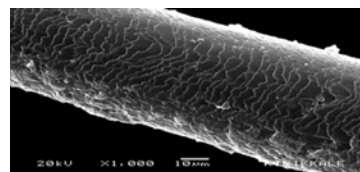
Here, a robust and highly stable, silver oxide based electrocatalyst composite system for the Efficient Oxygen Evolution Reaction (OER) was presented.



Hair Morphology Examination of Badger Meles Meles (L., 1758) in Turkey By Using Light And Scanning Electron Microscopes 67-72

Didem Atasever and Nahit Pamukoglu

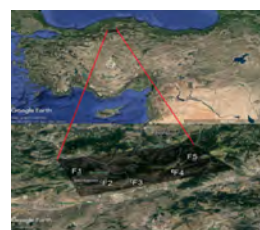
In this study, the hairs of the badger (Meles meles) in the collection and various museums were examined and was tried to determine whether there were variations.



Inventory of Large Mammal Species in the Ilgaz Mountains (Cankiri): A Major Ecological Corridor in Anatolia 73-80

Burak Akbaba and Safak Bulut

We located and identified the species of large mammals in the Ilgaz Mountains, as well as specific habitats used by them.



Owner

Prof. Dr. Ali Osman ÖZTÜRK
on behalf of Hitit University

Editor-in-chief

Prof. Dr. Ali KILIÇARSLAN

Associate Editors

Prof. Dr. D. Ali KÖSE
Assist. Prof. Dr. Öncü AKYILDIZ

Production

Assoc. Prof. Dr. Kazım KÖSE
Mustafa Reşit HABOĞLU
Erhan ÇETİN
Tugrul YILDIRIM
Harun Emre KIRAN
Ömer Faruk TOZLU

Editor's Office

Tel: +90 364 227 45 33 / 12 36

Fax: +90 364 227 45 35

Email: alikilicarslan@hitit.edu.tr

Subscription Service:

Tel: +90 364 227 45 33 / 12 82

Fax: +90 364 227 45 35

Email: hjse@hitit.edu.tr

EDITORIAL BOARD

Prof. Dr. İftikhar AHMAD

Prof. Dr. Mike BECKETT

Prof. Dr. İbrahim DİNÇER

Prof. Dr. Ali ELKAMEL

Prof. Dr. Mohamad S QATU

Prof. Dr. Saffa RIFFAT

Prof. Dr. Thanos SALIFOĞLU

Assoc. Prof. Dr. Yuehong SU

Dr. Wojciech NOGALA

Prof. Dr. Yusuf AYVAZ

Prof. Dr. Adil DENİZLİ

Prof. Dr. Ali GENÇER

Prof. Dr. Metin GÜRÜ

Prof. Dr. Murat HOŞÖZ

Prof. Dr. Sadık KAKAÇ

Prof. Dr. Tarık Ömer OĞURTANI

Prof. Dr. Ender SUVACI

Assoc. Prof. Dr. Ali TOPÇU

Prof. Dr. Kazım Savaş BAHÇECİ

Assoc. Prof. Dr. Cengiz BAYKASOĞLU

Prof. Dr. Naki ÇOLAK

Prof. Dr. Vedat DENİZ

Prof. Dr. Hakan GÜNGÜNEŞ

Prof. Dr. Bülent KABAK

Prof. Dr. Ali KILIÇARSLAN

Prof. Dr. Dursun Ali KÖSE

Prof. Dr. İrfan KURTBAŞ

Prof. Dr. İbrahim SÖNMEZ

Assoc. Prof. Dr. Seyfi ŞEVİK

Prof. Dr. Dilber Esra YILDIZ

University of Malakand, Chakdara, Pakistan

Bangor University, Bangor, United Kingdom

Uoit Ontario University, Ontario, Canada

University of Waterloo, Ontario, Canada

Central Michigan University, Michigan, United States

The University of Nottingham, United Kingdom

Aristotle University of Thessaloniki, Thessaloniki, Greece

The University of Nottingham, United Kingdom

Polish Academy of Sciences, Poland

Suleyman Demirel University, Turkey

Hacettepe University, Turkey

Ankara University, Turkey

Gazi University, Turkey

Kocaeli University, Turkey

TOBB University, Turkey

Middle East Technical University, Turkey

Anadolu University, Turkey

Hacettepe University, Turkey

Hitit University, Turkey

Hitit University, Turkey

Hitit University, Turkey

Hitit University, Turkey

Hitit University, Turkey

Hitit University, Turkey

Hitit University, Turkey

Hitit University, Turkey

Hitit University, Turkey

Hitit University, Turkey

Hitit University, Turkey

Hitit University, Turkey

| | |
|----------------------|--|
| Journal Name | : HITTITE JOURNAL OF SCIENCE AND ENGINEERING |
| Year | : 2020 |
| Managing Editor | : Prof. Dr. Ali KILIÇARSLAN |
| Managing Office | : Hitit University Faculty of Engineering |
| Managing Office Tel | : +90 364 227 45 33 / 12 36 |
| Publication Language | : English |
| Publication Type | : Peer Reviewed, Open Access, International Journal |
| Delivery Format | : 4 times a year (quarterly) |
| Print ISSN | : 2149-2123 |
| Online ISSN | : 2148-4171 |
| Publisher Address | : Hitit Üniversitesi Kuzey Kampüsü Çevre Yolu Bulvarı 19030 Çorum / TÜRKİYE |
| Publisher Tel | : +90 364 227 45 33/1236 |



This new issue of Hittite Journal of Science and Engineering contains twelve manuscripts from the disciplines of chemistry, biology, mining engineering, computer engineering and mechanical engineering. These manuscripts was first screened by Section Editors using plagiarism prevention software and then reviewed and corrected according to the reviewer's comments. I would like to express my gratitude to all our authors and contributing reviewers of this issue.

I would like to thank to the new President of Hitit University, Prof. Dr. Ali Osman Öztürk, for his support and interest in HJSE and also to the

Associate Editors of HJSE, namely Prof. Dr. Dursun Ali Köse and Asst. Prof. Dr. Öncü Akyıldız, as well as our Production Editors Dr. Kazım Köse, Mustafa Reşit Haboğlu, Erhan Çetin, Harun Emre Kıran and Ömer Faruk Tozlu for their invaluable efforts in making of the journal.

It's my pleasure to invite the researchers and scientists from all branches of science and engineering to join us by sending their best papers for publication in Hittite Journal of Science and Engineering.

Dr. Ali Kılıçarslan

Editor-in-Chief

The Influence of Grinding Parameters of Talc on Water-Based Paint Properties: Application of Multivariate Regression Analysis

Murat Muduroglu¹, Muhammed Fatih Can¹  Baris Ergul² 

¹Afyon Kocatepe University, Department of Mining Engineering, Afyon, Turkey

²Eskisehir Osmangazi University, Department of Statistics, Eskisehir, Turkey

ABSTRACT

In this study, the influence of grinding parameters of talc sample in the conventional ball mill on water-based paint properties was investigated, and the results obtained from the experiments were statistically modeled. The regression analysis were designed to reveal the correlation between grinding parameters of the talc and the opacity and brightness of the paint with the recipes containing prepared mineral. In multivariate regression analysis, the differential grinding parameters were used to determine the change on opacity and brightness of the paint with a linear model between the change of the grinding parameters as the variables. Therefore, developed analysis includes a numerical model which could foresee the changes on final paint properties due to parameter changes (ball charge, material charge and time) in the grinding process. At the end of the experimental studies, the results indicated that the changes on brightness and opacity of a water-based paint are very dependant to the characteristics of talc mineral used as a filler in the same recipe. In other words, it was possible to foresee the changes on opacity and brightness of the paint due to changing grinding parameters of talc used as mineral filler in paint by using multivariate multiple regression analysis.

Keywords:

Talc, Grinding, Grinding parameters, Paint, Opacity (OP), Brightness (BR), Multivariate regression analysis (MRA), Modeling.

Article History:

Received: 2019/07/12

Accepted: 2020/02/08

Online: 2020/03/26

Correspondence to: Muhammed Fatih Can, Afyon Kocatepe University, Mining Engineering Department, Afyon, Turkey
Tel: +90 533 460 40 09
E-Mail:mfcan@aku.edu.tr

INTRODUCTION

Coating applied for coloring material or protection purpose is called as paint. Besides their coloring feature paints have also hidden and protective properties. Colorless binder and solvent composition specially applied on wooden materials are called lacquer (Yurekli, 1997, Paksoy, 1999).

There are many raw materials used in paint production. These raw materials can be classified under 4 main groups as; binders, solvents, pigments/mineral fillers, and additives. Industrial minerals/mineral fillers have a significant role in paint production and can be used up to 50% in a typical water-based paint formula. Mineral fillers are widely used in paper, coating, and paint industries in order to enhance the properties of the final product by decreasing the production costs. In the paint industry the pigments are utilized with fillers, and both are in very fine size and required to be extensively dispersed in the paint. The mineral ingredients have active roles in the paint layer formation, strength, durability, OP, and color of the final coating (Conceição

et al., 2018). Several minerals and the chemical process should be applied to industrial minerals before their use in paint recipes. TiO₂, calcium carbonate (natural & precipitated), zinc oxide, kaolinite (natural & calcined), talc, mica, quartz, dolomite, and barite are main raw materials used in the paint (Ciullo, 1996). Moreover, the mineral fillers are known to provide some unique coating characteristics, in terms of, providing OP, the balance of BR, better surface finish and ease at application (Conceição et al., 2018). Additionally, they help to reduce production/recipe cost. Despite being at the sixth row in paint production in Europe, Turkey imports most of the fillers and additives (Karakas, 2011).

Talc is a hydromagnesium silicate, Mg₃(Si₂O₅)₂(OH)₂ and commonly used as a mineral filler in the paint industry (State Planning Organization, SPO, 2001). Ideally, it consists of 31.7% MgO, 63.5% SiO₂, and 4.8% water (Grim, 1968). Talc can reduce the settling ratio of pigment together with the positive effect on OP in the paint. Blistering and cleavages in a paint can also be elimina-

ted by using talc. It inhibits moisture transfer to the material, and increases the corrosion resistance of the paint due to a platy form of talc. Talc is also used in primer coatings due to better adherence property compared to other fillers. However, it is not recommended to use talc over a certain amount in a recipe because of its high dusting characteristics (Gündüz, 2005).

The performance of talc in painting depends on its physical characteristics such as particle morphology, particle size distribution, and oil absorption (Yekeler et al., 2004). These characteristics directly affect the interactions between mineral particles and other raw materials in paint, and hence the properties of the paint are changed. Talc is crushed and ground to obtain proper micron size before used in paint recipes. Grinding is generally performed in ball mills. Paint producers' demand for the homogeneous product (Conceição et al., 2018). Within water based coatings, talc has a satisfying performance with sustainable raw material quality. However, this quality may vary as the talc suppliers utilize different set ups for liberating/comminution processes. This leads talc products with different characteristics to be obtained upon different grinding parameters and the use of these different talc products in the paint may deteriorate the permanence of paint quality in industrial production line.

Generally, regression analysis and response surface methods are applied in literature. The basic principle of the response surface is a polynomial relationship between control and response variables (Bezerra et al., 2008). In some advanced cases, models at second-order fit better and cubic terms can be used for complex cases. The response surface data have been digitized with a regression model to form a response surface (Box and Hunter, 1961; Bezerra et al., 2008). Moreover, Bootstrap, Bayesian and Ordinary Least Squares are also valid methods to estimate the parameters of the model methods (Wold, 1973; Wold, et al., 2001).

In this context, the aim of this study was to investigate the correlation between grinding parameters of the talc and the physical properties (OP and BR) of the paint with the recipes containing prepared mineral.

The results obtained from the grinding experiments were also statistically modeled. The regression analysis was designed to reveal the correlation between the grinding parameters of the talc and the final properties of the paint. In MRA, the differential grinding parameters were used to determine the change on OP and BR of the paint with a linear model between the change of the grinding parameters as the variables.

MATERIAL AND METHODS

Material

The raw sample of talc used in this study was supplied from the Sivas region of Turkey.

The chemical analysis of the sample was done by using Bruker S8 Tiger model X-ray floresans (XRF) spectrophotometer. First, the sample was ground under 100 μm , and then, 1.5 g of the sample was mixed with 7.5 g of $\text{LiBO}_4 + \text{LiB}_4\text{O}_7$ mix. Before the measurement, the mixture was transformed to glass pellet form by fusion method. The result of the chemical analysis of the sample is presented in Table 1. Additionally, the mineralogical analysis of the sample was done using a Rigaku ZSX Primus II model x-ray diffraction (XRD) with using $\text{CuK}\alpha$ radiation, and the XRD result of the sample is seen in Fig. 1. As seen from Fig. 1, the major mineral was the talc in the sample. This result indicated that the sample was pure enough for the experiments.

Table 1. Chemical Analysis (XRF) of raw talc sample

| Comp. | SiO ₂ | MgO | Fe ₂ O ₃ | Al ₂ O ₃ | CaO | Na ₂ O | CuO | K ₂ O | LOI |
|-------|------------------|------|--------------------------------|--------------------------------|------|-------------------|------|------------------|-----|
| (%) | 63.4 | 33.7 | 0.47 | 0.05 | 0.05 | 0.02 | 0.01 | 90 (ppm) | 2.3 |

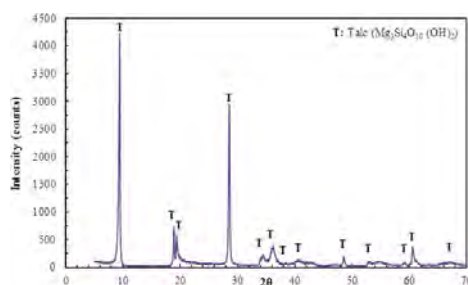


Figure 1. XRD graph of the raw talc sample

Grinding of talc

The laboratory type ceramic ball mill by using alumina balls were utilized for laboratory scale talc sample grinding. Before the grinding process, the particle size of raw talc sample was decreased to -1 mm by an impact crusher. In the grinding experiments; the ball size and distribution, ball feed(j), material feed(f_i), critical speed (%N_c), and time of grinding were optimized. The conditions for the mill, media, and material used in the grinding experiments are presented in Table 2.

Preparation of paint

The solid/liquid suspensions for water based paint were prepared in a 1.000 ml volume lab container, considering the complete components in paint recipe. The paints were prepared by using a laboratory type high speed (20.000 rpm max.) disperser/dissolver. In current research, white pigment containing paint ingredient was determined, including the following percentages of the formulation: Pigment = 53% (15% TiO₂ and 38% filler), re-

Table 2. Properties of mill, media, and material used in grinding experiments.

| | | |
|---------------------------|---|-----------------------------------|
| Mill (Ceramic) | Volume (cm ³) | 3.000 |
| | Dimensions | Diameter: 150 mm |
| | | Length: 200 mm |
| | Critical speed (%Nc) | 50, 60, 70, 75, 80, 85, 90 |
| Grinding time (min) | 30, 45, 60, 90, 120 | |
| Media (Alumina balls) | Ball sizes (mm) | 12, 16, 20 |
| | Ball density (g/cm ³) | 2,80 |
| | Ball feed (%) (j) | 0.25; 0.30; 0.35; 0.40; 0.45 |
| | Ball size distribution (12, 16, 20 mm) %wt. | 50-25-25 |
| Material (Talc sample) | Density (g/cm ³) | 2,9 |
| | Bulk density (g/cm ³) | 0.957 |
| | Material feed (%) (fc) | 0.120; 0.140; 0.160; 0.190; 0.210 |

sin = 18%, additives = 2.5% (defoamer, dispersant, bactericide, biocide, thickener, surfactant, and coalescent), and solvent = 26.5% water. Throughout the investigations, the ingredients ratios (pigments/mineral filler, resin, solvent, and additives) were kept constant. Only the type of talc sample used as a functional filler in the recipe was changed. Leneta type cardboards were used for OP and BR measurements. Gloss, viscosity, pH were also measured. The major properties of a coating which are related to the filler quality, are the OP and BR. Therefore, these properties were used in regression analysis. The OP has no unit, and is calculated from Equation (1) (Conceição et al., 2018):

$$OP(\%) = \frac{R_p}{R_b} \cdot 100 \quad (1)$$

Here:

R_p = reflectance under the black background.

R_b = reflectance under the white background.

Datcolor spectrophotometer was used to define the OP of the paint dry film. As a general application the paint was spread on white cardboard with a black strip, type Leneta, using a 100 μ m thick extender. Hiding power/opacity was calculated according to TS ISO 6504-3 standard.

The brightness/gloss values were defined by Sheen gloss meter on the dry film. This time the paint was spread on a glass surface, with a extender of 100 μ m thickness. Brightness/gloss was calculated according to TS ISO 6504-3 standard as well.

The chosen functional filler was different talc samples obtained under different grinding conditions.

Multivariate Linear Regression Analysis (MRA)

Whenever a mathematical model required to explain the relationship between two or more variables with a causal relationship, the regression analysis which is a statistical analysis technique is chosen.

The simple linear regression model includes a dependent and independent variable. Multiple linear regression model includes one dependent and multiple independent variables. In some cases, the number of dependent variables may be more than one, as may be the number of independent variables. In such cases, multivariate multiple regression analysis is used to examine linear relationships between dependent and independent variables. In MRA, the number of dependent variables is important, and must be more than one dependent variable. If dependent and independent variables are continuous variables, multivariate multiple linear regression is used to investigate the linear relationship between the dependent and independent variables (Dattalo, 2013).

In cases where the number of dependent variables is two or more, multivariate multiple linear regression analysis, which is the generalized version of multiple linear regression analysis is used. The calculation of the sum of squares and coefficient estimates required to determine the validity of the model are similar to those of multiple linear regression analysis (Ozdamar, 2004).

The multivariate multiple linear regression model is given by Equation (2):

$$Y = X\beta + \varepsilon \quad (2)$$

where Y; nxp dimensional dependent variable matrix, X; nx(q+1) dimensional independent variables matrix, β ; (q+1)xp the matrix of regression coefficients and In cases where the number of dependent variables is two or more, multivariate multiple linear regression ε shows nxp dimensional error matrix.

In order to perform multivariate multiple regression analysis, some assumptions must be realized. These; the expected value of the error matrix is zero, ie this assumption, expressed as $E(Y) = XB$, indicates that the model is linear. The second assumption is error matrix are unrelated. This assumption is related to the covariance matrix. The final assumption is that the error matrix has a multivariate normal distribution (Srivasta and Khatri, 1979).

The Akaike information criterion, AIC, was developed by Akaike (1974) to estimate between the model generating the data and a fitted model. AIC is widely used in model selection and a biased estimator.

Some features of AIC are listed as follows:

- In model comparisons, the model with the lowest AIC value is always preferred.
- AIC is valid not only within the selected sample size but also in the future forecast outside the selected sample size.
- It can be used easily in nested, non-nested and interlaced models.

RESULTS

Table 3 shows 15 experiments produced with control variables ball charge (*BC*), material charge (*MC*) and time of grinding (*TM*) as well as Opacity (*OP*), Brightness (*BR*) and average particle size (d_{50}).

Table 3. Independent and Dependent Variables (*OP*, *BR* and d_{50})

| Experiment | X1 (<i>BC</i>) | X2 (<i>MC</i>) | X3 (<i>TM</i>) | Y1 (<i>OP</i>) (%) | Y2 (<i>BR</i>) (85°) GU | Y3 (d_{50}) (μm) |
|------------|---------------------|---------------------|---------------------|-------------------------|---------------------------------|--------------------------------------|
| 1 | 0.45 | 0.14 | 30 | 88.73 | 1.4 | 12 |
| 2 | 0.4 | 0.14 | 30 | 88.47 | 1.5 | 12 |
| 3 | 0.35 | 0.14 | 30 | 89.28 | 1.3 | 14 |
| 4 | 0.3 | 0.14 | 30 | 88.26 | 1.3 | 15 |
| 5 | 0.25 | 0.14 | 30 | 88.34 | 1.3 | 16 |
| 6 | 0.25 | 0.21 | 30 | 83.58 | 1.3 | 15 |
| 7 | 0.25 | 0.19 | 30 | 84.71 | 1.4 | 15 |
| 8 | 0.25 | 0.16 | 30 | 84.30 | 1.3 | 17 |
| 9 | 0.25 | 0.14 | 30 | 85.02 | 1.5 | 19 |
| 10 | 0.25 | 0.12 | 30 | 85.79 | 1.5 | 20 |
| 11 | 0.25 | 0.19 | 120 | 83.19 | 1.6 | 9 |
| 12 | 0.25 | 0.19 | 90 | 81.84 | 1.5 | 11 |
| 13 | 0.25 | 0.19 | 60 | 81.73 | 1.6 | 12 |
| 14 | 0.25 | 0.19 | 45 | 81.96 | 1.4 | 14 |
| 15 | 0.25 | 0.19 | 30 | 83.04 | 1.6 | 17 |

In the next step, multivariate multiple linear regression analysis was applied and the results are presented in Table 4. As seen in Table 4, AIC was found to be 59.6315.

Table 4. Multivariate Multiple Regression Analysis Results

| | <i>OP</i> | <i>BR</i> | d_{50} |
|-----------|-------------------|------------------|--------------------|
| Constant | 82.7383 (4.4112)* | 1.2452 (0.1739) | 13.3053 (3.8902) |
| <i>BC</i> | -8,6927 (1.8074) | -0.0494 (0.0083) | 78.4495 (15.7321) |
| <i>MC</i> | 43.2573 (12.9523) | 0.4463 (0.1482) | -65.6294 (38.1924) |
| <i>TM</i> | 0.0077 (0.0181) | -0.0002 (0.0012) | -0.0432 (0.0373) |
| AIC | 59.6315 | | |

*: Valuesarum in parentheses indicate standard error values.

Equation (3), (4), and (5) show the models for *OP*, *BR*, and d_{50} .

$$OP = 82.7383 - 8.6927 * BC + 43.2573 * MC + 0.0077 * TM \quad (3)$$

$$BR = 1.2452 - 0.0494 * BC + 0.4463 * MC - 0.0002 * TM \quad (4)$$

$$d_{50} = 13.3053 - 78.4495 * BC - 65.6294 * MC - 0.0432 * TM \quad (5)$$

Then, d_{50} was excluded from the analysis because it was found not significant. In the next step, multivariate multiple linear regression analysis was applied and the results are seen in Table 5. As shown in Table 5, AIC was found to be 17.7874.

Table 5. Multivariate Multiple Regression Analysis Results without d_{50}

| | <i>OP</i> | <i>BR</i> |
|-----------|-------------------|------------------|
| Constant | 82.5213 (4.0754)* | 1.2455 (0.1545) |
| <i>BC</i> | -8.8227 (1.6502) | -0.0554 (0.0075) |
| <i>MC</i> | 43.1563 (10.7992) | 0.3484 (0.1164) |
| <i>TM</i> | 0.0078 (0.0012) | 0.0003 (0.00012) |
| AIC | 17.7874 | |

*: Valuesarum in parentheses indicate standard error values.

Equations, (6) and (7) show the models for *OP* and *BR*.

$$OP = 82.5213 - 8.8227 * BC + 43.1563 * MC + 0.0078 * TM \quad (6)$$

$$BR = 1.2455 - 0.0554 * BC + 0.3484 * MC - 0.0003 * TM \quad (7)$$

When the two models are compared (with d_{50} and without d_{50}), the model with the smaller AIC value is selected. Accordingly, the model (without d_{50}) expressed by Eqs. (6) and (7) is better. It was observed that removing the d_{50} variable gives better results because, AIC value is lowest.

One of the assumptions of MRA, whether the error matrix comes from the multivariate normal distribution should be tested. Multivariate Normality tests are using t value and its p value. Accordingly, for Equations (6) and (7), it was tested whether the error matrix came from the multivariate normal distribution. The analysis results are given in Table 6. According to Table 6, it is seen that the error matrix

Table 6. Multivariate Normality Test

| n | Variables | Salope | t | P |
|----|-----------|--------|-------|-------|
| 15 | 2 | 0.893 | 2.226 | 0.022 |

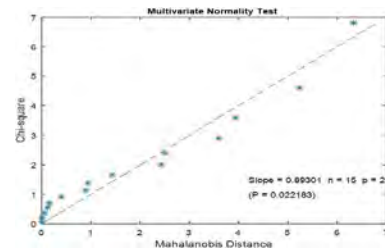


Figure 2. Results for Multivariate Normality Test

has a multivariate normal distribution at 1% significance level ($p > 0,01$). The result of the multivariate normality test is shown in Fig. 2. Equations (6) and (7) can be used for interpretation.

Within this research, MRA is found convenient to explain the changes on the water-based paint dry film properties developed by the varying talc product characteristics in the recipe due to different grinding parameters.

DISCUSSION

In this study, multivariate multiple regression analysis was used for modeling. A model was created through the combined use design of mixtures.

Using the equations of a linear model showed that it was possible to foresee the value of the OP and BR for any change of the grinding parameter used.

While the other variables were constant, when the value of BC was increased by one unit, the value of OP decreased by 8.8227 units. When the value of MC was increased by one unit, the value of OP increased by 43.1563 units. Similarly, when the value of BC was increased by one unit, the value of BR results in a decrease of 0.0554 units. One unit increase in MC leads to an increase in the value of BR by 0.3484 units.

It can easily be seen from the results obtained from this study that there is a direct relationship between ball charge (BC) and the average particle size (d_{50}) of talc samples used in paint. With the increase in BC for the grinding, more effective grinding conditions were supplied and produced smaller particle sizes (d_{50}) talc samples. However, smaller particle size does not indicate better OP properties in the paint. Oppositely, in our studies, the hiding power/opacity decreased with the decrease of the average particle size (d_{50}) due to increased BC in the grinding. On the other hand, with the increase of material charge (MC) in the grinding caused a slight decrease at average particle sizes (d_{50}) of talc samples. Despite, a slight decrease at d_{50} sizes, a significant increase calculated with the OP of the paint. This can be explained as; when we increase the amount of ball in mill cataract and cascade forces be more effective and get better grinding conditions to result with smaller size but also rounded (with less aspect ratio) particles.

When the amount of material(talc) was increased in the mill, then the effect of cataract and cascade forces were decreased, and results with bigger sized (compared to high BC grindings) but less rounded (with higher aspect ratio) particles. Talc particles would probably have larger platy surfaces due to higher d_{50} size, less rounded shape and higher aspect ratio, and will improve the hiding power/opacity

of the paint. With the increase of material charge (MC) in grinding caused a significant increase at OP of the paint.

It can be said from the XRD analysis of raw and ground

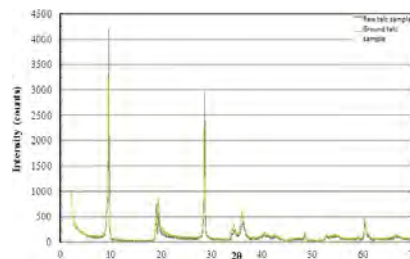


Figure 3. Mineralogical Analysis (XRD) of raw and ground talc samples.

und talc samples given in Fig. 3. that there was no significant change in the crystal/cage structure of talc after grinding. Addition to this, the corners of the structure were rounded after the grinding.

It can clearly be seen from the particle size (2) dimension calculations on SEM photos by using the auto-cad program before and after the grinding that the aver. the aspect ratio was significantly changed/decreased due to grinding as shown in Table 7.

Table 7. Measured dimensions and aspect ratios of talc samples

| Particle no | Raw Talc Samples | | | | Ball Mill Talc Samples | | | |
|--------------|------------------|-------------|-------------|--------------|------------------------|-------------|-------------|--------------|
| | L.E. | S.E. | A.R. | C.R. | L.E. | S.E. | A.R. | L.E. |
| 1 | 15.56 | 8.19 | 1.90 | 0.720 | 11.1 | 9.17 | 1.21 | 0.710 |
| 2 | 11.03 | 6.80 | 1.62 | 0.660 | 22.00 | 12.18 | 1.81 | 0.794 |
| 3 | 29.76 | 19.39 | 1.53 | 0.619 | 7.81 | 4.91 | 1.59 | 0.614 |
| 4 | 12.25 | 5.38 | 2.28 | 0.683 | 14.33 | 9.73 | 1.47 | 0.796 |
| 5 | 30.53 | 11.03 | 2.77 | 0.566 | 12.17 | 9.76 | 1.25 | 0.571 |
| 6 | 10.42 | 7.00 | 1.49 | 0.542 | 11.10 | 9.17 | 1.21 | 0.802 |
| 7 | 12.37 | 6.21 | 1.99 | 0.639 | 9.94 | 5.11 | 1.95 | 0.534 |
| 8 | 10.22 | 5.52 | 1.85 | 0.694 | 10.00 | 4.84 | 2.07 | 0.698 |
| 9 | 16.64 | 15.89 | 1.05 | 0.583 | 10.30 | 5.88 | 1.75 | 0.703 |
| 10 | 12.76 | 5.09 | 2.51 | 0.608 | 10.92 | 9.93 | 1.10 | 0.527 |
| 11 | 24.11 | 11.55 | 2.09 | 0.626 | 14.33 | 9.73 | 1.47 | 0.576 |
| 12 | 13.09 | 5.58 | 2.35 | 0.725 | 7.81 | 4.91 | 1.59 | 0.590 |
| 13 | 10.07 | 5.52 | 1.82 | 0.735 | 8.65 | 5.23 | 1.65 | 0.644 |
| 14 | 8.89 | 5.79 | 1.54 | 0.671 | 7.92 | 4.84 | 1.64 | 0.836 |
| 15 | 14.99 | 9.82 | 1.53 | 0.659 | 14.85 | 6.99 | 2.12 | 0.713 |
| 16 | 13.04 | 7.02 | 1.86 | 0.652 | 7.67 | 5.03 | 1.52 | 0.514 |
| 17 | 9.06 | 8.33 | 1.09 | 0.541 | 12.51 | 6.34 | 1.97 | 0.701 |
| Aver. | 14.98 | 8.47 | 1.77 | 0.642 | 11.37 | 7.28 | 1.56 | 0.666 |

L.E. : Long edge
S.E. : Short edge
A.R. : Aspect ratio
C.R. : Circularity

The circularity of talc particles was also calculated on the 2D image given in Fig. 4. After the calculation, it was seen in Table 7 that the particles become more circular/ro-



Figure 4. 2D image of ground talc particles.

unded after grinding.

The increase of *BC* and *MC* had a very minor effect on *BR* of paint, therefore, can be ignored.

CONCLUSION

In this study talc mineral was ground at different grinding conditions and utilized as the variable mineral filler of a water-based paint recipe. Multivariate multiple regression analysis was applied to foresee the influence of grinding parameters of talc to the properties of the paint.

The results showed that it was possible to foresee the changes on *OP* and *BR* of a dry film depends on the mineral filler characteristics in the same paint. In other words, it was possible to foresee the changes on *OP* and *BR* of the paint due to changing grinding parameters of talc used as mineral filler in paint by using MRA. Besides that, applying this regression analysis, the main effects of each parameter of the grinding can be determined to paint basic properties.

ACKNOWLEDGEMENT

The authors would like to thank the Research Fund Unit of Afyon Kocatepe University for financial support (AKU 17.FEN.BİL.63).

REFERENCES

1. Akaike, H, 1974, A new look at the statistical model identification, *IEEE Transaction on Automatic Control* 19, 716–723.
2. Bezerra, M.A., Santelli, R.E., Oliveira, E.P., Villar, L.S., Escalera, L.A., 2008, Response surface methodology (RSM) as a tool for optimization in analytical chemistry, *Talanta* 76, 965–977.
3. Box, G. E., Hunter, J. S., 1961, The 2k-p fractional factorial designs. *Technometrics*, 3, 311– 351.
4. Ciullo P.A., 1996, *Industrial Minerals and Their Uses, A Handbook & Formulary*, Noyes Publication, Westwood New Jersey, 125-136.
5. Conceição, Petter & Sampaio, 2018, Prediction of water-based paint properties based on their mineral fillers; Simplex-PLSR coupling application, 3-5.
6. Dattalo, P, 2013, *Analysis of Multiple Dependent Variables*. Oxford University, Oxford.
7. DPT, (2001), *Particular Industrial Minerals, Sub-commission Soil-based Industrial Raw Materials I*. Special Commission Report, Ankara.
8. Grim, R., 1968, *Clay mineralogy*, McGraw-Hill Book Company, New York, 596.
9. Gündüz, G., 2005, *Paint information*. TMMOB Chamber of Chemical Engineers, p.461.
10. Karakaş, F., 2011, *Functioning Mechanism of Industrial Minerals in Water-based Paints*, Ph.D. Thesis Istanbul Technical University, Institute of Science, Mining Engineering Dept., p.185, Istanbul Turkey.
11. Menezes, R. R., Malzac Neto H. G., Santana, L. N. L., Lira, H. L., Ferreira, H. S. and Neves, G. A., 2008, Optimization of wastes content in ceramic tiles using statistical design of mixture experiments, *Journal of the European Ceramic Society*, 28, 3027–3039.
12. Özdamar, K, 2004, *Statistical Data Analysis with Package Programs*, Kaan Publishes, Eskisehir Turkey.
13. Paksoy S., 1999, *Paint Handbook*, TMMOB Chamber of Chemical Engineers, Istanbul.
14. Srivastava, M., Khatri, C, 1979, *An Introduction to Multivariate Statistics*. North Holland, New York, USA.
15. Wold, H., 1973, "Nonlinear Iterative Partial Least Squares (NIPALS) modelling: Some current developments." In *Multivariate Analysis III*. Proceedings of the 3rd International Symposium on Multivariate Analysis. Dayton, Ohio, edited by P. R. Krishnaiah, 383-407. Academic Press.
16. Wold, S., Sjöström, M., Eriksson, L., 2001, *Chemometrics and Intelligent Laboratory Systems* 58, 109–130.
17. Yekeler, M., Ulusoy, U., Hiçyılmaz, C., 2004, Effect of particle shape and roughness of talc mineral ground by different mills on the wettability and floatability, *Powder Technology*, 140, 68-78.
18. Yürekli, Ş., 1997, *Resine and Paint Technology*, Istanbul.

Thermodynamic Analysis of Effects of the Inlet Air Cooling on Cycle Performance in Combined Brayton-Diesel Cycle

Betul Sarac¹  Teoman Ayhan² 

¹Karadeniz Technical University, Department of Naval Architecture and Marine Engineering, Trabzon, Turkey

²Avrasya University, Department of Mechanical Engineering, Trabzon, Turkey

ABSTRACT

In the present study, the effects of inlet air cooling on compound cycle performance in a diesel gas turbine engine system where waste heat is used in the composite power system in the sustainable energy system were investigated thermodynamically. The effects of the inlet air cooling the system that enhances power production and the resulting thermal efficiency values were analyzed based on various operational variables (gas turbine pressure ratio, diesel engine compression ratio, gas turbine inlet and fresh air inlet temperatures, etc.). The energy losses in each system component were determined and the second law efficiency of the system was determined based on the introduced operational parameters. The gas turbine unit in the model included a gas generator with two compressors and a high-pressure turbine, and a low-pressure power turbine running on a separate shaft. The diesel engine and gas-generator exhaust gases were mixed and expanded in a low-pressure turbine, leading to the production of power with the waste energy. In the cycle, an intake air cooler, an intercooler and a recuperative air pre-heater were used. In the intake air cooling cycle, the power increase was around 15% when the pressure rate of the low-pressure compressor was 3.5. Natural gas was used as fuel in the thermodynamic model. The cycle irreversibility was used in the calculations based on the thermodynamic concepts.

Keywords:

Brayton-diesel cycle, Combined power system, Energy, Exergy

INTRODUCTION

The contribution of energy in ensuring the sustainability of modern life is a primary requirement. Today, energy technologies are advancing towards the use of clean energy resources. However, it is observed that it would take long years to develop the technologies that could be adequate for global energy requirements [1]. Today, energy conversion technologies based on fossil fuels are used in power generation and to fulfill power requirements. Due to the development of energy conversion technologies based on fossil fuels, the importance of composite cycles in the reduction of exhaust emissions released to the environment per unit of generated electrical energy and the thermal efficiency of the system has increased. The combined power cycles for high efficiency and reduction of negative effects on the environment have led to the consideration of combined power cycles as ideal conventional power systems [2,3].

The combined power systems are also commonly applied in power propulsion systems of high tonnage ships [4,5,6]. The fact that natural gas could be used as fuel in combined power systems led to the development of other thermodynamic power cycles that work with diesel-based combined power cycle systems [7]. In gas turbine plants constructed in warm climates or combined power systems with a gas turbine, cooling of the compressor inlet air induces a need for additional power on top of the installed power [8,9,10,11]. In thermodynamic performance calculations for current combined power cycles, the calculations conducted with standard air assumptions are preferred for practical engineering purposes [12,13].

The literature revealed that there was no previous study on a combined power system with a supercharged diesel cycle connected with a gas generator that works

Article History:

Received: 2020/01/14

Accepted: 2020/01/30

Online: 2020/03/26

Correspondence to: Betül Sarac,
Department of Naval Architecture and
Marine Engineering, Karadeniz Technical
University, 61530, Trabzon, Turkey.
E-mail: bsarac@ktu.edu.tr,
Phone: +535 397 27 03,
Fax: +462 752 21 58.

with a split shaft and the cooling of compressor inlet air and a low-pressure gas turbine [14]. There are several studies on diesel engine performance and theoretical diesel cycle models in the literature [15,16, 17]. In the present study, a combined power cycle design was attempted based on the assumption that the selected diesel engine was adiabatic. The present study aim to calculate the thermodynamic availability and performance of the above-mentioned combined power system and to investigate the effects of atmospheric air cooling in the compressor inlet on the combined power system. [18] investigated the variations in the second law efficiency of gas turbines and their effects on the thermal efficiency of the combined cycle based on different gas turbine parameters. They reported that the exergy efficiency for different gas turbine operating parameters varied between 33.8% and 28.7% and the combined cycle thermal efficiency varied between 42% and 55% due to change in various parameters [18].

Energy, exergy and exergy economy in combined diesel engine power systems study was made by [19]. They introduced the formulas required to calculate energy exergy and exergy economy in each combined power system unit. They reported that the combined power systems that operate with compression ignition engines were among the most efficient simple cycle power generation plants and their efficiency was around 50%.

Different methods to improve efficiency gas turbine cogeneration cycle are studied by [20]. In these methods, they investigated the increase in gas turbine inlet air temperature, cooling the compressor inlet air, air preheating, fuel preheating, increasing the compressor inlet air pressure, increasing the excess air rate, steam injection, and humidification of the compressor inlet air. They reported that exergy efficiency increased by 20% with efficiency improvement methods and they emphasized that, if possible, efficiency improvement methods should be applied together in combined power systems.

In the present study, a combined power cycle designed with a pre-cooler, an intercooler, and a recuperator, and included a gas generator, a power turbine, and a diesel engine, was introduced. The current study aim to calculate the thermodynamic availability and performance of the introduced combined power cycle and to investigate the effects of intake air cooling at the compressor inlet on the combined power system.

It is found that the improvements in the first and second law efficiencies of the proposed models were significant and the recuperator application criterion was dependent on the rpk. The amount of fuel consumed in the gas turbine combustion chamber is reduced 10% with a comparison to the without pre-cooled combined cycle.

MATERIAL AND METHODS

System Description

The installation diagram of the system that included a diesel engine connected to a split shaft gas generator and a low-pressure turbine that utilized the waste energy of the exhaust gas and the compressor inlet air cooling unit is presented in Figure 1. The air drawn by the low-pressure compressor from the atmosphere is transferred through a pre-cooler, and the pressure is increased in the compressor and then passed through an intercooler and the air temperature was reduced to the atmospheric temperature and then a certain amount was sent to the high-pressure compressor and the remaining was sent to the diesel engine. The air, the pressure and temperature of which was increased in the high-pressure compressor was combined with the fuel in the the combustion chamber and the combustion of the fuel increases the air temperature up to the high-pressure turbine inlet temperature.

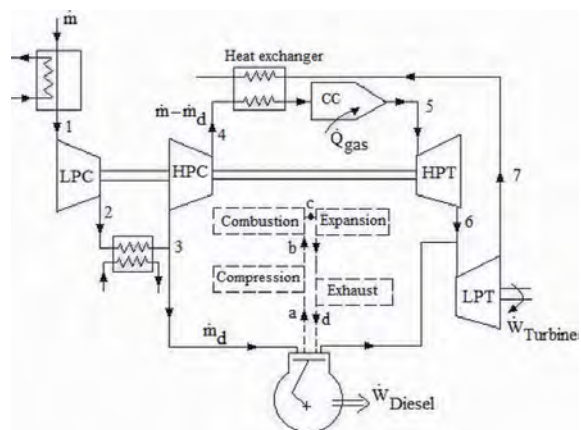


Figure 1. Brayton-diesel combined power system where the inlet air is cooled.

The combination of the air and the fuel in the diesel engine leads to an expansion due to the heat generated by combustion and produces power, and is mixed with the exhaust gases from the high-pressure turbine at the low-pressure turbine inlet and enters into the split-shaft low-pressure turbine and released to the atmosphere after expanding and producing power. The airflow completed by the low-pressure turbine is described as an open gas turbine cycle of the system in the literature [13]. In the present study, the thermodynamic model of the introduced system was developed based on thermodynamic air standard assumptions. It was assumed that the modeled diesel engine was adiabatic, and the cycle was an ideal diesel cycle. It was accepted that irreversibility in the gas turbine and the gas generator originated from compressors, turbines, combustion chamber, the mixture of air currents, pre-cooled and inter-cooled heat exchangers and recuperators. In gas turbine power units, it was reported in the literature that cooling the compressor

intake air, especially in hot climate conditions, improved power generation. In the introduced system, quantitative and qualitative thermodynamic calculations were conducted to determine the effects of cooling the compressor intake air on system performance. Different techniques have been used in compressor intake air cooling. In the present study, it was considered to use an indirect evaporative air cooler. The aim of this study did not include investigating the effects of indirect evaporation air cooler performance on the introduced system. In the introduced system, the compressor and turbine connected to the diesel engine were not connected to the same shaft. Thus, the pressure of the supercharged air required by the diesel engine could be supplied directly from the low-pressure compressor. In the combined power system, the operating pressure of the diesel engine under supercharged conditions that corresponded to the values where the engine operated based on the turbocharged values was considered.

Thermodynamic Model

The ideal and irreversible processes of the combined cycle based on the station numbers indicated in the combined system installation scheme are presented in Fig. 1 and the introduced combine system cycle is presented in P-V and h-s diagrams in Fig. 2. The common cycle for the low-pressure turbine associated with the gas generator was a typical Joule-Brayton cycle. In the proposed model of the combined power system with and without air cooling at the compressor inlet, the volumetric flow of air that passes through the system remains constant. The effects of air cooling in the compressor inlet on the combined system performance were also discussed. The cycles formed by the stations that defined the processes in the combined cycle under ideal operating conditions are (a-b-c-d) and (1-2s-3-4s-5-d-6s-6m-7s).

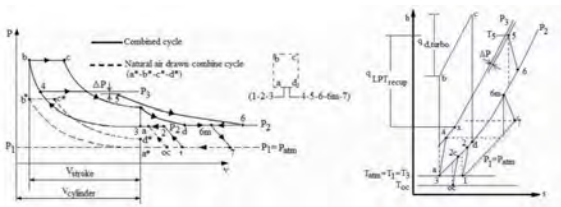


Figure 2. Combined power system P-v and h-s diagrams

The cycle formed by the processes defined by irreversibility is (1-2-3-4-5-d-6-6m-7). The compressor inlet air cooling cycle varies (oc-2c-3-4-5-d-6-6m-7).

The properties of the diesel engine used in the system were obtained from the values of the diesel engine used as the main propulsion engine in the RO-RO cargo ship named M/V ASSTAR TRABZON. The diesel engine was a 12-cylinder, four-stroke, V type engine with a nominal power of 2935 kW and a cylinder diameter 320 mm and a stro-

ke length of 420 mm [21]. In the present study, the volumetric compression ratio was selected as 8, the fuel cut-off ratio was selected as 2 and the rotation speed was selected as 600 rpm. The temperature and pressure values at the diesel cycle process stations and the cycle equations are given based on the compression and fuel cut-off rates are presented below:

Volumetric compression rate and fuel cut-off ratio

$$r_v = \frac{v_a}{v_b}, r_c = \frac{v_c}{v_b} \quad (1)$$

Temperature and pressure for isentropic compression are defined as below

$$T_b = r_v^{k-1} T_a, P_b = r_v^k P_a \quad (2)$$

Temperature and pressure at the end of the constant pressure heating

$$T_c = r_c r_v^{k-1} T_a, P_c = P_b \quad (3)$$

Temperature and pressure at the end of the isentropic expansion process

$$T_d = r_c^k T_a, P_d = r_c^k P_a \quad (4)$$

Mean effective pressure P_{mean}

$$P_{mean} = \frac{P_a r_v^k \left[k(r_c - 1) - r_v^{1-k} (r_c^k - 1) \right]}{(k-1)(r_c - 1)} \quad (5)$$

The thermal efficiency of the diesel cycle was calculated with Eq. (6) [13].

$$\eta_d = 1 - \left(\frac{1}{k} \right) \left(\frac{1}{r_v^{1-k}} \right) \left(\frac{r_c^k - 1}{r_c - 1} \right) \quad (6)$$

Effective power equations for low and high-pressure compressors are given

$$\dot{W}_{LPC} = \frac{m c_p^{1-2} (T_{2s} - T_1)}{\eta_{LPC}}, \dot{W}_{HPC} = \frac{(m - m_{d,turbo}) c_p^{3-4} (T_{4s} - T_3)}{\eta_{HPC}} \quad (7)$$

Effective power equations for low and high-pressure turbines are given below:

$$\dot{W}_{HPT} = \left(m - m_{d,turbo} \right) c_p^{5-6} (T_5 - T_{6s}) \eta_{HPT} \quad (8)$$

$$\dot{W}_{LPT} = m c_p^{6m-7} (T_{6m} - T_7) \eta_{LPT}$$

The pressure loss in the combustion chamber is described with ΔP and the inlet pressure for the high-pressure turbine is defined in Eq. (9).

$$P_{T5} = P_3 (1 - \varepsilon_y) \quad (9)$$

ε_y depicts the pressure loss percentage in Eq. (9) and varies between %4 and 6. The exhaust gas pressure for the

pressure loss in low-pressure turbine exhaust is defined below and ψ_{exp} depicts the exhaust gas expansion loss coefficient and varies between 1.2 and 1.4.

$$P_{exhaust} = \psi_{exp} P_{atm} \quad (10)$$

The calculations were conducted with the assumption that air exhaust pressure in the low-pressure turbine was $P_6 = P_{exhaust}$. The mass flow of the air that passes through the low pressure compressor under atmospheric conditions was accepted as m and the atmospheric conditions were accepted as ideal and the z is calculated with Eq. (11), the dimensionless energy equation for the gas generator. The defined z is a significant parameter that determines the high efficiency operating range of the designed cycle.

$$(z-1)\theta \bar{c}_p \left(1 - \frac{1}{\phi_{HPT}}\right) \eta_{HPT} = \frac{(z-1)(\phi_{HPT}-1)}{\eta_{HPK}} + z \frac{(\phi_{HPT}-1)}{\eta_{LPLK}} \quad (11)$$

The dimensionless magnitudes in the equation above can be written as follows:

High-pressure turbine exponential pressure ratio ϕ_{HPT} ;

$$\phi_{HPT} = \frac{T_5}{T_6} = \left(\frac{P_{T5}}{P_6}\right)^{\frac{k-1}{k}} \quad (12)$$

Low-pressure compressor pressure ratio r_{pk1} and high-pressure compressor pressure ratio r_{pk2} ,

$$r_{pk1} = \frac{P_2}{P_1}, \quad r_{pk2} = \frac{P_3}{P_2} \quad (13)$$

Compressor unit pressure ratio:

$$r_{pk} = \frac{P_3}{P_1}, \quad \phi_{LPC} = \frac{T_{2s}}{T_1} = \left(r_{pk1}\right)^{\frac{k-1}{k}}, \quad (14)$$

$$\phi_{HPC} = \frac{T_{4s}}{T_3} = \left(r_{pk2}\right)^{\frac{k-1}{k}}, \quad \phi_K = \phi_{LPC} \phi_{HPC}$$

The ratio of the highest cycle temperature to atmospheric air temperature:

$$\phi_K = \frac{T_5}{T_1} \quad (15)$$

The ratio of specific temperatures at dimensionless constant pressure:

$$\bar{c}_p = \frac{c_{p,Turbine}}{c_{p,Compressor}} \quad (16)$$

Theoretical volumetric air flow rate $\dot{V}_{cylinder}$ and theoretical mass flow rate $\dot{m}_{d,turbo}$ in the diesel cycle:

$$\dot{V}_{cylinder} = V_{cylinder} \left(\frac{n}{2}\right) \left(\frac{1}{60}\right), \quad \dot{m}_{d,turbo} = \frac{P_2 \dot{V}_{cylinder}}{RT_3} \quad (17)$$

The ratio of theoretical mass airflow in the system \dot{m} , to the supercharged air mass flow in the diesel cycle, $\dot{m}_{d,turbo}$ is defined as z . z and theoretical air mass flow \dot{V}_{system} in the system are given below,

$$z = \frac{\dot{m}}{\dot{m}_{d,turbo}}, \quad \dot{V}_{system} = \frac{\dot{m} RT_{atm}}{P_{atm}} \quad (18)$$

The intake air temperature in the compressor inlet air cooling is calculated with $T_{oc} = xT_{atm}$ this equation. Where x is the ratio of the intake air cooling temperature to the atmospheric air temperature and could vary between 0.85 and 0.99 and could be applied technologically. Volumetric flow air inlet temperature in the system remains constant with or without cooling; thus, the mass flow of the air in the pre-cooled cycle can be calculated with the following equation:

$$\dot{m}_{oc} = \frac{P_{atm} \dot{V}_{system}}{RT_{oc}} \quad (19)$$

The following equation could be written for the mass air flows in pre-cooled and without pre-cooled cycles:

$$\dot{m}_{oc} = \frac{1}{x} \dot{m} \quad (20)$$

The changes in average specific temperatures of the air in isentropic compression and expansion in pre-cooled and without pre-cooled cycles are negligible. The thermal efficiency of the cycle can be written as follows:

$$\eta = \frac{\dot{W}_{d,turbo} + \dot{W}_{LPT}}{\dot{Q}_{d,turbo} + \dot{Q}_{gas}} \quad (21)$$

where,

$$\dot{Q}_{d,turbo} = \dot{m}_{d,turbo} c_p^{b-c} (T_c - T_b), \quad (22)$$

$$\dot{W}_{d,turbo} = \eta \dot{Q}_{d,turbo} \quad \text{and} \quad \dot{Q}_{gas} = \dot{m} c_p^{5-4} (T_5 - T_4)$$

The thermal efficiency of the cycle with compressor intake air cooling was calculated with the equation below;

$$\eta_{oc} = \left[\frac{\dot{W}_{d,turbo} + \dot{W}_{LPT}}{\dot{Q}_{d,turbo} + \dot{Q}_{gas}} \right]_{oc} \quad (23)$$

The equations used in the air pre-cooling operation are similar to the equations used with the cycles without air pre-cooling and the cooling effects of the atmospheric air were included in these equations.

$$\eta_{I_{recup}} = \frac{\dot{W}_{d,turbo} + \dot{W}_{LPT}}{\left(\dot{m} - \dot{m}_{d,turbo}\right) c_{p5} T_5 - \left(\dot{m} - \dot{m}_{d,turbo}\right) c_{pTx} T_x + \dot{Q}_{d,turbo}} \quad (24)$$

$$\eta_{I_{recup,oc}} = \frac{\dot{W}_{d,turbo} + \dot{W}_{LPT,oc}}{\left(\dot{m}_{oc} - \dot{m}_{d,turbo} + \dot{m}_{y,gas,oc}\right) c_{p5} T_5 - \left(\dot{m}_{oc} - \dot{m}_{d,turbo}\right) c_{pTx} T_x + \dot{Q}_{d,turbo}} \quad (25)$$

The mass fuel flow in the diesel engine and the gas turbine was determined with the following equations. LHV depicts the thermal value of the fuel.

$$\dot{m}_{y,d,turbo} = \frac{\dot{Q}_{d,turbo}}{LHV - c_{pb-c} T_c}, \quad \dot{m}_{y,gas} = \frac{\dot{Q}_{d,turbo}}{LHV - c_{p4-5} T_5} \quad (26)$$

Total fuel consumption in the combined system was calculated with the equation below:

$$\dot{m}_y = \dot{m}_{d,turbo} + \dot{m}_{y,gas} \quad (27)$$

Where ψ depicts the ratio of the mass flow rate of the fuel utilized in the turbine combustion chamber to total fuel consumption mass flow rate and calculated with the following equation:

$$\psi = \frac{\dot{m}_{y,gas}}{\dot{m}_y} \quad (28)$$

The fuel consumption remains the same in fuel calculation for the cycle with pre-cooling. The following equation was used to determine the ratio of the system air mass flow rate to the total system fuel consumption:

$$\mu = \frac{\dot{m}}{\dot{m}_y}, \quad \beta = \frac{\dot{m}_y}{\dot{m}} \quad (29)$$

Since the mass airflow rate remains the same in the diesel cycle in the combined cycle, the fuel mass flow rate in the diesel cycle would also remain constant. In the diesel cycle, the air compression pressure may be high; however, the baseline compression temperature is reduced to the atmospheric pressure through the intercooler. In the theoretical cycle, the highest cycle temperature depends on the volumetric compression ratio of the cycle and the fuel cut-off rate and is directly proportional to the inlet temperature.

$$\dot{m}_{y,d,turbo} = \frac{\dot{Q}_{y,d,turbo}}{LHV - c_{pb-c} T_c}, \quad \dot{m}_{y,gas,oc} = \frac{\dot{Q}_{gas,oc}}{LHV - c_{p4-5} T_5} \quad (30)$$

$$\dot{m}_{y,oc} = \dot{m}_{y,d,turbo,oc} + \dot{m}_{y,gas,oc}, \quad (31)$$

$$\dot{m}_{y,saving} = \left(\dot{m}_{y,d,turbo} - \dot{m}_{y,recup} \right) 100 / \dot{m}_{y,d,turbo}$$

Exergy Analysis

The second law analysis in thermodynamics is a powerful tool in the optimization of complex power systems. Exergy, also known as usability, is the portion of energy that could be utilized. In the present study, the exergy of air at each system unit inlet was calculated with the following equation [13]:

$$e = c_p (T_1 - T_o) - T_o \left[c_p \ln \left(\frac{T_1}{T_o} \right) - R \ln \left(\frac{P_1}{P_o} \right) \right] \quad (32)$$

In the Brayton-diesel combined power system, where the intake air is cooled and shown in Fig. 1, the mass, energy, and exergy balance equations for each system component are presented in Table 1. In exergy calculations, the temperature was accepted as 25°C and the pressure was accepted as 1 atm for the dead state condition.

Since the temperatures remain constant in decomposition, pressure losses lead to irreversibility. The second law of thermodynamics efficiency equations for the pre-cooled and without pre-cooled systems is given in Eq. (33) and Eq. (34). The second law of thermodynamics efficiency for the recuperator system is given in Eq. (35).

$$\eta_{II} = \frac{\dot{W}_{y,d,turbo} + \dot{W}_{LPT}}{\dot{E}_{Q_{d,turbo}} + \dot{m} e_1 + \dot{E}_{Q_{Cb}} + \left(\dot{m} - \dot{m}_{d,turbo} + \dot{m}_{y,gas} \right) e_5 + \left(\dot{m}_{d,turbo} + \dot{m}_{y,diesel,oc} \right) e_3} \quad (33)$$

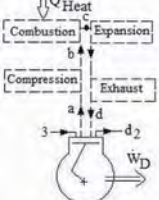
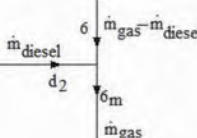
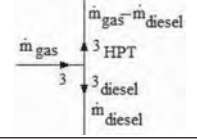
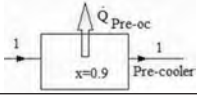
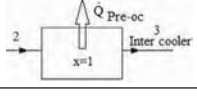
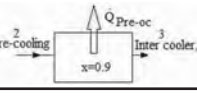
$$\eta_{II,oc} = \frac{\dot{W}_{y,d,turbo} + \dot{W}_{LPT}}{\dot{E}_{Q_{d,turbo}} + \dot{m}_{oc} e_1 + \dot{E}_{Q_{Cb}} + \left(\dot{m}_{oc} - \dot{m}_{d,turbo} + \dot{m}_{y,gas,oc} \right) e_5 + \left(\dot{m}_{d,turbo} + \dot{m}_{y,diesel,oc} \right) e_3} \quad (34)$$

$$\eta_{II,recup} = \frac{\dot{W}_{y,d,turbo} + \dot{W}_{LPT}}{\dot{E}_{Q_{d,turbo}} + \dot{E}_{Q_{Cb}} + \left(\dot{m} - \dot{m}_{d,turbo} + \dot{m}_{y,gas} \right) e_5} \quad (35)$$

The second law efficiency of the cycle with pre-cooling and recuperator is given below:

$$\eta_{II,recup} = \frac{\dot{W}_{y,d,turbo} + \dot{W}_{LPT,oc}}{\dot{E}_{Q_{d,turbo}} + \dot{E}_{Q_{Cb}} + \left(\dot{m} - \dot{m}_{d,turbo} + \dot{m}_{y,gas} \right) e_5 + \dot{E}_{Q_{pre-cooling}}} \quad (36)$$

Table 1. Mass, energy and exergy equations for system components

| | |
|---|--|
| <p>Low-pressure Compressor</p>  | $m_1 = m_2 \quad (37)$ |
| | $m_1 h_1 + W_{LPC} = m_2 h_2 \quad (38)$ |
| | $m_1 e_1 + e_{W_{LPC}} = m_2 e_2 + E_{d_{LPC}} \quad (39)$ |
| <p>High-pressure Compressor</p>  | $m_3 = m_4 \quad (40)$ |
| | $m_3 h_3 + W_{HPC} = m_4 h_4 \quad (41)$ |
| | $m_3 e_3 + e_{W_{HPC}} = m_4 e_4 + E_{d_{HPC}} \quad (42)$ |
| <p>High-pressure Turbine</p>  | $m_5 = m_6 \quad (43)$ |
| | $m_5 h_5 = m_6 h_6 + W_{HPT} \quad (44)$ |
| | $m_5 e_5 = m_6 e_6 + e_{W_{HPT}} + E_{d_{HPT}} \quad (45)$ |
| <p>Low-pressure Turbine</p>  | $m_6 = m_7 \quad (46)$ |
| | $m_6 h_6 = m_7 h_7 + W_{LPT} \quad (47)$ |
| | $m_6 e_6 = m_7 e_7 + e_{W_{LPT}} + E_{d_{LPT}} \quad (48)$ |
| <p>Combustion chamber</p>  | $m_4 = m_5 \quad (49)$ |
| | $m_4 h_4 + Q_{cb} = m_5 h_5 \quad (50)$ |
| | $m_4 e_4 + e_{Q_{cb}} = m_5 e_5 + E_{d_{Q_{cb}}} \quad (51)$ |
| <p>Diesel engine</p>  | $m_3 = m_6 \quad (52)$ |
| | $m_3 h_3 + Q_{Heat} = m_6 h_6 + W_D \quad (53)$ |
| | $m_3 e_3 + e_{Q_{Heat}} = m_6 e_6 + e_{W_D} + E_{d_{W_D}} \quad (54)$ |
| <p>Combined</p>  | $m_D + m_{gas} - m_D = m_{gas} \quad (55)$ |
| | $m_D h_D + (m_{gas} - m_D) h_{gas} = m_{gas} h_{6m} \quad (56)$ |
| | $m_D e_D + (m_{gas} - m_D) e_{gas} = m_{gas} e_{6m} + E_{d_{combine}} \quad (57)$ |
| <p>Separation</p>  | $m_{gas} = m_D + m_{gas} - m_D \quad (58)$ |
| | $m_{gas} h_{gas} = (m_{gas} - m_D) h_{HPT} + m_D h_D \quad (59)$ |
| | $m_{gas} e_{atm} = (m_{gas} - m_D) e_{atm} + m_D e_{atm} \quad (60)$ |
| <p>Indirect evaporative cooler for the intake air cooling</p>  | $m_1 = m_{1-oc} \quad (61)$ |
| | $m_1 h_1 = m_{1-oc} h_{1-oc} + Q_{pre-oc} \quad (62)$ |
| | $m_1 e_1 = m_{1-oc} e_{1-oc} + e_{Q_{pre-oc}} + E_{d_{pre-oc}} \quad (63)$ |
| <p>Inter cooler</p>  | $m_2 = m_{3,int-oc} \quad (64)$ |
| | $m_2 h_2 = m_{3,int-oc} h_{3,int-oc} + Q_{3,int-oc} \quad (65)$ |
| | $m_2 e_2 = m_{3,int-oc} e_{3,int-oc} + e_{Q_{3,int-oc}} + E_{d_{int-air-oc}} \quad (66)$ |
| <p>Intake air cooling operated for the inter cooler</p>  | $m_{2oc} = m_{3oc,int-oc} \quad (67)$ |
| | $m_{2oc} h_{2oc} = m_{3oc,int-oc} h_{3oc,int-oc} + Q_{int-oc} \quad (68)$ |
| | $m_{2oc} e_{2oc} = m_{3oc,int-oc} e_{3oc,int-oc} + e_{Q_{int-oc}} + E_{d_{int-air-oc}} \quad (69)$ |

RESULTS AND DISCUSSION

The power generated in the combined system and the increase in the compressor unit pressure affect the power generated in the low-pressure turbine. The compressor unit was therefore considered as two stages. However, since the low-pressure compressor pressure, r_{pk1} , was limited by the limit values under the supercharged conditions of the diesel cycle, the performance of the combined system was scrutinized based on the changes in this parameter.

The limit power values that could be obtained in the combined system in the r_{pk1} increases based on the selected r_{pk} values are presented in Fig. 3.

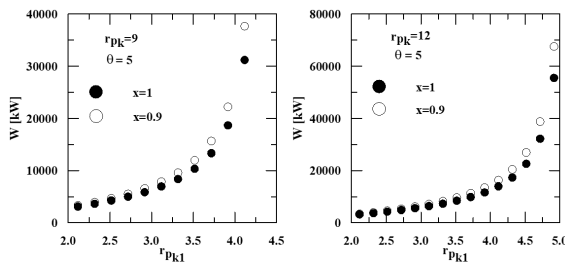


Figure 3. The change in the combined power system in various r_{pk} values based on power and low-pressure compressor r_{pk1} pressure ratio.

The power generated in the combined system is directly associated with the mass flow rate of the air circulating in the system. Therefore, the power generated in the combined system is based on the design of the gas turbine group in addition to the power of the selected diesel engine. In the present study, the turbocharged diesel unit (low-pressure compressor and low-pressure turbine) operating with a split shaft, and a high-pressure turbine group (gas generator) that drives the compressors were modeled as a combined system. As seen in Fig. 3, the decrease in the combined system pressure ($P3/P1$) leads to a decrease in the generated power, which is directly associated with the mass flow of the air circulating in the system and decreases at this value. However, the supercharged operating conditions of the diesel engine determine a low-pressure compressor ratio r_{pk1} for each r_{pk} value. It is possible to observe the performance of the intake-air-cooled combined systems based on the cooling efficiency parameter x in the same figures. Here, the magnitude and significance of the effect of intake-air cooling on power generation could be observed. For $r_{pk1} = 3.5$, the increase in power increase was about 15%. The difficulty of the implementation of $x=0.8$ value determined in the present study is obvious.

As seen in Fig. 4, the thermal efficiency of the combined system also reached a maximum value based on the pressure ratio of the low-pressure compressor in the intake air cooled combined system too. In contrast, the thermal efficiency of the inlet air-cooled composite system decreased as the

low pressure compressor pressure ratio r_{pk1} increased. Similarly, the lower the pressure ratio of the compressor unit the lower the thermal efficiency of the combined system. Based on the same figures, it was determined that the use of a recuperator increased the thermal efficiency in the combined cycle with a recuperator and with and without intake-air cooling; however, it did not effect on the thermal efficiency when the compressor unit pressure was lower than a certain value ($r_{pk1}=7$).

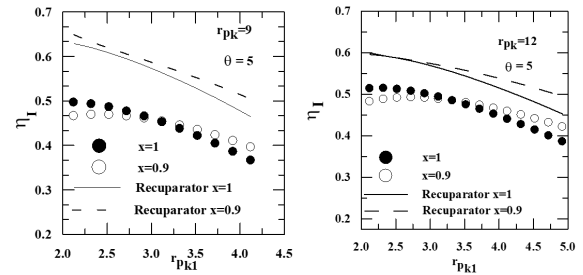


Figure 4. The variations in the combined power system based on thermal efficiency in various r_{pk} values and low-pressure compressor r_{pk1} pressure ratio.

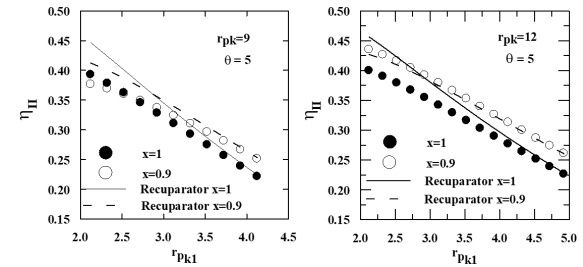


Figure 5. The variations in the combined power system based on exergy efficiency in various r_{pk} values and low-pressure compressor r_{pk1} pressure ratio.

In Fig. 5, the low-pressure compressor also decreased with the increase in pressure ratio r_{pk1} in the proposed model introduced in the second law efficiency of the combined system. The change in the total fuel consumption mass flow rate in the combined system based on r_{pk1} is presented in Fig. 6. The total fuel mass flow rate is presented in Fig. 6 for r_{pk} values of 9 and 12 where it was higher for each r_{pk1} value when compared to other proposed models with intake air cooling. Similar variations were identified for other compressor pressure ratios as well.

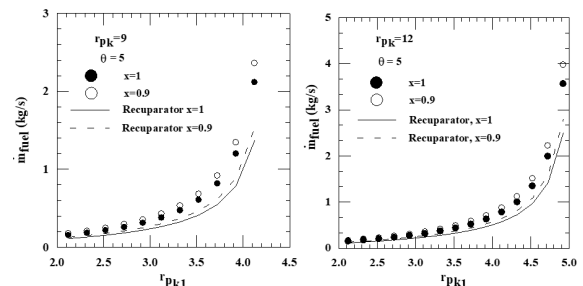


Figure 6. The variations in r_{pk1} with fuel mass flow for $r_{pk}=9$ and $r_{pk}=12$ in combined power system

The increase in generated power with the increase in fuel/air ratio β for each r_{pk} value in the combined system is presented in Fig. 7.

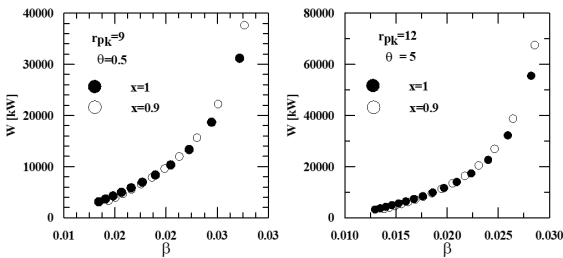


Figure 7. The variations in fuel/air ratio β for various r_{pk} values in the combined power system

The variations in thermal efficiency for various r_{pk} values in the air pre-cooled and without pre-cooled combined power systems based on the air-fuel ratio are presented in Fig. 8.

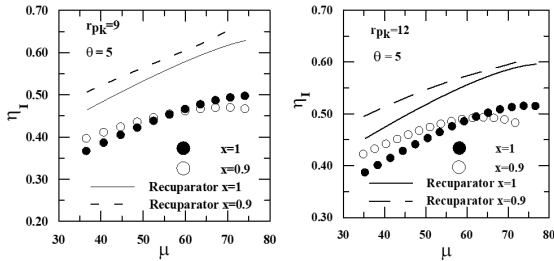


Figure 8. The variations in thermal efficiency for various r_{pk} values in the combined power systems based on the air-fuel ratio

In Fig. 9, it was observed that the low-pressure compressor increased with the increase in the pressure ratio μ in the operating modes introduced in the second law efficiency of the combined system.

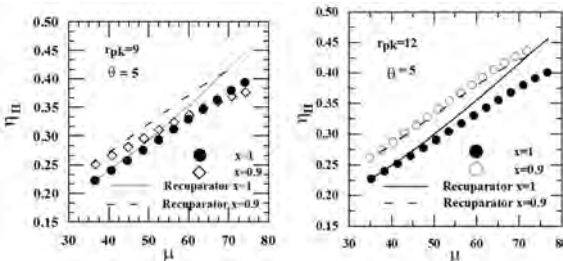


Figure 9. The changes in exergy efficiency and air/fuel ratio in the combined power system for various μ values

The variations in average effective pressure with r_{pk1} in the diesel engine are presented in Fig. 10. Based on the figure, the power was directly proportional to the supercharging pressure. The changes in the ratio of the fuel mass flow rate in the turbine combustion chamber to the total fuel consumption mass flow rate based on r_{pk1} are presented in Fig. 11. The review of Fig. 12 demonstrated that recuperator use was beneficial for fuel efficiency in all proposed models.

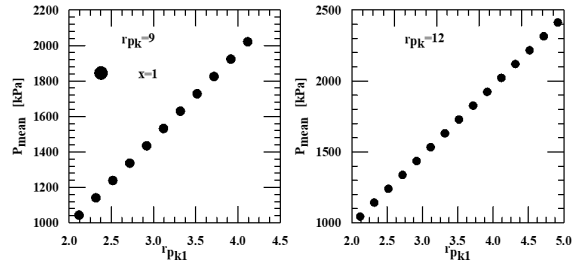


Figure 10. The variations in average effective pressure with r_{pk1} in the diesel engine

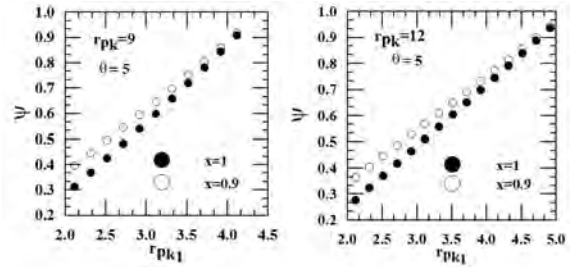


Figure 11. The ratio of the mass flow rate of the fuel used in the turbine combustion chamber to the mass flow rate of the total fuel consumption, change according to r_{pk1}

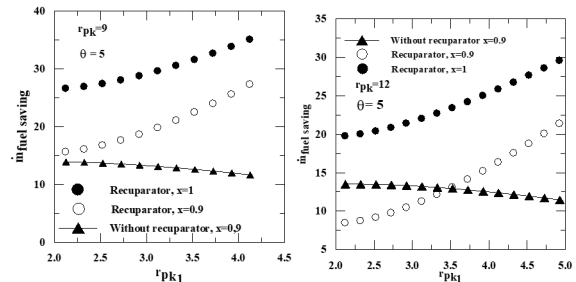


Figure 11. Fuel savings for r_{pk} values in the combined system variation with respect to r_{pk1}

CONCLUSION

In the introduced combined cycle, it was demonstrated that the inlet air was an effective solution to meet the peak power requirements in hot climate conditions. It was also demonstrated that the air pressure required for the supercharge operation in the diesel engine could be supplied by a compressor unit. The first of the compressor groups utilized in the combined cycle was the low-pressure compressor and it was demonstrated that the use of the diesel exhaust mixture of the gas generator energy waste in the low-pressure turbine increased the power generated by the combined system when the pressure rate is selected to prevent the combustion in diesel engine supercharge conditions. It was observed that the generated power increased under the highest pressure and atmospheric pressure conditions used in the cycle at higher r_{pk} values; however, the limit values of the generated power reached the optimum value under the diesel engine supercharged combustion conditions that limited

r_{pk1} pressure ratio. In contrast, the efficiency of the combined cycle decreased with an increase in r_{pk1} .

The second law efficiency of the combined system exhibited a decrease with the increase in the low-pressure compressor pressure ratio. The increase in r_{pk1} led to supercharge in the diesel cycle, hence to an increase in irreversibility, increasing the exergy destruction in the high-pressure compressor, combustion chamber, exhaust gas mixture, and low-pressure turbine, leading to a decrease in the second law efficiency of the combined cycle.

It was observed that the compressor intake-aircooling increased power generation in the combined power system with compressor inlet air cooling, and it increased the second law efficiency, although it had no significant impact on the first law efficiency.

In cycle models with a recuperator, the improvements in the first and second law efficiencies were significant and the recuperator application criterion was dependent on the r_{pk} . The maximum average effective pressure achievable in the diesel engine is around 2500 kPa. The amount of fuel consumed in the gas turbine combustion chamber in the pre-cooled combined cycle was approximately 10% higher when compared in the without pre-cooled combined cycle.

The use of a recuperator in the combined cycle could provide increased fuel saving based on the r_{pk1} values in the combined system. Furthermore, the fuel-saving in the pre-cooled cycle was at the lowest values.

SYMBOLS

| | |
|--------------|--|
| c_p | Specific heat at constant pressure [kJ/kgK] |
| c_v | Specific heat at constant volume [kJ/kgK] |
| exp | Expansion |
| \dot{m} | Mass flow rate [kg/s] |
| R | Gas constant for air [kJ/kgK] |
| r_p | Pressure ratio |
| T | Temperature [K] |
| P | Pressure [Pa] |
| \dot{W} | Power [kW] |
| η | Efficiency [%] |
| θ | The ratio for the turbine inlet temperature to the atmospheric air temperature |
| ϵ_y | Pressure loss in percentage |
| ψ | Expansion coefficient for exhaust gas |
| x | The ratio for the cooling air temperature to the atmospheric air temperature |
| ABK | Low-pressure compressor |
| YBK | High-pressure compressor |

| | |
|-------|---------------------------------|
| HPT | High-pressure turbine |
| LPT | Low-pressure turbine |
| atm | Atmosphere |
| D | Diesel |
| Int | Inter |
| k | The ratio of the specific heats |
| oc | Cold air |
| recup | Recuperator |
| turbo | Turbocharge |
| y | Fuel |
| Cb | Combustion chamber |

References

1. Khana MN, Tililil I. New advancement of high performance for a combined cycle power plant: Thermodynamic analysis. *Case Studies in Thermal Engineering* 12 (2018) 166–175.
2. Descombes G, Boudigues S. Modelling of waste heat recovery for combined heat and power applications. *Applied Thermal Engineering Elsevier* 29, 13 (2009) 2610. DOI:10.1016/j.applthermaleng.2008.09.019.
3. El-Awad MM, Siraj MA. A Combined Diesel-Engine Gas-Turbine System for Distributed Power Generation. *International Conference on Chemical, Biological and Medical Sciences (ICCBMS)*, Kuala Lumpur Malaysia, 2012
4. Altosole M, Benvenuto G, Campora U, Laviola M, Trucco A. Waste Heat Recovery from Marine Gas Turbines and Diesel Engines. *Energies*. 10 (2017) 1–24.
5. Dzida M, Mucharski J. On the possible increasing of efficiency of ship power plant with the system combined of marine diesel engine, gas turbine and steam turbine in case of main engine cooperation with the gas turbine fed in parallel and the steam turbine. *Polish maritime research*. 16 (2009) 40–44.
6. Durmusoglu Y, Kocak G. Exergetic efficiency analysis of a combined power plant of a container ship. *Journal of Thermal Engineering*, 5 (2019) 1–13.
7. Dzida M. Possible efficiency increasing of ship propulsion and marine power plant with the system combined of marine diesel engine, gas turbine and steam turbine. *Advances in Gas Turbine Technology*. (2011) pp. 45–68. DOI:10.5772/24018.
8. Al Madani H. Gas turbine performance enhancement by intake air cooling. *International Journal of Exergy*, 3 (2006) 164–173.
9. Ibrahim TK, Rahman MM, Abdalla N. Improvement of gas turbine performance based on inlet air cooling systems: A technical review. *International Journal of Physical Sciences*. 6 (2011) 620–627.
10. Kumar A., Sanjay M. and Prasad L. Parametric analysis of cooled gas turbine cycle with evaporative inlet air cooling. *International Journal of Scientific & Engineering Research*. 3 (2012) 3, 1–8.
11. Zaki GM, Jassim RK, Alhazmy MM. Energy, exergy and thermoeconomics analysis of water chiller cooler for gas turbines intake air cooling. *Smart Grid and Renewable Energy*. 2 (2011) 190–205.

12. Stone R. Introduction to Internal Combustion Engines. The Mac Millan Press LMTD. 1992.
13. Çengel YA, Boles BA. Thermodynamics and Engineering Approach. McGraw Hill-Science, 6th edition. 2001.
14. Mohammadkhani F, Khalilarya SH, Mirzaee I. 2012. Energetic and Exergetic Analysis of Internal Combustion Engine Cogeneration System. The Journal of Energy: Engineering & Management. 2 (2012) 4 24-31.
15. Reddy S.S.K., Pandurangadu V. and S.P.A. Hussai S.P.A. Effect of turbo charging on volumetric efficiency in an insulated diesel engine for improved performance. International Journal of Modern Engineering Research (IJMER). 3, (2013) 2 674-677.
16. Ebrahimi R. Thermodynamic modelling of performance of an irreversible Diesel cycle with engine speed, ature and Science. 7 (2009) 9 78-82.
17. Qian JY, Zhang Y, Zhuge W. Air supply system design of a diesel_brayton combined cycle. Proceedings of the Institution of Mechanical Engineers, Part A: Journal of Power and Energy. (2018) <https://doi.org/10.1177/0957650918810133>
18. Sreedharan H, Reshma JR, Jacob JK, Sivakumar VV. Energy and exergy analysis on 350 MW combined cycle power plant. European Journal of Technology and Design. 12 (2016) 2 72-78.
19. Abuşoğlu A, Kanoğlu M. Exergetic and thermoeconomic analyses of diesel engine powered cogeneration: Part 1- Formulations. Journal of Applied Thermal Engineering. 29 (2009) 234-241.
20. Karali R, Öztürk İT. Efficiency improvement of gas turbine cogeneration systems. Improving the efficienc of gas turbine cogenartion systems. Technical gazette 25 suppl 1 (2017), 21-27. DOI: 10.17559/TV-20140509154652
21. Karaca, S. 2015. Application of energy and exergy analysis due to different angles of propeller blades to a turbocharged diesel engine vessel. Master thesis. Karadeniz Technical Iniversity, Trabzon.

Comparison of Thermal Performance of Newly Produced Lightweight Wall and Roof Elements for Energy-efficient Buildings

Hasan Oktay¹  Recep Yumrutas²  Zeki Argunhan³ 

¹Batman University, Department of Mechanical Engineering, Batman, Turkey

²Gaziantep University, Department of Mechanical Engineering, Gaziantep, Turkey

³Bitlis Eren University, Department of Mechanical Engineering, Bitlis, Turkey

ABSTRACT

In this study, both experimental and theoretical investigations are performed to obtain new concrete types with high thermal insulating characteristics for energy-efficient buildings. In this regard, 102 new concrete wall samples were produced using different aggregates at different volume fractions, and their thermophysical properties were tested according to EN and ASTM standards. The experimental research focused on developing new wall or roof types with higher thermal insulation properties in order to reduce the energy consumption of buildings due to heating or cooling. In order to specify the thermal performance of developed lightweight concretes, an analytical solution method is developed by the Complex Finite Fourier Transform (CFFT) method to estimate heat gain utilizing measured thermophysical properties data of those samples. The results indicated that the reduction in heat gain value was obtained as 83.21 % for the PC100 wall corresponding to conventional concrete. Consequently, the thermal insulation effect of those samples shows excellent potential for development.

Keywords:

Energy-efficient buildings, Concrete, Heat gain, Thermophysical properties, CFFT

INTRODUCTION

The building sector is responsible for the enormous amount of total energy consumption in the World. Most of this energy is used for the provision of heating and cooling applications. The main objective of a cooling or heating system is to maintain the thermal comfort conditions to the occupants of the building that are required for indoor products and processes. The heat ratio that must be removed from a room to maintain a stable temperature at the comfort level is defined as a cooling load [1]. The heat gain through the building envelope, which includes roofs and walls in most buildings, constitutes a significant partition of the overall cooling load of space due to its large area [2]. If the structures having appropriate thermal properties are selected, also accurate cooling load calculation is performed, and then suitable HVAC system components can be selected. Therefore, estimation of the cooling load through the building envelope is an essential task in the selection of proper components of an HVAC system that influences the building's performance. However, an accurate calculation of the cooling load is quite complicated

and time-consuming due to the thermal storage effects of a building thermal mass and continuously changing outdoor climatic conditions [3].

In literature, several methods have been developed to calculate the cooling load due to heat gain through the envelope such as transfer function method (TFM), heat balance method (HB), total equivalent temperature difference method (TETD), and cooling load temperature difference (CLTD) method. TFM, which is widely used in HVAC industry [4], uses a set of design types with recalculated conduction transfer functions (CTF) coefficients tabulated for certain types of walls, ceilings, and floors handbook of ASHRAE [5]. The calculation of heat gain by the CLTD method is provided by multiplying the UA value of a building envelope with the CLTD values obtained by using the HB or TFM technique. It is limited by the data for specific constructions used in North America with particular external conditions [2]. On the other hand, Complex Finite Fourier Transform (CFFT) is a new model and analytically provides a transformation of the problem into a form that leads to

Article History:

Received: 2019/11/19

Accepted: 2020/03/17

Online: 2020/03/26

Correspondence to: Hasan Oktay,
Batman University, Department of
Mechanical Engineering, Batman, Turkey
Tel: +90 488 217 3991
Fax: +90 488 217 3502
E-Mail: hasan.oktay@batman.edu.tr

a transient solution. Zainal and Yumrutas [6] used the CFFT technique to find the CLTD values numerically for multi-layered roofs and walls. A one-dimensional solution to the transient problem is a new approach to estimate CLTD values. By the way, CFFT is applicable for any possible building structure and ever-changing outdoor climatic conditions, and also it does not require the tables.

Concrete is the most widely used construction material in the world due to its internal functionality and the presence of raw materials used in its production [7-8]. It is essential to improve the thermophysical properties of concrete to reduce the heating and cooling energy consumption of buildings. The important thermophysical properties for heat-transfer processes of a building are density, specific heat, thermal conductivity, and thermal diffusivity. Notably, a low conductivity is required due to the ability to provide thermal insulation, and high specific heat is required due to the ability to retain heat [8]. Besides, the thermophysical properties of concrete depend on moisture content, type, and proportion of aggregate and cement materials [9,10]. Since aggregates generally comprise about 70-80% of the concrete volume, these materials can be expected to have a more significant effect than other parameters [11]. Many studies have discussed in literature about the influences of type and proportion of aggregate on thermophysical properties of concrete. An experimental study [12] was carried out with several types of aggregates to investigate the influence of the aggregate on the thermal properties of concrete. Results showed that concrete containing pieces of calcined clay bricks showed a lower thermal conductivity, but a higher specific heat than concrete containing stone chips. Besides, the thermal conductivity of produced concretes was directly proportional to their thermal diffusivities. Różycka and Pichór [13] studied the effect of perlite waste addition on the properties of autoclaved aerated concrete. The results showed that due to its high insulation properties, expanded perlite waste could potentially be used as a replacement in the production of autoclaved aerated concrete. Benazzouk et al. [14] were conducted a study about the influence of waste rubber particles on the thermal properties of concrete. The results indicated that the addition of rubber particles to concrete reduces thermal conductivity and density. Kilincarslan et al. [15] reported that the addition of pumice to foam concrete reduces thermal conductivity and bulk density. Besides, many studies have been revealed that thermal insulation characteristics of masonry materials are improved by introducing various amounts of lightweight and synthetic aggregates and also some additives [16–18]. Although many researchers have studied the thermal properties of concretes containing different types of lightweight aggregates, there has not been much in the literature to identify the effects of insulation properties for a given climate.

In this study, experimental and theoretical studies are performed. The experimental research focused on developing new wall or roof types with higher thermal insulation properties in order to minimize the energy consumption of buildings. The calculation method for the cooling load used in the study is based on the solution of the periodic heat transfer problem in order to obtain the temperature distribution of the multilayer wall or flat roof structures.

MATERIAL AND METHODS

Several materials were used to obtain different lightweight building wall or roof elements. The materials were locally available fine aggregate, coarse aggregate, ordinary Portland cement, mineral admixtures such as silica fume, superplasticizers, and lightweight aggregates such as rubber aggregate (RA), pumice aggregate (PA) and expanded perlite aggregate (EPA). The concrete mixtures were prepared with a constant water-cement ratio of 0.48 and total cement content of 350 kg/m³. The value of 0.48 was selected for providing desired consistency in the mixtures [19]. Then, aggregates were replaced by RA, EPA, and PA at different volume fractions (10%, 20%, 30%, 40%, 50%, and 100%) of the total aggregate volume. Besides, a control mix with no replacement of the light-weight aggregate was produced to make a comparative analysis. The chemical composition of the materials used in the study and mix proportions are detailed in Ref. [20]. During the mixing process, the target air content was established at 2% for the control concrete and 6% for the air-entrained concrete. The same series of calculations accomplished by the volume to weight conversions for aggregates. The actual material quantities were then calculated by using the following equations:

$$V_a = 1 - \left(\frac{C}{\delta_c} + \frac{W}{\delta_s} + h + k \right) \quad (1)$$

$$W = \left(\frac{E}{C} \right) \times C \quad (2)$$

$$G_i = V_a \times P_i \times \delta_i \quad (3)$$

where V_a is total aggregate volume in concrete (m³), C is weight of cement (kg), W is weight of water (kg), h is targeted air volume in concrete (m³), k is admixtures volume in concrete (m³), E/C is effective water/cement ratio, δ_c and δ_i are specific gravity of cement and aggregates (kg/m³), respectively. Then, the concrete mixes were prepared in a laboratory in the following order:

- Firstly, PA and EPA were pre-wetted for 30 min.
- Secondly, one-third of water and light-weight aggregate were mixed.

- Thirdly, cement, mineral admixtures were mixed with remaining water.
- Finally, stirring was continued until a uniform concrete was produced.

The mixture was first mixed for 5 min in a mixer and then placed in the mold, and it was adequately compacted for 2 min on a vibration table (Fig. 1). The mixtures were produced as expanded perlite concrete (EPC), rubberized concrete (RC), pumice concrete (PC), normal concrete (NC), air-entrained concrete (AEC) and the numbers as 10, 20, 30, 40, 50 and 100 show the percentage of replacement. In total, 102 concrete samples were produced, and their mechanical tests such as the compressive strength (ASTM C39, as shown in Fig. 2), bulk density (ASTM C138) and porosity tests (ASTM C1202-12) were performed in accordance with ASTM standards on air-dry samples aged 28 days (ASTM C330-99). The minimum strength requirements for building blocks are most commonly set at 2.5 MPa [21]. Therefore, the produced samples whose compressive strengths are under the limit were not included in the study (EPC100 and RC100 were not cased).



Figure 1. Vibrating Table



Figure 2. The compressive strength test (ASTM C39)

In order to establish thermophysical properties of the concretes, thermal conductivity, thermal diffusivity, and specific heat tests were performed by transient plane source technique (TPS) according to EN 12667. The advantage of the TPS method compared to stationary or steady-state methods is to determine a full set of thermophysical properties within a single measurement. The values of the thermal property device range for measuring parameters are given in Table 1. ISOMET 2104 device was used to measure the thermal property of concrete samples based on the transient plane source method, as indicated in Fig. 3.

Table 1. Values of device range for measuring parameters

| Measurement property | Measurement range | Accuracy |
|------------------------|--|---|
| Thermal conductivity | 0.015–6 W/mK | 5 % of reading ± 0.001 W/mK |
| Specific heat capacity | 4×10 ⁴ – 4 ×10 ⁶ J/m ³ K | 15 % of reading ± 1.103 J/m ³ K |
| Thermal diffusivity | 4×10 ⁻⁵ – 4 ×10 ⁻⁸ m ² /s | 10 % of reading ± 0.1 ×10 ⁻⁸ m ² /s |
| Operating temperature | From -20 – +70 °C | 1°C |



Figure 3. The measurement devices of the thermal property

Formulation of Heat Transfer Problem

In order to decide whether any one of the building wall or roof elements is the best or not due to heat transfer, it is necessary to compare heat gain or loss for these elements. In this study, at first, the heat gain values through the produced wall or roof structures are estimated, and then the estimated heat gain values for each element are compared with other building elements. Since the magnitude of energy consumption in heating and cooling of any space is extremely important for humanity or environment protection or pollution, any element or elements having the lowest heat gain values are recommended to applicants.

Heat gain, q_c (W/m²) through indoor space of a building from exterior walls or roofs can be calculated using the inner wall surface, room temperature, T_r and combined convection heat transfer coefficient at the inner surface, h_i :

$$q_c = h_i [T_1(0,t) - T_r] \quad (4)$$

In the present study, inner surface temperature, $T_1(0,t)$ is a function of coordinate and time obtained from a general solution of transient heat transfer problem. The building wall or roof consisting of N layers is shown in Fig. 4.

Formulation of periodic heat transfer from a building structure to a room is presented as the following partial equations under given boundary conditions:

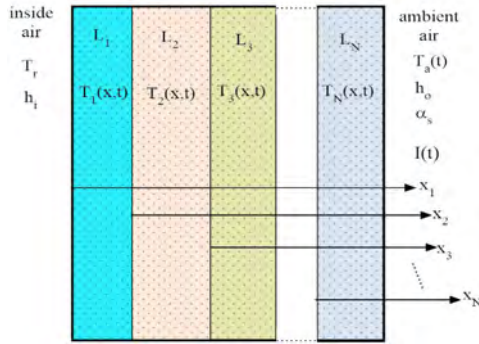


Figure 4. Schematic view of a multilayer wall or flat roof

$$\frac{\partial^2 T_n}{\partial x_n^2} = \frac{1}{\alpha_n} \frac{\partial T_n}{\partial t} \quad 1 \leq n \leq N \quad (5)$$

$$h_i (T_r - T_1) = -k_1 \frac{\partial T_1}{\partial x_1} (x_1 = 0) \quad \text{at } X_1 = 0 \quad (6)$$

$$k_{n-1} \frac{\partial T_{n-1}}{\partial x_{n-1}} (x_{n-1} = L_{n-1}) = k_n \frac{\partial T_n}{\partial x_n} (x_n = 0) \quad 2 \leq n \leq N \quad (7)$$

$$T(x_{n-1} = L_{n-1}) = T(x_n = 0) \quad 2 \leq n \leq N \quad (8)$$

$$-k_N \frac{\partial T_N}{\partial x_N} (x_N = L_N) = h_o [T_N - T_e(t)] \quad \text{at } X_N = L_N \quad (9)$$

$$T_e(t) = T_a(t) + \frac{\alpha_s I_t(t)}{h_o} - \frac{R}{h_o} \quad \text{at } X_N = L_N \quad (10)$$

where ΔR is the difference between the long-wave radiation incident from the sky and the radiation incident emitted by a blackbody at the ambient air temperature. ASHRAE recommends the correction factor, $\epsilon \Delta R / h_o$ to be given a value of 4°C and 0°C for horizontal surfaces and vertical surfaces, respectively.

The heat transfer problem consists of Eqs. (5)–(10) is transformed into dimensionless formulations, and then CFFT is applied to obtain the general solution of the problem and is expressed as:

$$T_n(z_n, \tau) = \sum_{j=-M}^M T_{nj}(z_n) e^{i\omega_j \tau} \quad \omega_j = 2\pi j \quad (11)$$

where $T_1(0, t)$ is the inner surface temperature of the roof or wall obtained from Eq. (8) at $z_n = 0$ and expressed as:

$$T_1(0, t) = \sum_{j=-M}^M T_{1j}(0) e^{i\omega_j \tau} \quad \text{at } Z_n = 0 \quad (12)$$

where $T_{1j}(0)$ is a dimensionless parameter. Its expression and calculation procedure are presented in Yumrutaş et

al. [1,3]. $T_n(z_n, \tau)$, given by Eq. (11), is a periodic solution of the temperature distribution in a wall and is obtained as a function of solar radiation incident on a tilted surface and ambient air temperature, $T_a(t)$. $I_1(t)$ is the intensity of solar radiation incident falling on the unit area and can be defined as a sum of the diffuse, beam, and reflected radiation [22].

$$I_T(t) = I_b(t)R_b + I_d(t) \left(\frac{1 + \cos \beta}{2} \right) + I(t)\rho_g \left(\frac{1 - \cos \beta}{2} \right) \quad (13)$$

where $I_d(t)$ and $I_b(t)$ are diffuse and beam radiation on a horizontal surface. ρ_g is ground reflectance and taken as 0.2 in the present study. Geometric factor, R_b can be calculated for vertical surfaces ($\beta = 90^\circ$) as;

$$R_b = \frac{\cos \delta \sin \phi \cos \gamma \cos \omega + \cos \delta \sin \gamma \sin \omega - \sin \delta \cos \phi \cos \gamma}{\cos \phi \cos \delta \cos \omega + \sin \phi \sin \delta} \quad (14)$$

where, ϕ , ω , γ and δ are the latitude, hour, azimuth and declination angles, respectively [22].

COMPUTATIONAL PROCEDURE

In order to find the best-produced sample in terms of heat transfer, heat gain through the samples is estimated by utilizing the solution of transient heat transfer problem for a wall or roof. In this regard, a computer program in MATLAB was prepared by using climatic data, which are hourly ambient air temperature and solar radiation on a horizontal surface, and thermophysical properties of the produced samples. The climatic data were obtained at the meteorological stations for Gaziantep province (latitude: 37.04°N , longitude: 37.31°E) on July 21. By utilizing the program, hourly solar radiation incident on a vertical surface with different direction is calculated by using Eq. (13). The room temperature, the inner and outer surface combined heat transfer coefficients are taken as 25°C , 8.3, and $17 \text{ W/m}^2\text{C}$, respectively. Solar absorptivity α_s , which depends on the external face color of a building envelope, is assumed to be 0.8 (dark-colored surface). The hourly sol-air temperature and the other constant parameters were given as input data. When the program is first executed, the hourly sol-air temperature in Eq. (10) is computed, and then the inner surface temperature and heat gain through the wall or roof are computed by Eqs. (12) and (4), respectively.

RESULTS AND DISCUSSION

Both experimental and theoretical investigations are performed in this study to find the best wall or roof material

Table 2. Mechanical and thermal properties of produced concrete samples.

| Types of concrete | Compressive strength σ (MPa) | Bulk density, ρ (kg/m ³) | Thermal conductivity k (W/m K) | Specific heat c (J/kg K) | Thermal diffusivity α (mm ² /s) |
|-------------------|--|--|-------------------------------------|-------------------------------|--|
| NC | 51.85 | 2345.09 | 1.96 | 709.07 | 1.18 |
| AEC | 48.11 | 2288.86 | 1.91 | 712.14 | 1.17 |
| EPC10 | 31.21 | 2139.09 | 1.51 | 725.48 | 0.97 |
| EPC20 | 19.02 | 1885.52 | 1.22 | 779.63 | 0.83 |
| EPC30 | 10.01 | 1559.44 | 0.70 | 865.69 | 0.52 |
| EPC40 | 8.15 | 1376.56 | 0.50 | 922.59 | 0.40 |
| EPC50 | 4.88 | 1168.63 | 0.36 | 966.95 | 0.32 |
| PC10 | 33.46 | 2005.34 | 1.54 | 772.42 | 0.99 |
| PC20 | 23.39 | 1851.02 | 1.29 | 818.52 | 0.85 |
| PC30 | 13.07 | 1559.95 | 0.76 | 903.87 | 0.54 |
| PC40 | 9.90 | 1400.72 | 0.54 | 949.51 | 0.41 |
| PC50 | 9.51 | 1329.97 | 0.41 | 991.80 | 0.31 |
| PC100 | 5.24 | 721.49 | 0.16 | 1221.85 | 0.18 |
| RC10 | 42.04 | 2244.30 | 1.72 | 721.83 | 1.06 |
| RC20 | 30.41 | 2148.07 | 1.44 | 737.70 | 0.91 |
| RC30 | 19.04 | 2033.93 | 1.22 | 761.20 | 0.79 |
| RC40 | 9.51 | 1874.62 | 0.89 | 808.93 | 0.58 |
| RC50 | 4.53 | 1644.98 | 0.62 | 868.16 | 0.43 |

from produced samples. In the experimental study, new lightweight concrete samples having adequate strength and relatively high thermal insulation properties were produced for energy efficiency. The experimental test results for the thermal diffusivity, compressive strength, bulk density, specific heat, and thermal conductivity are tabulated in Table 2. The experimental results given in Table 2 are obtained based on the average of five tested values with \pm a tolerance limit (less than 2%) for each property test. In the theoretical study, the surface temperature of the samples and heat gain values through the structures are calculated by an analytical model utilizing a program in MATLAB. The heat gain calculations are performed for different building structures, and the schematic view of the configurations used in this study is represented in Fig. 5.

In order to evaluate possible correlations between measurement values of the thermophysical properties of building structures, multivariate regression is performed on the dataset of 102 concrete samples (Table 2) using the free statistical software found in Microsoft Excel. A vital correlation given by Eq. (15) was obtained by using the measurement results of thermal conductivity and thermal diffusivity, as depicted in Fig. 6. It is observed that there is a nearly linear relation between the values of thermal diffusivity and conductivity of produced concrete samples and can be expressed by the equation with $R^2=0.99$:

$$k = 2 \times 10^6 \alpha - 0.1845 \quad (15)$$

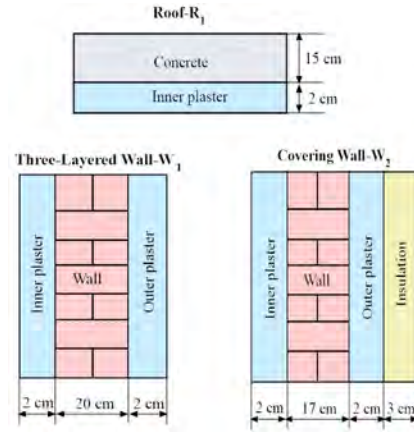


Figure 5. Schematic view of a multilayer wall or flat roof configurations used in this study

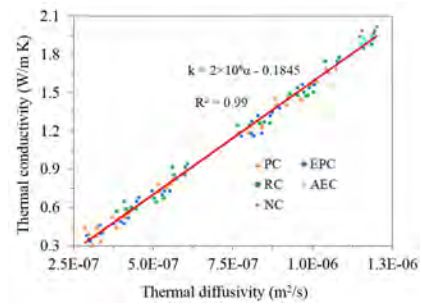


Figure 6. Relationship between the thermal diffusivity and the thermal conductivity obtained experimental study

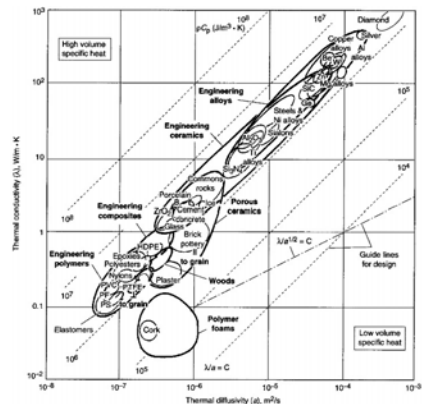


Figure 7. A comprehensive list of building materials: thermal conductivity is plotted against thermal diffusivity for room temperature [23]

Besides, the results obtained in the present study were compared with similar studies in the literature (Fig. 7). Thermal conductivity is plotted against the thermal diffusivity for a comprehensive list of building structures [23]. It can be concluded that the relations obtained from this study have a similar tendency to those relations reported in the literature, and covered all other building structures.

In order to estimate temperature distributions on a wall or roof surface, sol-air temperature values should be

calculated by using hourly ambient air temperature and solar radiation incident on a horizontal surface. Fig. 8 presents the daily variation of sol-air temperatures due to horizontal and vertical surfaces for the city of Gaziantep. The sol-air temperature values of walls and roofs due to the North, East, West, and South directions are calculated from the Eq. (10) by using the measurement values. The calculated sol-air temperature values for all surfaces behave as quasi-symmetric; especially, it can be noticeable in the East and West directions. Besides, it is depicted that values of diffuse radiation for the West are higher than the values for the East. Heat gain fractions in the present study are defined as the ratio of heat gain value of each wall construction to the heat gain value of the reference wall sample.

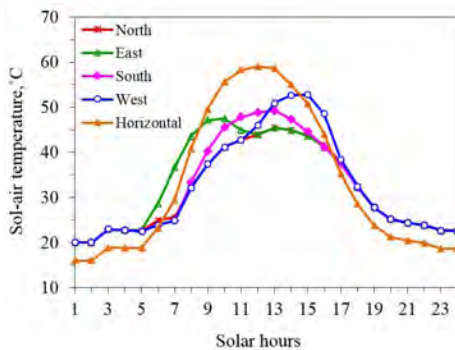


Figure 8. Daily variation of sol-air temperatures due to horizontal and four main vertical surfaces

Fig. 9 shows the variation of heat gain fraction for each wall construction (W1) with respect to aggregate content. It is seen from the results that 83.21 % reduction in heat gain value is obtained using the PC100 wall, corresponding to reference concrete (NC). The lowest value of heat gain results for the lowest thermal conductivity of the PC100 wall. It is understood from the Fig. 9 that the heat gain values for the walls are inversely proportional to the light-weight aggregate ratios. The reduction in heat gain of composites is due to the insulating effect of light-weight aggregate particles having a lower thermal conductivity compared to normal aggregates.

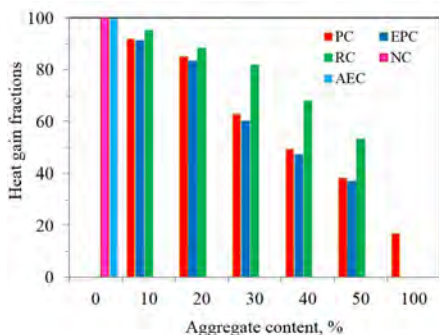


Figure 9. The percentages of max. heat gain fractions for each south-wall construction (W1) with different aggregate content

The results of daily heat gain values through the walls

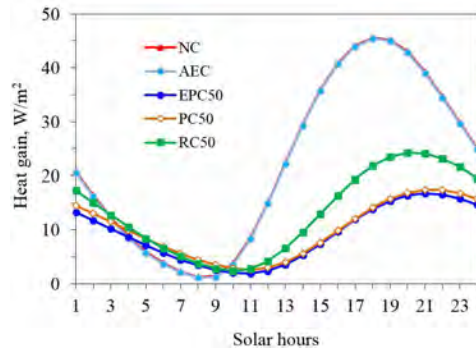


Figure 10. Variation of heat gains for south-facing wall constructions (W1) at the same light-weight aggregate ratios

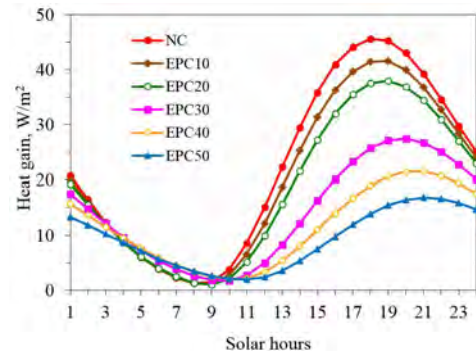


Figure 11. Daily variation of heat gain values of dark-colored NC and EPC walls (W1) with different EPA ratios due to the south direction

(W1) due to south direction are shown in Fig. 10. As shown in this figure, the highest value of heat gain occurs for the NC wall having the highest value of thermal diffusivity and conductivity. The results show that thermal diffusivity and conductivity of the materials have a profound influence on the thermal performance of the structures. Besides, the AEC wall also has the highest amplitude of heat gain value for the design day, and they are reasonably close to those of the NC wall. In these walls, the lowest values of heat gain value are provided for PC50 and EPC50 walls, of which the values are close to each other. It can be seen that the thermal diffusivity of a sample has a profound effect on heat gain since the thermal diffusivity values of NC, AEC, PC50, and EPC50 are 1.18, 1.17, 0.32, and 0.31 mm²/s, respectively. It is evident from Fig. 10 that the utilization of PC50 or EPC50 as a wall or roof material in a building provides a lower heat gain value and maintains a stable temperature at comfort level compared to NC and AEC.

Daily variations of heat gain values for the NC and EPC walls with different EPA ratios are illustrated in Fig. 11. The NC wall has the highest amplitude of the heat gain value, and it is followed by EPC10, EPC20, EPC30, EPC40, and EPC50, respectively. The highest values of heat gain are estimated for EPC50 and NC walls with values of 16.796 W/m² and 45.598 W/m², respectively.

The daily amplitude of inner and exterior surface tem-

perature differences ($\Delta T = T_{ex} - T_m$) for roofs (R1) are shown in Fig. 12. The highest differences in temperature occur in EPC50 roof construction, and the lowest differences in temperature occur in NC roof construction, having the highest value of thermal diffusivity and conductivity. Furthermore, it can be seen from the figure that heat transfer takes place from the room side to outside air before the hour of 6 and after the hour of 19. When solar radiation does not exist or is very low, the temperature difference for all constructions is dropped below 0°C. The reason is that when solar radiation intensity is low, terrestrial objects surfaces usually have a lower temperature than the ambient air; hence, horizontal surfaces receive long-wave radiation from the sky only.

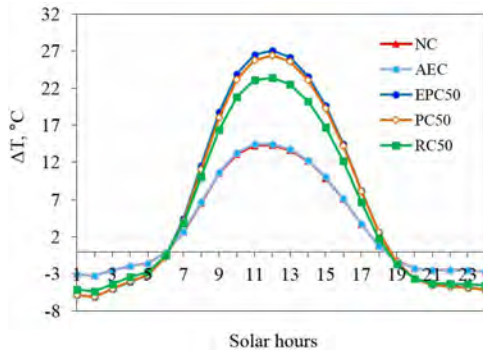


Figure 12. Variation of inner and outer surface temperature differences for roof constructions (R1) at the same light-weight aggregate ratios

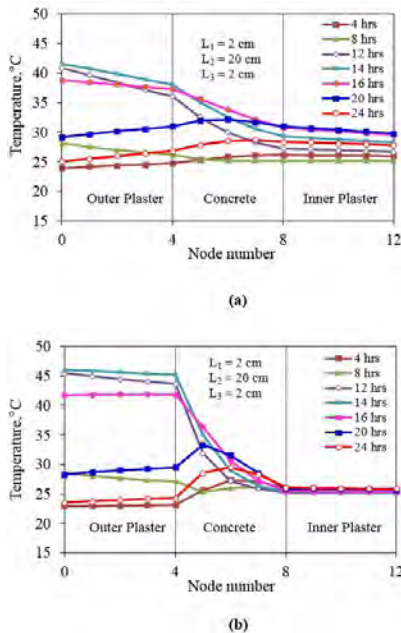


Figure 13. Temperature distributions across the dark-colored walls due to south direction: (a) NC and (b) PC100 walls

Temperature distributions across the NC, EPC50, and PC100 walls (W1) due to the south direction at various time intervals are shown in Fig. 13 for July 21. After heat fluxes across the EPC50 wall, the temperature on the interior plaster is maintained at a constant level of 25-27°C. In the case

Table 3. Thermophysical properties of selected wall and roof materials[1]

| Building materials | Thermal conductivity k (W/m K) | Density ρ (kg/m ³) | Specific heat c (J/kg K) | Thermal diffusivity α (mm ² /s) |
|--------------------|-------------------------------------|--|-------------------------------|--|
| Plaster | 0.700 | 2778 | 840 | 0.30 |
| EPS | 0.038 | 18 | 1500 | 1.40 |
| Briquette | 0.920 | 1600 | 840 | 0.68 |
| Brick | 0.690 | 1580 | 840 | 0.52 |
| Blockbims | 0.230 | 770 | 835 | 0.36 |
| AAC | 0.150 | 400 | 1047 | 0.36 |

of the NC wall, variation of the temperature is unsteady at the interior plaster, and the temperature is maintained at 26-30°C, which is higher than the comfort temperature. When the wall constructed with PC100, a constant temperature of 25°C exists throughout the interior plaster at all the time; thus, it is possible to maintain a constant, comfortable temperature during all the time in a day and for various weather conditions.

Blockbims, brick, briquette, concrete, and autoclaved aerated concrete (AAC) are the most common type of building material used in building construction. The thermophysical properties of these materials are tabulated in Table 3.

In Fig. 14, the highest heat gain values of NC, blockbims, briquette, AAC, brick, and PC100 walls (W1) are compared with respect to wall thickness due to the south direction. The period of the highest heat gain takes place in different hours depending on thermophysical properties and thermal storage capabilities of the building material. For all wall material, the heat gain values decrease since the wall thickness or heat resistance increases. Fig. 14 depicts as to which thickness of NC wall corresponds to the thicknesses of blockbims, briquette, brick, AAC, PC100, or each other. It is observed that heat gain for the PC100 wall with 10 cm thickness corresponds to 29.7 cm of briquette, 14.3 cm of blockbims, 24.7 cm of brick walls. Besides, the value of heat gain for the NC wall with a thickness of 20 cm is equal to the value of heat gain for briquette and brick with the thicknesses of 14.2 cm and 11.9 cm, respectively. The results revealed

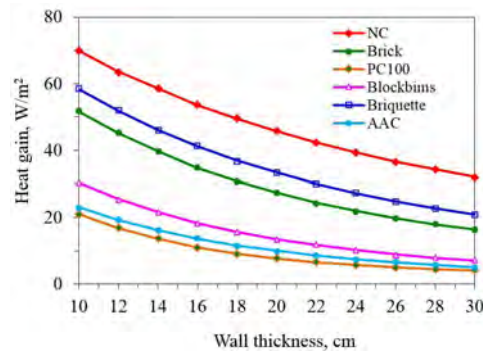


Figure 14. Daily variation of the highest heat gains of selected walls (W1) with respect to their thicknesses due to south direction

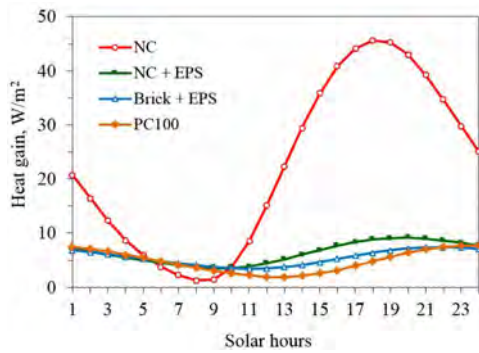


Figure 15. Comparison of the daily heat gain variations of NC wall (W1), PC100 wall (W1), Brick and NC walls with EPS insulations (W3)

that using lightweight structures such as PC100, EPC50 in the building, thermal comfort conditions can be achieved with minimum energy consumption for both winter and summer seasons. It is recommended to all users who use the light-weight concrete constructions in their buildings.

Fig. 15 shows a comparison of the daily heat gain variations of NC wall (W1), PC100 wall (W1), Brick, and NC walls with EPS insulations (W3). Daily total heat gain values are calculated as 535.50 W/m², 152.99 W/m², 130.77 W/m², and 115.21 W/m² for NC wall, NC + EPS wall, Brick + EPS wall and PC100 wall, respectively. It is seen that the thermal performance of the PC100 wall is better than NC, NC + EPS, and Brick + EPS walls. Furthermore, the lowest heat gain values are obtained for the PC100 wall at the hours between 12 and 17 when the ambient temperature is very high. Therefore, when capacity, initial and operating cost of air conditioner systems is thought, light-weight concrete is a very suitable material for both masonry and structural applications.

Fig. 16 is plotted for determining the relation between thermal diffusivity and heat gain, where the program is performed to estimate the daily heat gain values by using Eq. (12) as an input for the wall configuration of W1. As thermal diffusivity increases, the heat gain also increases; thus, for $\alpha=0.3$ mm²/s, the lowest amplitude of the heat gain appears while for $\alpha=1.5$ mm²/s, the highest amplitude of the heat gain value occurs. Furthermore, increasing the thermal diffusivity causes the maximum and the minimum peaks of

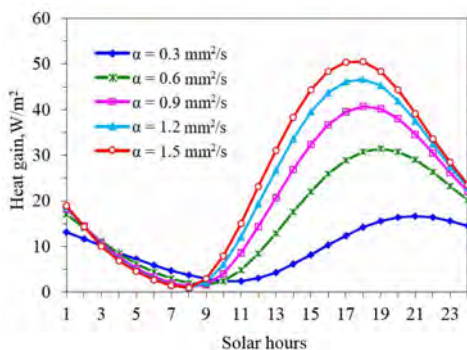


Figure 16. Thermal diffusivity versus heat gain.

the daily heat gain to appear earlier. For $\alpha=0.3$ mm²/s, the minimum and the maximum peaks of the daily heat gain appear at 10 and 21 hrs., respectively. On the other hand, for $\alpha=1.5$ mm²/s, the minimum and the maximum heat gain peaks appear at 8 and 18 hrs., respectively. Hence, for a lower value than $\alpha=0.3$ mm²/s, the minimum peak of the heat gain and the maximum peak of the sol-air temperature coincide; moreover, the maximum peak of heat gain occurs when solar radiation does not exist and that reduces the cooling load efficiently.

Therefore, selecting a material with lower thermal diffusivity and thermal conductivity for a masonry construction can help to reduce the cooling load of a building and capacity of an HVAC system and can maintain comfortable conditions at even higher ambient air temperatures. Since the energy consumption due to heating or cooling of a building system is so enormous, the thermal insulation effect of the elements is so attractive and shows promising potential for development.

CONCLUSION

In this study, experimental and theoretical investigations were both performed to find the best building wall or roof type with high thermal insulating characteristics. The following conclusions can be drawn:

1. Thermal properties of the building materials have a profound impact on the enhancement the heat gain and surface temperature values. In particular, thermal diffusivity is a crucial property, and materials with low thermal diffusivity give the small amplitude of heat gain value. In all types of roofs and walls, the highest and the lowest heat gain value detected for the NC and PC100 walls, respectively.
2. The result of regression analysis indicates that a strong positive relationship ($R^2=0.99$) exists between thermal diffusivity and conductivity values. As thermal diffusivity increases, the heat gain also increases; thus, for $\alpha=0.3$ mm²/s, the lowest amplitude of the heat gain appears while for $\alpha=1.5$ mm²/s, the highest amplitude of the heat gain value occurs.
3. The results indicated that the reductions in heat gain values were obtained as 63.17 % for the EPC50 wall and 83.21 % for PC100 wall with a commonly used thickness of 20 cm, respectively, corresponding to conventional concrete (NC).
4. Daily total heat gain values are calculated as 535.50 W/m², 152.99 W/m², 130.77 W/m², and 115.21 W/m² for NC wall, NC + EPS wall, Brick + EPS wall and PC100 wall, respectively. The results show that the ther-

mal performance of PC100 building material is better than the NC + EPS and Brick + EPS wall constructions.

5. A material with lower thermal conductivity and diffusivity for a masonry construction should be selected for reducing heat gain or loss of a building and capacity of an HVAC system size, and also can maintain comfortable conditions. As a result, cost of the HVAC system and operating cost will be decreased.

NOMENCLATURE

| | |
|----------|--|
| c | specific heat (kJ/kg K) |
| h_i | combined heat transfer coefficient at the inner surface (W/m ² K) |
| h_o | combined heat transfer coefficient at the outer surface (W/m ² K) |
| i, j | complex arguments |
| I_T | radiation heat flux on tilted surface (W/m ²) |
| I_{bT} | beam radiation heat flux on tilted surface (W/m ²) |
| I_{dT} | diffuse radiation heat flux on tilted surface (W/m ²) |
| I_{rT} | reflected radiation heat flux on horizontal surface (W/m ²) |
| k | thermal conductivity (W/m K) |
| L | thickness (m) |
| p | time period (h) |
| t | time (s) |
| T_a | ambient air temperature (°C) |
| T_e | sol-air temperature (°C) |
| T_r | design inside air temperature (°C) |

Greek symbols

| | |
|---------------------------|---|
| α | thermal diffusivity (m ² /s) |
| α_s | absorptance of surface |
| ρ | density (kg/m ³) |
| ω_j | complex frequency |
| δ | declination |
| ε | emissivity of a surface |
| ΔR | difference between long-wave radiation incident on the surface from the sky (W/m ²) |
| τ, τ_n, τ_{np} | dimensionless time terms |
| ρ_g | ground reflectance |
| ω | hour angle |
| ϕ | latitude angle |
| γ | surface azimuth angle |

Subscripts

| | |
|-----|---------------------------|
| AEC | air-entrained concrete |
| EPC | expanded perlite concrete |
| i | inside |
| N | number of layers |
| N | number of the last layer |
| NC | normal concrete |
| o | outside |
| PC | pumice concrete |
| RC | rubberized concrete |

REFERENCES

1. Yumrutaş R, Kaşka Ö, Yıldırım E. Estimation of total equivalent temperature difference values for multilayer walls and flat roofs by using periodic solution. *Building and Environment* 42 (2007) 1878–1885.
2. Bansal K, Chowdhury S, Gopal MR. Development of CLTD values for buildings located in Kolkata, India. *Applied Thermal Engineering* 28 (2008) 1127–1137.
3. Yumrutaş R, Unsal M, Kanoglu M. Periodic solution of transient heat flow through multilayer walls and flat roofs by complex finite Fourier transform technique. *Building and Environment* 40 (2005) 1117–1125.
4. Wang SK. *Handbook of air conditioning and refrigeration*, McGraw-Hill, New York, 2001.
5. ASHRAE. *ASHRAE handbook-fundamentals*, ASHRAE, Atlanta, 1993.
6. Zainal OA, Yumrutaş R. Validation of periodic solution for computing CLTD (cooling load temperature difference) values for building walls and flat roofs. *Energy* 82 (2015) 758–768.
7. ACI Committee 213. *Guide for Structural Lightweight Aggregate Concrete*, American Concrete Institute ISBN: 978-0-87031-897-9, 2014.
8. Yunsheng X, Chung DDL. Effect of sand addition on the specific heat and thermal conductivity of cement. *Cement and Concrete Research* 30 (2000) 59–61.
9. Khan MI. Factors affecting the thermal properties of concrete and applicability of its prediction models. *Building and Environment* 37 (2002) 607–614.
10. Kim K, Jeon S, Kim J, Yang S. An experimental study on thermal conductivity of concrete. *Cement and Concrete Research* 33 (2003) 363–371.
11. Chi JM, Huang R, Yang CC, Chang JJ. Effect of aggregate properties on the strength and stiffness of lightweight concrete. *Cement and Concrete Composites* 25 (2003) 197–205.
12. Howlader MK, Rashid MH, Mallick D, Haque T. Effects of aggregate types on thermal properties of concrete. *ARPN Journal of Engineering and Applied Sciences* 7 (2012) 900–907.
13. Rózycka A, Waldemar P. Effect of perlite waste addition on the properties of autoclaved aerated concrete. *Construction and Building Materials* 120 (2016) 65–71.
14. Benazzouk A, Douzane O, Mezreb K, Laidoudi B, Que'neudec M. Thermal conductivity of cement composites containing rubber waste particles: Experimental study and modeling. *Construction and Building Materials* 22 (2008) 573–579.
15. Kilincarslan Ş, Metin D, Mehmet A. The effect of pumice as aggregate on the mechanical and thermal properties of foam concrete. *Arabian Journal of Geosciences* 11 (2018) 289.

16. Liu MYJ, Alengaram UJ, Jumaat MZ, Mo KH. Liu. Evaluation of thermal conductivity, mechanical and transport properties of lightweight aggregate foamed geopolymer concrete. *Energy and Buildings* 72 (2014) 238-245.
17. Yun TS, Jeong YJ, Han TS, Youm KS. Evaluation of thermal conductivity for thermally insulated concretes. *Energy and Buildings* 61 (2013) 125-132.
18. Paki T, Yesilata B. Physico-mechanical and thermal performances of newly developed rubber-added bricks. *Energy and Buildings* 40 (2008) 679-688.
19. Somayaji, S. *Civil Engineering Materials*, Upper Saddle River: Prentice Hall, ISBN 0-13-083906-X, p. 129, 2001.
20. Oktay H, Yumrutaş R, Akpolat A. Mechanical and thermophysical properties of lightweight aggregate concretes. *Construction and Building Materials* 96 (2015) 217–225.
21. BS 6073-1:1981. *Precast concrete masonry units - Part 1: Specification for precast concrete masonry units*, British Standards Institution, 1981.
22. Duffie JA, Beckman WA. *Solar engineering of thermal process*, Wiley, New York, 1980.
23. ASM International Materials Properties Database Committee, *Thermal Properties of Metals*, ISBN 0-87170-768-3, 2002.

Using the Low Concentrated Photovoltaic Module as a Preheater in an Organic Rankine Cycle

Burak Kursun 

Amasya University, Department of Mechanical Engineering, Amasya, Turkey

ABSTRACT

In concentrated photovoltaic thermal (CPVT) systems, sunlight is directly converted into electricity and during this conversion waste heat is generated on the photovoltaic module. The resulting waste heat can be used for heating the fluids. In this study, the effect of using a low concentrating photovoltaic thermal system as a pre-heater before the evaporator in the organic Rankine cycle (ORC) was investigated. Thermodynamic analyzes were performed for different solar radiation values, concentration ratio values and various photovoltaic module (PV) materials. The increase in solar radiation and concentration increased the electricity production in the photovoltaic module and the thermal efficiency of the system but led to a decrease in exergy efficiency. In the analyzes, four different PV module materials were examined and M-Si and P-Si module materials showed better performance in terms of system efficiency and electricity production.

Keywords:

Concentration ratio, Organic rankine cycle, Photovoltaic cell, Photovoltaic module, Waste heat

Article History:

Received: 2020/01/14

Accepted: 2020/01/30

Online: 2020/03/26

Correspondence to: Burak Kurşun,
Amasya University, Department of
Mechanical Engineering, Amasya,
Turkey

E-mail: burak.kursun@amasya.edu.tr;

Phone: +90 358 211 5005;

Fax: +90 358 260 0070.

INTRODUCTION

Concentrated photovoltaic thermal system (CPVT) technology has an important place among solar energy systems. In CPVT systems, sunlight is directly converted to electricity and during this conversion waste heat is generated on the photovoltaic module. The resulting waste heat can be used to heat the fluids.

Photovoltaic systems are also used in electricity and waste heat generation in steam power cycles. There is a certain number of studies on this subject in the literature. Chen et al. examined a hybrid photovoltaic / heat pump system [1]. In this study, waste heat of photovoltaic panel was utilized by using refrigerant R134a. It was observed that the performance coefficient (COP) of the system increased for high solar radiation and decreased for high flow rate. In addition, the electrical efficiency of the photovoltaic panel increased by 1.9%. Five different organic Rankine cycle (ORC) configurations, the use of photovoltaic thermal (PVT) systems for different fluid types and photovoltaic module materials have been investigated by Tourkov and Schafer [2]. As the working fluid, n-butane showed the highest performance and CdS was found to be the most compatible module mate-

rial with the configurations. Rahbar et al. combined the PVT system having different materials with a parabolic corrugated solar collector and used it as a heat source in an organic Rankine cycle [3]. R1233zd fluid was used for Rankine cycle and nano fluid (H_2O / Ag) was used for cooling of photovoltaic module. It was reported that the use of nanofluid increased the efficiency of the PVT system by 2.71%. In another study, CPVT system was used as the evaporator of an ORC [4]. R245fa was preferred as the heat transfer fluid and analyzes were performed for different solar radiation and photovoltaic module temperatures. System efficiency ranged from 9.81-11.83% depending on different parameter values. Han et al. performed thermodynamic analysis of the combination of CPVT system and concentrated solar power system [5]. In this study, it was revealed that increasing in the concentration ratio for PV module and decreasing in the exit temperature of the heat transfer fluid increased the energy and exergy efficiency. Qu et al. the use of the CPVT system with the Kalina cycle was investigated [6]. The CPVT system contributed to the LiBr-Water mixed absorption cooling system used in the cooling of the fluid exiting the turbine in the Kalina cycle. With this contribution, system efficiency increased between

2-3% and electrical module efficiency increased from 4.2% to 24% with cooling of photovoltaic module. In another study using the Kalina cycle and CPVT system, the effects of concentration ratio and module temperature on system efficiency were examined [7]. In the study, the electrical efficiency of photovoltaic module was found to be highest for 40 concentration ratio and 60 °C module temperature. Al-nimr et al. placed a photovoltaic module on the outer surface of the parabolic corrugated solar collector receiver and provided cooling of the module with the fluid in the receiver [8]. The electricity obtained from the photovoltaic module was used in hydrogen production. A thermodynamic analysis carried out for the integrated system consisting of Li-Br absorption cooling system, CPVT system and proton exchange membrane electrolyser by Akrami et al. [9]. In the study, electrical energy obtained from CPVT system was used for the production of hydrogen and the waste heat generated in the module was used for evaporation of water in the absorption cooling system. The exergy analysis revealed that the highest exergy loss was caused by the CPVT system.

In this study, unlike literature studies, CPVT system was used as preheater before evaporator in an ORC. By using the CPVT system as a pre-heater, it is aimed to increase the temperature of the heat transfer fluid before entering the evaporator, to reduce the heat load of the evaporator and to generate additional electrical energy through the photovoltaic module. The use of CPVT system as a preheater was investigated for different direct irradiation values, concentration ratios and photovoltaic module materials and energy and exergy efficiency calculations of ORC-CPVT system were performed.

MATERIAL AND METHODS

The use of the CPVT system as preheating in an ORC is shown in Fig. 1. In the ORC, the refrigerant R123 is used as the working fluid. In the system of Fig. 1, at the state 1, the fluid exits the condenser in the saturated liquid phase. In the state 2, the pressure of the fluid was increased to the evaporator pressure by the pump. The R123 fluid enters the CPVT system so that its temperature increases with the heat transfer from the solar energy and is separated from the photovoltaic module (State 3). In addition, as a result of solar radiation, electricity is produced from the photovoltaic module. The fluid becomes the superheated steam phase at the state 4. The fluid at the state 4 expands in the turbine and its pressure drops to the condenser pressure (State 5). The fluid at the state 5 becomes a saturated liquid in the state 1 by rejecting heat in the condenser and the pressure of the fluid is increased to the evaporator pressure by the pump and the cycle continues.

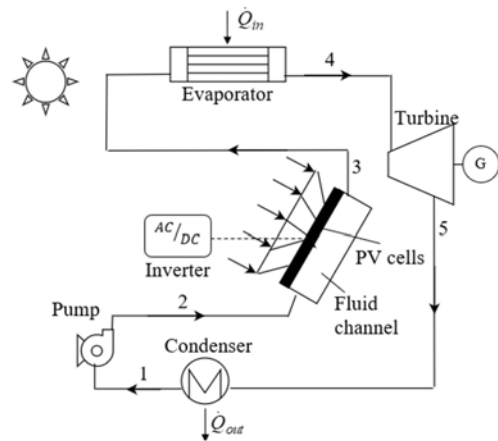


Figure 1. ORC with CPVT system

The energy and exergy calculations for the system in Fig. 1 were performed in accordance with some assumptions. All calculations were carried out for steady-state conditions. The pressure losses in the photovoltaic panel and piping line were neglected. In addition, isentropic efficiencies for pump and turbine were taken as 0.80 and 0.85, respectively [4].

The first and second laws of thermodynamics were used in the calculation of temperature, enthalpy, pressure, entropy and exergy values. The energy balance equations generated for each component given in Fig. 1 are shown in Table 1.

Table 1. Energy balance equations for each system component

| | |
|------------|--|
| Pump | $\dot{W}_p = [\dot{m}_{R123}(h_2 - h_1)]$ |
| Evaporator | $\dot{Q}_{in} = \dot{m}_{R123}(h_4 - h_3)$ |
| PV module | $\dot{Q}_{abs,R123} = \dot{m}_{R123}(h_3 - h_2)$ |
| Turbine | $\dot{W}_T = [\dot{m}_{R123}(h_4 - h_5)]$ |
| Condenser | $\dot{Q}_{out} = \dot{m}_{R123}(h_5 - h_1)$ |

CPVT system consists of photovoltaic module, ethylene vinyl acetate adhesives, glass cover, aluminum fluid channel and insulation (Fig. 2). The photovoltaic module converts solar rays directly into electrical energy and the temperature of the module increases during electricity generation. Some of the waste heat generated by the module is absorbed by the cold fluid and the other part is transferred to the external environment by conduction, convection and radiation heat transfer mechanisms.

The dimensions of the CPVT system and the thermal properties of the components are given in Table 2.

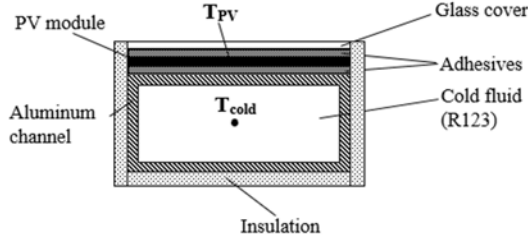


Figure 2. CPVT system structure

Table 2. CPVT system dimensions and thermal properties [6]

| Material | Thickness (m) | Width (m) | Thermal conductivity (W/m.K) | Emissivity |
|-----------|-----------------------|-----------|------------------------------|------------|
| Glass | 3×10^{-3} | 0.185 | 0.8 | 0.90 |
| PV cell | 3×10^{-4} | 0.165 | 14.8 | - |
| Adhesive | 1.27×10^{-6} | 0.185 | 0.37 | - |
| Aluminum | 4×10^{-3} | 0.185 | 211 | - |
| Glasswool | 3×10^{-2} | 0.245 | 0.005 | 0.50 |

The efficiency of the photovoltaic module (η) varies depending on the module temperature and the material of the module. The efficiency was calculated with Equation 1 given below [10],

$$\eta_{PV} = \eta_{ref} \left[1 - \beta_{ref} (T_{PV} - T_{ref}) + \gamma \log I \right] \quad (1)$$

Where, η_{ref} and β_{ref} indicates the module efficiency and the reference temperature coefficient at 25°C, respectively. T_{ref} is the reference temperature value (25°C) and I is the direct solar irradiation value. In Equation 1, the final expression in parentheses ($\gamma \log I$) can be neglected for low concentration values [10,11]. η_{ref} and β_{ref} vary according to the module material (Table 3). In actual conditions, the value β_{ref} varies slightly depending on the module temperature. However, according to the parameter values in the study, this value was considered constant since the module temperatures were close to each other [12].

Table 3. Constants for PV cell types

| Material | M-Si | P-Si | Ge | CdTe |
|---------------------|-----------------------|-----------------------|-----------------------|-----------------------|
| η_{ref} (%) | 25 | 19.5 | 7.8 | 17.3 |
| β_{ref} (1/K) | 9.03×10^{-4} | 9.03×10^{-4} | 4.76×10^{-3} | 9.26×10^{-3} |

Concentrated net solar radiation is calculated by Equation 2,

$$\dot{Q}_{PV} = ICA_{PV}\eta_{opt} \quad (2)$$

In the equation C concentration ratio, A_{PV} photovoltaic module aperture area and η_{opt} optical efficiency. Optical efficiency was taken as 0.83 [4].

The part of the solar radiation transformed into electrical energy ($\dot{W}_{elec,PV}$) is calculated by Equation 3,

$$\dot{W}_{elec,PV} = \dot{Q}_{PV}\eta_{PV}\eta_{inv} \quad (3)$$

Where, η_{PV} and η_{inv} are the PV module and inverter efficiency, respectively. The inverter efficiency was taken as 0.90 [4].

The waste heat generated by the electricity produced in the photovoltaic module is calculated by the following equation,

$$\dot{Q}_{waste} = \dot{Q}_{PV}(1 - \eta_{PV}) \quad (4)$$

While some of the waste heat is absorbed by the cold fluid in the fluid channel shown in Fig. 2, the other part is transferred from the system to the external environment as heat loss. The energy balance in these conditions can be expressed by Equation 5,

$$\dot{Q}_{waste} = \dot{Q}_{abs,cold} + \dot{Q}_{loss} \quad (5)$$

Where $\dot{Q}_{abs,cold}$ is the heat absorbed by the cold fluid and \dot{Q}_{loss} is the total heat loss to the external environment. $\dot{Q}_{abs,cold}$ and \dot{Q}_{loss} are calculated according to the thermal resistance network given in Fig. 3.

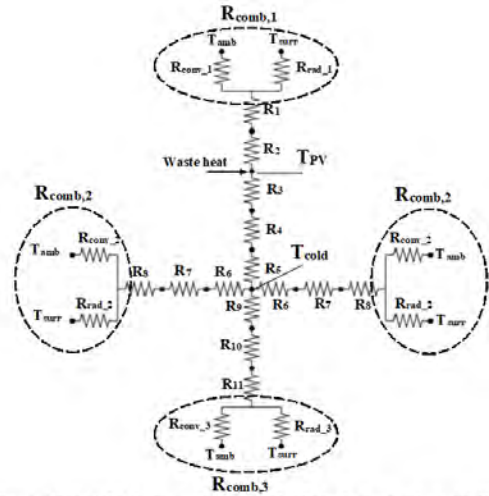


Figure 3. Thermal resistance network and heat transfer mechanisms

The highest temperature occurs in the photovoltaic module and some of the heat generated is transferred to the fluid and the other part is lost to the external environment. It was assumed that the temperature distribution in all la-

yers of the CPVT system was uniform. Considering the heat losses from the side surfaces of the fluid channel, heat losses from the glass surfaces, adhesives and the side surfaces of the photovoltaic module were ignored. The thermal resistances including the heat transfer mechanisms were calculated by Equation 6, 7 and 8.

$$R_{cond} = L_{thickness} / kA_{s,cond} \quad (6)$$

$$R_{conv} = 1 / hA_{s,conv} \quad (7)$$

$$R_{comb} = 1 / h_{comb} A_{s,comb} \quad T_{amb} \approx T_{surr} \quad (8)$$

In the equations, $L_{thickness}$ is the layer thickness, $A_{s,cond}$, $A_{s,conv}$ and $A_{s,comb}$ are conduction, convection and combined heat transfer surface areas, respectively. h and h_{comb} are respectively the fluid-related heat transfer coefficient and the combined heat transfer coefficient. Surrounding and ambient temperatures were taken approximately equal in terms of creating convenience in calculations [13]. The combined heat transfer coefficient including the convection and radiation effects was found by Equation 9.

$$h_{comb} = h_{conv} + h_{rad} \quad (9)$$

Here, h_{conv} and h_{rad} denote heat transfer coefficients of convection and radiation, respectively. These heat transfer coefficients were calculated by Equation 10 and 11,

$$h_{conv} = 2.8 + 3V_{wind} \quad (10)$$

$$h_{rad} = \sigma \epsilon (T_s^2 + T_{surr}^2) (T_s + T_{surr}) \quad (11)$$

Where, σ Stefan Boltzmann constant, ϵ is the emissivity and T_s surface temperature. The wind velocity was taken as 1 m / s.

The Nu number equation was used to calculate the heat transfer coefficient in the fluid region. The equation used to find the Nu number in a rectangular channel flow is given by Equation 12 [6],

$$Nu = \begin{cases} 3.66 + \frac{(0.49 + 0.02 / Pr) \left(\frac{Re Pr D_h}{L} \right)^{1.12}}{\left(1 + 0.065 \left(\frac{Re Pr D_h}{L} \right)^{0.7} \right)} & Re < 2300 \\ \frac{\left(\frac{f}{8} \right) Re Pr}{K_1(f) + K_2(Pr) \left(\frac{f}{8} \right)^{\frac{1}{2}} \left(Pr^{\frac{2}{3}} - 1 \right)} & Re \geq 2300 \end{cases} \quad (12)$$

K_1 and K_2 functions are calculated with the following equations, depending on the coefficient of friction (f) and Prandtl number (Pr),

$$K_1(f) = 1 + 3.4f \quad (13)$$

$$K_2(Pr) = 11.7 + 1.8Pr^{-\frac{1}{3}} \quad (14)$$

$$f = (1.82 \log Re - 1.64)^{-2} \quad (15)$$

Reynolds (Re) and Pr numbers are calculated by Equation 16 and 17,

$$Re = \rho V D_h / \mu \quad (16)$$

$$Pr = \mu c_p / k_{fluid} \quad (17)$$

All thermophysical properties of the fluid were determined according to the average fluid temperature. The heat transfer coefficient in the fluid channel was calculated with the following equation depending on the Nu number,

$$h = k_{fluid} Nu / D_h \quad (18)$$

Heat transfer values absorbed by the fluid and lost to the external environment were calculated by Equation 19 and 20, respectively.

$$\dot{Q}_{abs,R123} = \frac{T_{PV} - T_{cold}}{R_3 + R_4 + R_5} \quad (19)$$

$$\dot{Q}_{loss} = \frac{T_{PV} - T_{surr}}{R_1 + R_2 + R_{comb,1}} + 2 \left(\frac{T_{cold} - T_{surr}}{R_6 + R_7 + R_8 + R_{comb,2}} \right) + \left(\frac{T_{cold} - T_{surr}}{R_9 + R_{10} + R_{11} + R_{comb,3}} \right) \quad (20)$$

In the first stage of the analysis, the average fluid temperature (T_{cold}) was estimated according to the inlet temperature of the fluid. The estimated and calculated average fluid temperatures were then compared with each other. Iterations continued until the difference between the estimated and calculated mean fluid temperatures was less than 0.1°C.

Thermal efficiency of the system (η_{th}) is calculated with the equation given below,

$$\eta_{th} = \frac{\dot{W}_{net}}{\dot{Q}_{sol,CPVT} + \dot{Q}_{in}} \quad (21)$$

Where, " \dot{W}_{net} " is the net power obtained from the system, " $\dot{Q}_{sol,CPVT}$ " is the solar energy coming into the CPVT system and " \dot{Q}_{in} " is the heat input in the evaporator. These energy and heat transfer values are calculated by the following equations,

$$\dot{W}_{net} = \dot{W}_T + \dot{W}_{elec,PV} - \dot{W}_{pump} \quad (22)$$

$$\dot{Q}_{sol,CPVT} = ICA_{PV} \quad (23)$$

In the equations \dot{W}_T refers to the electrical energy obtained from the turbine, $\dot{W}_{elec,PV}$ refers to the electrical energy obtained from the CPVT system, and \dot{W}_{pump} refers to the energy input to the pump used in the ORC.

Exergy efficiency of the system (η_{ex}) was found by using Equation 24,

$$\eta_{ex} = \frac{\dot{W}_{net}}{\dot{E}_{sol,CPVT} + \dot{E}_{Q_{in}}} \quad (24)$$

The exergies of solar energy and heat input were calculated by Equation 25 [14] and Equation 26,

$$\dot{E}_{sol,CPVT} = IA_{PV}C \left(1 - \frac{4T_{amb}}{3T_{sol}} + \frac{1}{3} \left(\frac{T_{amb}}{T_{sol}} \right)^4 \right) \quad (25)$$

$$\dot{E}_{Q_{in}} = \dot{Q}_{in} \left[1 - \left(\frac{T_{amb}}{T_{source}} \right) \right] \quad (26)$$

T_{sol} is the surface temperature of the sun (6000 K) and T_{source} is the temperature of the heat source (473 K). Ambient temperatures due to solar radiation were taken from an existing study in the literature [15].

Thermodynamic analysis of the CPVT system and ORC was performed using the EES commercial package program. The CPVT system and ORC simulation results were compared with the literature studies. Fig. 4 shows the comparison of the analysis results of the CPVT system for the water inlet temperature at 60 °C with the results of the literature in terms of average water and PV module temperature. The highest difference between analysis and literature results for the average water temperature and the PV module temperature were observed as 1.5% and 0.56%, respectively.

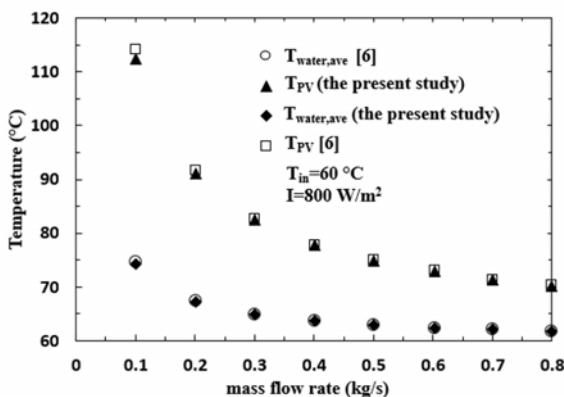


Figure 4. Validation of CPVT simulation

Validation for ORC simulation is given in Table 4. For enthalpy and entropy values, the highest deviation was 0.4% and 0.36%, respectively.

Table 4. Validation of ORC simulation with Ref. [4]

| State | Temperature (°C) | Pressure (bar) | Enthalpy (kJ/kg) | | Entropy (kJ/kg.K) | |
|-------|------------------|----------------|------------------|--------|-------------------|--------|
| | | | Analysis | Ref. | Analysis | Ref. |
| 1 | 30 | 1.7904 | 239.1 | 239.6 | 1.135 | 1.1372 |
| 2 | 30.4 | 10.044 | 239.9 | 240.35 | 1.136 | 1.1377 |
| 4 | 90 | 10.044 | 468.2 | 470.48 | 1.7925 | 1.786 |
| 5 | 49 | 1.7904 | 444.8 | 445.01 | 1.812 | 1.8137 |

When the validation results are examined, it is seen that the analysis results are consistent with the results of the studies in the literature.

RESULTS AND DISCUSSION

In this study, the use of CPVT system as a preheater in the ORC was evaluated in terms of system efficiency and exergy. Thermodynamic analyzes were performed for different solar irradiation values, concentration ratio values and various photovoltaic module materials.

Table 4 shows the thermodynamic properties obtained at each state in the cycle for certain parameter values. The use of the CPVT system increased the temperature of the R123 fluid prior to entering the evaporator (State 3). Depending on the change in parameter values, the increase in temperature at state 3 also changed. When the CPVT system was not used, the fluid temperature was increased from 48.86 °C to 182 °C with the heat input in the evaporator. In the case of CPVT usage, the R123 temperature in the evaporator was increased from 91.22 °C to 182 °C. Thus, the heat input to the system decreased.

Table 5. Thermodynamic properties for specific parameter values ($C = 10$, $I = 964 \text{ W/m}^2$, $M\text{-Si}$, $A_{pv} = 4.95 \text{ m}^2$)

| State | \dot{m} (kg/s) | T (°C) | P (kPa) | h (kJ/kg) | s (kJ/kg.K) |
|-------|------------------|----------|-----------|-------------|---------------|
| 1 | 0.5 | 48.01 | 200 | 250.4 | 1.169 |
| 2 | 0.5 | 48.86 | 1800 | 251.8 | 1.17 |
| 3 | 0.5 | 91.22 | 1800 | 298.5 | 1.305 |
| 4 | 0.5 | 182 | 1800 | 509.4 | 1.816 |
| 5 | 0.5 | 124.4 | 200 | 124.4 | 1.84 |

Fig. 5 shows the changes in system efficiency and electricity generation as a result of different parameter changes. In Fig. 5a, efficiency and power values due to solar radiation are given. The increase in solar radiation increased the electricity production in the PV module. As a result, the

temperature of the fluid at the evaporator inlet was increased, thus the heat input required was decreased for the system. Preheating and the generation of electricity increased the thermal efficiency of the system from 12.1% to 15.5%. The condition where the radiation is zero indicates that the CPVT system is not used. On the other hand, with the use of CPVT system, it was observed that the exergy efficiency of the system decreased from 33.6% to 28.8%. This is due to the fact that the exergy of solar energy is higher than the increase in the work output obtained from the system. Since the temperature values at the state 4 and 5 were same for the both conditions, the amount of energy obtained from the turbine was constant. As can be seen from Fig. 5b, the increase in the concentration ratio increased the electrical energy obtained from the CPVT system and the temperature value at the state 3 so that the thermal efficiency ranged between 12.4-15.5%. Similar to Fig. 5a, with the increase of solar energy input, the exergy efficiency decreased from 32.6% to 28.8%. Fig. 5c shows the effects of PV module material on energy production and system efficiency. In terms of electricity generation and system efficiency, P-Si and M-Si PV module materials were found to be more convenient. This is due to the high electrical efficiency of P-Si and M-Si module materials. CdTe and Ge module materials also contributed to the generation of electricity, but the module temperatures were higher due to low electrical efficiency. The high module temperature transferred more heat energy to the fluid but decreased the electricity production and caused the thermal and exergy efficiency of the system to decrease compared to other PV materials.

CONCLUSION

When the CPVT system was used as a preheater in an ORC, the fluid temperature was increased before the evaporator and additional electricity was generated. As the heating of the fluid before the evaporator reduced the heat input to the evaporator, the thermal efficiency of the system increased. On the other hand, the use of the CPVT system has led to a decrease in the exergy efficiency as the exergy of the solar energy is higher than the increase in the work output obtained from the system.

The change of parameter values affected the amount of energy obtained and system efficiency. The increase in solar radiation and concentration ratio increased the electricity production of the PV module and thermal efficiency of the system and led to a decrease in exergy efficiency. The CPVT system was also examined for the effect of PV module material. It was observed that M-Si and P-Si module materials were more convenient in terms of system efficiency and electricity generation.

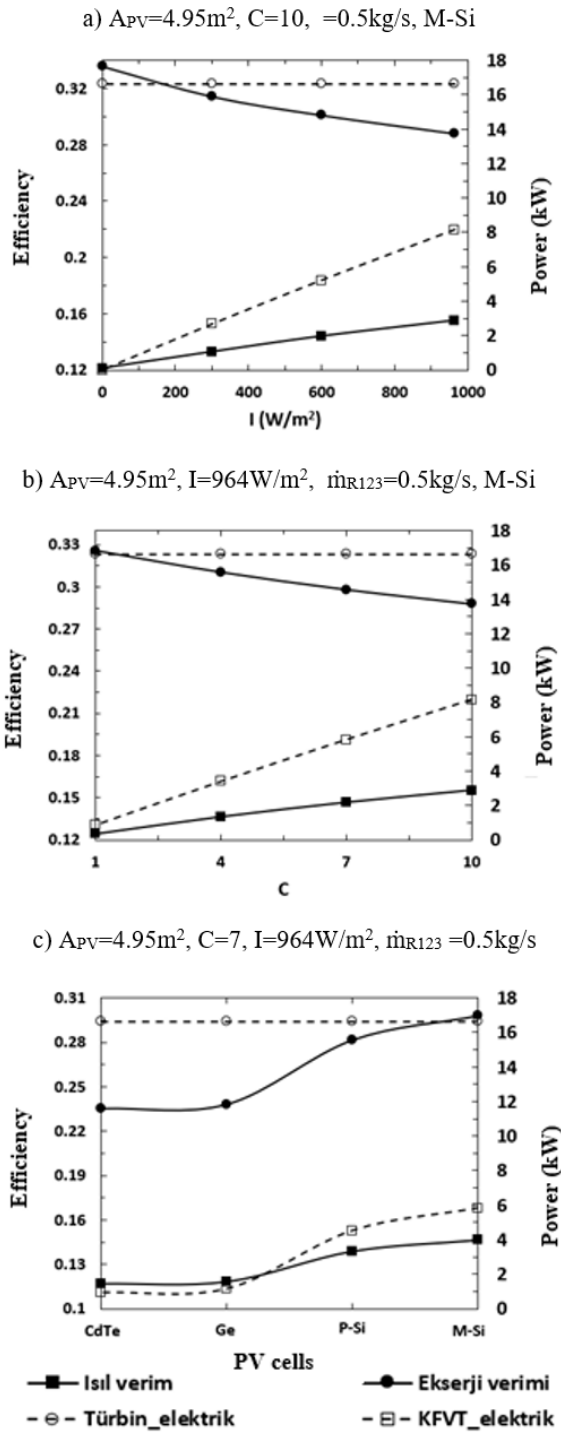


Figure 5. System efficiencies and power generations

As can be seen from the results of the analysis, the use of CPVT system as a preheater for suitable PV cell material significantly increased power production and thermal efficiency of the system.

References

1. Chen, Hongbing, Saffa B. Riffat, and Yu Fu. "Experimental study on a hybrid photovoltaic/heat pump system." *Applied Thermal Engineering* 31.17–18 (2011) 4132–4138.
2. Tourkov, Konstantin, and Laura Schaefer. "Performance evaluation of a PVT/ORC (photovoltaic thermal/organic Rankine cycle) system with optimization of the ORC and evaluation of several PV (photovoltaic) materials." *Energy* 82 (2015) 839–849.
3. Rahbar, Kiyarash, et al. "Heat recovery of nano–fluid based concentrating Photovoltaic Thermal (CPV/T) Collector with Organic Rankine Cycle." *Energy conversion and management* 179 (2019) 373–396.
4. Kosmadakis, G., D. Manolakos, and G. Papadakis. "Simulation and economic analysis of a CPV/thermal system coupled with an organic Rankine cycle for increased power generation." *Solar Energy* 85.2 (2011) 308–324.
5. Han, Xue, et al. "Parametric analysis of a hybrid solar concentrating photovoltaic/concentrating solar power (CPV/CSP) system." *Applied energy* 189 (2017) 520–533.
6. Qu, Wanjun, et al. "A concentrating photovoltaic/Kalina cycle coupled with absorption chiller." *Applied energy* 224 (2018) 481–493.
7. Qu, Wanjun, Bosheng Su, and Sanli Tang. "Thermodynamic Evaluation of a hybrid solar concentrating photovoltaic/Kalina cycle for full spectrum utilization." *Energy Procedia* 142 (2017) 597–602.
8. Moh'd A, Al-Nimr, Mohammad Bukhari, and Mansour Mansour. "A combined CPV/T and ORC solar power generation system integrated with geothermal cooling and electrolyser/fuel cell storage unit." *Energy* 133 (2017) 513–524.
9. Akrami, Ehsan, et al. "Exergy and exergoeconomic assessment of hydrogen and cooling production from concentrated PVT equipped with PEM electrolyzer and LiBr-H₂O absorption chiller." *International Journal of Hydrogen Energy* 43.2 (2018) 622–633.
10. Skoplaki, Elisa, and John A. Palyvos. "On the temperature dependence of photovoltaic module electrical performance: A review of efficiency/power correlations." *Solar energy* 83.5 (2009) 614–624.
11. Notton, Gilles, et al. "Modelling of a double-glass photovoltaic module using finite differences." *Applied thermal engineering* 25.17–18 (2005) 2854–2877.
12. Kribus, Abraham, et al. "A miniature concentrating photovoltaic and thermal system." *Energy Conversion and Management* 47.20 (2006) 3582–3590.
13. Cengel, Yunus. *Heat and mass transfer: fundamentals and applications*. McGraw–Hill Higher Education, 2014.
14. Petela, Richard. "Exergy of undiluted thermal radiation." *Solar Energy* 74.6 (2003) 469–488.
15. Jafarkazemi, Farzad, and Emad Ahmadifard. "Energetic and exergetic evaluation of flat plate solar collectors." *Renewable Energy* 56 (2013) 55–63.

Solar Power Prediction with an Hour-based Ensemble Machine Learning Method

Seyda Ertekin 

Middle East Technical University, Department of Computer Engineering, Ankara, Turkey

ABSTRACT

In recent years, the share of solar power in total energy production has gained a rapid increase. Therefore, prediction of solar power production has become increasingly important for energy regulations. In this study we proposed an ensemble method which gives competitive prediction performance for solar power production. This method firstly decomposes the nonlinear power production data into components with a multi-scale decomposition technique such as Empirical Mode Decomposition (EMD). These components are then enriched with the explanatory exogenous feature set. Finally, each component is separately modeled by nonlinear machine learning methods and their results are aggregated as final prediction. We use two different training approaches such as Hour-based and Day-based, for predicting the power production at each hour in a day. Experimental results show that our ensemble method with Hour-based approach outperform the examined machine learning methods.

Keywords:

Solar power, Time series forecasting, Machine learning, Ensemble methods, Empirical mode decomposition

Article History:

Received: 2019/11/23

Accepted: 2020/03/17

Online: 2020/03/26

Correspondence to: Seyda Ertekin,
Department of Computer Engineering,
Middle East Technical University,
06680, Ankara, Turkey
E-mail: serteekin@metu.edu.tr,
Phone: +90 312 210 5509,
Fax: +90 312 210 5544.

INTRODUCTION

Energy sustainability is crucial for economic growth and financial development. Therefore, supplying energy through sustainable resources plays an important role in national economic strategies. It is well known that renewable energy sources such as solar power are sustainable in long-term timeline as compared to fossil resource [1]. With the developing technology, the cost of solar panels such as Photo-Voltaic, which directly produce electricity from solar energy, is decreasing. Thus, in developing countries such as Turkey, solar energy production comes to the increasingly important level.

The total installed capacity of solar power plants in Turkey increased by 57% over the last two years and has reached to 5 GW [2]. With the planned capacity increase, the installed capacity is expected to exceed 30 GW in the next 10 years [3]. In short, the share of total production of solar energy production in Turkey is increasing rapidly. Therefore, forecasting solar power production for making decision in power system scheduling and grid regulation plays an important role in Turkey's electric industry.

Solar power forecasting models are categorized according to model designs and inputs used by models. The Numerical Weather Forecast (NWP) model has been widely applied for solar radiation estimation [4,5]. This approach uses mathematical models of weather conditions for prediction. This method is often used for short-term (such as 6-hour) forecasts and model performance varies depending on weather data such as cloud cover and temperature [6,7].

Time series models aim to predict future data from past observed data using statistical and machine learning techniques. In literature, there are various time series methods [8, 9, 10, 11], some of them are directed towards for forecasting solar power [12, 13, 14, 15, 16, 17, 18]. Solar time series data includes high volatility and nonlinearity. Thus, nonlinear time series prediction methods are more preferable to achieve high prediction accuracies in solar power forecasting [8, 10, 14]. Nonlinear methods, such as Artificial Neural Networks (ANNs), Gradient Boosting Machines (GBM), Support Vector Regressor (SVR) can arbitrarily fit complex non-stationary functions with high accuracy.

Multi-scale decomposition techniques are also used together with prediction methods to increase prediction performance. Empirical Mode Decomposition (EMD) is one of the most widely used decomposition technique in different time series problems [9, 19, 20]. EMD is able to decompose any nonlinear and nonstationary data into components [21]. Since these components are highly correlated in themselves, more accurate forecasting results can be achieved. Solar power data usually shows nonlinear and non-stationary properties and has different volatility and fluctuations in different time periods. In order to achieve high accuracy results in solar power forecasting, several methods using EMD are proposed [22, 23, 24].

In this study, Turkey's solar power production is predicted with an ensemble method using EMD which does not only use historical data, but also enriched explanatory feature set which yields better approximations to more accurate predictions. In this ensemble method, the predictions are performed for each EMD components separately and their results are aggregated as final prediction result. Solar energy production is directly proportional with the amount of time that the solar power panels are exposed to the sun. Therefore, during the summer season at noon hours, the highest production figures appear. In order to capture these seasonal variations, the developed ensemble method uses chronological features such as month and quarter. In addition, the angle of the sun and irradiance at ground level play an important role in energy production. Therefore, the developed ensemble method takes various irradiation-related features into account.

The developed method is tested with ANN, SVR, GBM methods in the prediction stage. We performed day-ahead prediction where we predict next day (24-hours) production for every hour. We followed two approaches: Hour-based and Day-based. In Hour-based approach, each hour prediction in a day is performed separately by training the model with the corresponding hours in the historical data. On the other hand, in Day-based approach, each hour prediction in a day is performed by training the model with the entire historical data. We showed that Hour-based approach is more advantageous in solar power predictions, since it captures the high correlation between the production and solar irradiance.

METHODS

The developed method includes three main parts: Multiscale decomposition, feature enrichment and modeling. The architecture of the method is shown in Fig. 1.

Multiscale Decomposition

Solar power data shows nonlinear and non-stationary properties and has different volatility and fluctuations in different time periods. Using multiscale decomposition techniques are efficient and effective method to analyze this nonlinearities in these time series [25]. In literature, there are several multiscale decomposition techniques such as Empirical Mode Decomposition (EMD), Wavelet Packet Decomposition (WPD), Fourier Transform (FT) and etc. [26]. EMD is able to preserve time scale of the given time series throughout the decomposition, thus it is a more preferable technique than the others [21].

The essence of the EMD technique is to empirically identify the intrinsic oscillatory modes in the data and then decompose the data accordingly. The decomposed components, are called Intrinsic Mode Function (IMF) and have two important properties:

1. Each IMF has its own local characteristic time scale.
2. IMFs are relatively stationary series.

These properties allow to resolve nonlinearity and nonstationarity in solar power data. Thanks to this, forecasting methods are able to produce more accurate results.

Let $y(t)$ be a solar power data and EMD technique can be described as follows:

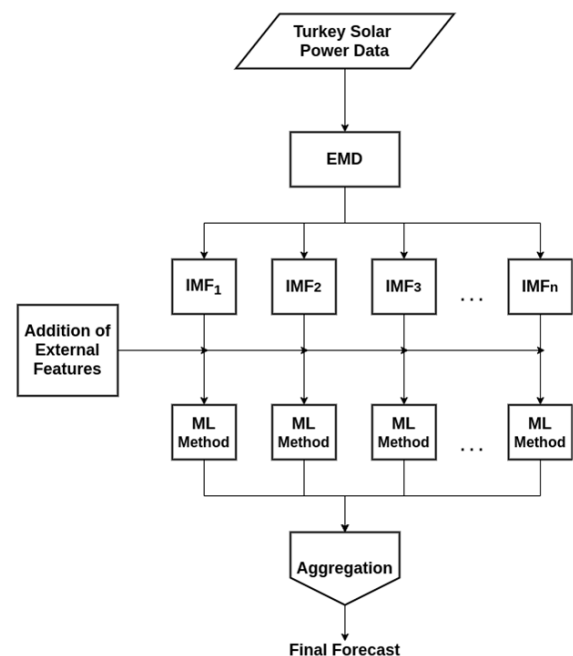


Figure 1. The architecture of proposed ensemble method

$$y(t) = \sum_{k=1}^m imf(t)_k + r(t)_m \quad (1)$$

where $imf(t)$ represents the intrinsic mode functions, and $r(t)$ is the residue. The detailed EMD procedure is as follows [27]:

1. All local extrema maxima and minima points of time series $y(t)$ are identified.

2. Upper and lower envelopes are constructed for identified extrema points by using cubic spline interpolation.

3. Mean value $m(t)$ of the envelopes are computed.

4. Take difference of mean and given series and obtain the first components: $h(t)=y(t)-m(t)$

5. Check properties of being IMF for $h(t)$:

a. If $h(t)$ meets two above conditions, it is considered as an IMF and it is denoted as $imf(t)$ in Equation 1. Then, let residual $r(t)=y(t)-h(t)$ and replace $y(t)$ with the residual $r(t)$ return step 1.

b. If $h(t)$ does not satisfy the conditions, let $y(t)=r(t)$ and return step 1.

6. Steps 1-5 are repeated until the obtained residual $r(t)$ is a monotonic function.

Feature Enrichment

The production of solar energy highly depends on various factors such as the presence of the sun, the angle of the sun and irradiance [1, 28]. Therefore, rather than using only historical data, those features can also be included into the feature set to increase forecasting accuracies. These features can be divided into two groups: Chronological and irradiance-related features.

Seasonal variations of solar energy production can be captured with chronological features. For this purpose, month and quarter knowledge is extracted from the time information and added into the feature set.

The monthly distribution of solar energy production is given in Fig. 2. Production values reaches the highest levels in August, but it is very low in December due to insufficient sunny days.

The quarterly distribution of solar energy production is given in Fig 3. It is evident that the production in the fourth quarter of the year, which includes sunless months, is considerably less than that of the third quarter of the year, which includes sunny months.

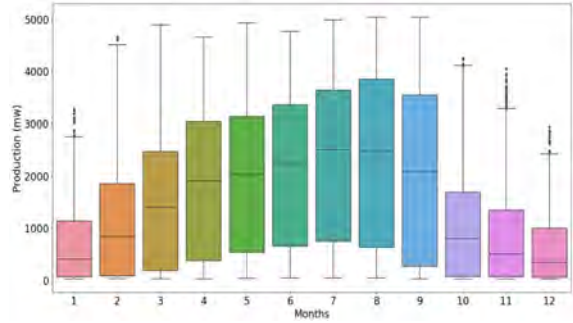


Figure 2. Monthly distribution of the solar power production of Turkey between Sep.2017-Sep.2019

Extraterrestrial, solar-oriented beam irradiance events occurring in the Earth's atmosphere are examined in three different components [1]: Direct Normal Irradiance (DNI), Diffuse Horizontal Irradiance (DHI) and Global Horizontal Irradiance (GHI).

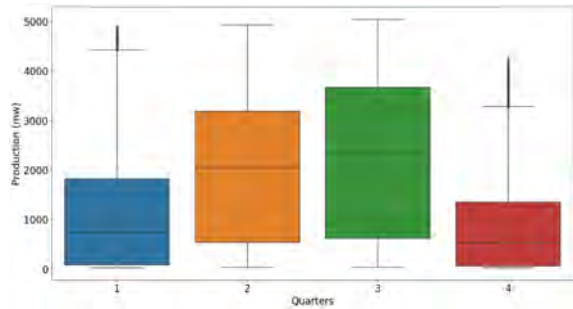


Figure 3. Quarterly distribution of the solar power production of Turkey between Sep.2017-Sep.2019

DNI is the amount of solar radiation that is perpendicular to the Sun, received per unit area at a given location. This measurement is particularly important to solar thermal installations that track the position of the sun. DFI is the amount of solar radiation at the Earth's surface from light scattered by the atmosphere and comes equally from all directions. Unlike DNI, DFI does not take radiation coming directly from the sun into account. GHI is the total amount of irradiance from the sun on Earth. This value is the sum of direct irradiance (DNI) and diffuse irradiance (DHI) which can be shown as follows:

$$GHI = DHI + DNI * \cos q \quad (2)$$

where q is the solar zenith angle. Since GHI indicates the summation of DNI and DFI, solar power plants particularly follow this amount.

These irradiance values, which explain the angle of the sun and quantity of the sun, are important explanatory features for solar energy production. Therefore, these are also added to the attribute set of the developed ensemble method.

Modelling

The solar energy production data $y(t)$ is decomposed into n number of components ($imf_1, imf_2, imf_3, \dots, imf_n$) by EMD, and each component is modelled with a number of the observed the data ($imf(t-1), imf(t-2), \dots, imf(t-a)$) and enriched feature set ($f_{chronological}, f_{irradiance}$) by machine learning models, as shown in the following equation:

$$y(t+1) = g(imf(t-1), imf(t-2), \dots, imf(t-a), f_{ch}, f_{irr}) \quad (3)$$

where g is the machine learning models such as ANN, GBM, SVR methods that we used in this study. Finally, forecasts from each component are summed up.

We propose to model the developed method, which aims to produce day ahead forecast, with an Hour-based approach. In this approach, each hour is trained and modelled in itself. This is because production within each hour is highly correlated in itself. Thus, models trained in data with less variance show higher predictive performance. Fig.4 shows the hourly distribution of solar energy production. While solar power production in the morning and evening hours is low, it increases in noon hours.

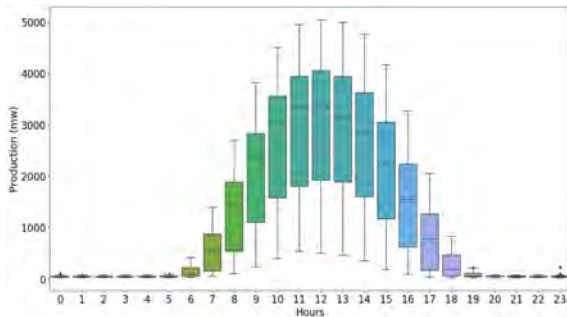


Figure 4. Hourly distribution of the solar power production of Turkey between Sep.2017-Sep.2019

RESULTS AND DISCUSSION

For Turkey solar power forecasting, hourly production data of last two years is used which is shown in Fig.5. This data is publicly available [29]. This hourly dataset consists of 17520 solar production values in Megawatt from Sep. 2017 to Sep. 2019. In this dataset, the solar production values vary between 0 and 5039 Megawatt (MW), while the average hourly production value is 979 MW.

In the experiments, 3 different machine learning algorithms, ANN, GBM, and SVR, are adopted into the developed ensemble method. In the modelling phase, the solar power dataset is split into three sets such as train, validation and test. 25% of the train set is used as the validation set to adjust the hyperparameters of the methods. The last 90 days

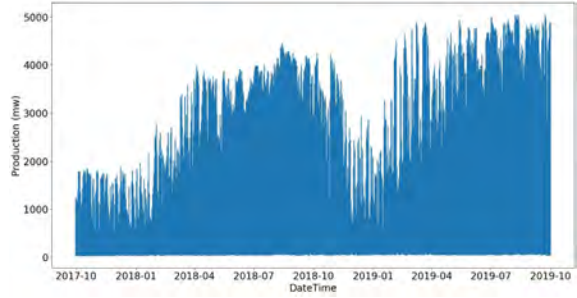


Figure 5. Hourly distribution of the solar power production of Turkey between Sep.2017-Sep.2019

of this time series, which has hourly 720 days of solar power production data, is used as a test set. The last 158 days of the remaining 630 days are the validation set, while 472 days are the training set. The test set used to present the performance of the methods is the last three months of the dataset. We apply grid search to tune the hyperparameters. We provided the search space of each algorithm in Table 1 and we indicated the ones that give the best results in bold. We used those best hyperparameters in order to report our error results in Table 2.

Table 1. The hyper-parameters of the applied machine learning methods

| | Parameter search spaces |
|-----|---|
| GBM | $learning_rate : [0.01, 0.05, 0.10, 0.20]$ |
| | $max_depth : [2, 3, 4, 5]$ |
| | $n_estimator : [300, 900, 3900, 4900]$ |
| SVR | $kernel = [linear, poly, rbf]$ |
| | $C = [0.1, 0.5, 1, 10]$ |
| | $epsilon = 0.1$ |
| ANN | $activation : [ReLU, Sigmoid, Tanh]$ |
| | $optimizer : [Adam, Nadam, Sgd]$ |
| | $architecture = (n \times 2n \times 1)$ |

In order to show the effectiveness of Hour-based approach, the same experimental setup is implemented for Day-based approach. While comparing performance results between methods, two error metrics are used: Normalized Mean Absolute Error (NMAE) and Normalized Mean Squared Error (NMSE) which are formulated as follows:

$$NMAE = \left(\frac{1}{n} \sum |e(t)| \right) / N \quad (4)$$

$$NMSE = \left(\frac{1}{n} \sum e(t)^2 \right) / N$$

where $e(t) = y(t) - y^{\wedge}(t)$ and $y(t)$ is the actual data value, $y^{\wedge}(t)$ is the forecasted value at given time t . N is the installed solar power capacity. NMAE measures the normalized average of the absolute errors over a given prediction whereas NMSE specifies the normalized average of the squared error.

The experiment results are shown in Table 2. The machine learning methods used in the proposed ensemble architecture are additionally executed individually and their results are also compared in terms of both error metrics. Furthermore, all these experiments are performed for both Day-based and Hour-based approaches, as seen in Table 2.

Table 2. Experimental Results (All NMAE results are multiplied by 100.)

| Approach | Method | NMAE | NMSE |
|------------|----------------|------|-------|
| Day-based | GBM | 2.80 | 14.93 |
| | SVR | 3.12 | 16.89 |
| | ANN | 2.72 | 13.00 |
| | Ensemble – GBM | 2.63 | 12.02 |
| | Ensemble – SVR | 2.97 | 14.67 |
| | Ensemble – ANN | 2.71 | 12.88 |
| Hour-based | GBM | 2.55 | 11.41 |
| | SVR | 3.01 | 15.91 |
| | ANN | 2.64 | 11.83 |
| | Ensemble – GBM | 1.96 | 8.07 |
| | Ensemble – SVR | 2.13 | 10.98 |
| | Ensemble – ANN | 2.01 | 8.91 |

When individual execution of machine learning methods are compared, it is seen that GBM and ANN give better results than SVR. For example, in the Hour-based approach, ANN and GBM give 2.55 and 2.64 NAME error results, respectively, while NAME result of SVR is slightly more than 3. As a result, ANN and GBM are able to yield better generalization in this nonlinear dataset. When the GBM and ANN results are compared in themselves, ANN has better results in individual use in execution, whereas GBM is able to have more accurate results in the proposed ensemble approach.

When the results of the proposed ensemble methods are examined, it is clear that it has improved the results of the individually executed machine learning methods. In both Hour-based and Day-based approaches, ensemble methods are able to produce more accurate results for both error metrics. For example, in the Hour-based approach, GBM, SVR and ANN machine learning methods are improved by the proposed ensemble method by 23%, 28%, and 24%, respectively. This indicates that when machine learning methods are fed with decomposed time series data with descriptive exogenous features, the movement in data can be captured more effectively.

When Day-based and Hour-based approaches are compared, it is clear that the Hour-based approach gives more accurate results than the Day-based approach. As shown in Fig. 4, solar power production values have different distributions within each hour. Hour-based approach, which reduces the variance of these different distributions, outperforms Day-based results between 4% and 25%.

CONCLUSION

Solar power production forecasting plays an important role in Turkey's electricity industry for making decisions in power system scheduling and grid regulation. In this study, we developed an ensemble method which can work with different machine learning algorithms on EMD components of the time series data with explanatory exogenous features. We use this method to forecast solar power production of Turkey. This method firstly decomposes the solar power data into the components by the EMD decomposition technique. These components are then enriched with explanatory exogenous features. Each of these components are modeled separately by machine learning methods and their results are aggregated to obtain final prediction result. We trained our ensemble method with two different approaches, Day-based and Hour-based. We performed the experiments on the last two years of solar energy production data of Turkey. Our experiments show that when (i) the time series data is decomposed before feeding into the machine learning algorithms, (ii) explanatory exogenous features are used in addition to historical data, (iii) each hour in a day is predicted with the model trained with the corresponding hours in the historical data. As a result, the developed ensemble method has a high potential in prediction of solar power production in energy industry.

References

- Inman RH, Hugo TC, Carlos FM. Solar forecasting methods for renewable energy integration. Volume 39, Issue 6, December 2013, Pages 535–576, doi:10.1016/j.pecs.2013.06.002.
- Enerji Atlasi, 2019, Gunes Enerji Santralleri, retrieved September 12, 2019, from: <https://www.enerjiatlasi.com/gunes/>
- GUYAD, 2019, retrieved October 22, 2019, from: <http://www.guyad.org/TR,360/teias-10-yillik-kapasite-planlamasini-yayinladi.html>
- Heinemann D, Lorenz E, Girodo M. Forecasting of solar radiation in: solar energy resource management for electricity generation from local level to global scale. Nova Sciences Publishers; 2006.
- Perez R, Beauharnois M, Lorenz E, Pelland S, Schlemmer J. Evaluation of Numerical Weather Prediction Solar Irradiance Forecasts in the US Proc. ASES Annual Conference. Raleigh, NC, USA–1721, May; 2011.
- Marquez R, Carlos FM. Intra-hour dni forecast based on cloud tracking image analysis. Solar Energy, 91, 327–336, May 2013, doi.org/10.1016/j.solener.2012.09.018.
- Bosh J, Zheng Y, Kleissl J. Deriving cloud velocity from a area of solar radiation measurements. Solar Energy, 87, 196–203, Jan. 2013, doi.org/10.1016/j.solener.2012.10.020.

8. Zhang P. Time Series Forecasting Using a Hybrid ARIMA and NeuralNetwork Model. *Neurocomputing* 50, 159–175, Neurocomputing, 50, 159-175, 2002, doi:10.1016/S0925-2312(01)00702-0.
9. Buyuksahin UC, Ertekin S. Improving forecasting accuracy of time series data using a new ARIMA-ANN hybrid method and empirical mode decomposition, *Neurocomputing* 361, 151-163, 2019, doi.org/10.1016/j.neucom.2019.05.099.
10. Khashei M, Bijari M. A Novel Hybridization of Artificial Neural Networks and ARIMA Models for Time Series Forecasting. *Appl. Soft Comput.*, 11, 2664-2675, 2011, doi:10.1016/j.asoc.2010.10.015.
11. Buyuksahin UC, Ertekin S. A feature-based hybrid ARIMA-ANN model for univariate time series forecasting. *Journal of the Faculty of Engineering and Architecture of Gazi University* 35:1 (2020) 467-478 doi.org/10.17341/gazimfd.508394.
12. Huang J, Korolkiewicz M, Agrawal M, Boland J. Forecasting solar radiation on an hourly time scale using a coupled autoregressive and dynamical system (cards) model. *Solar Energy*; 87, 136-149, Jan. 2013, doi.org/10.1016/j.solener.2012.10.012.
13. Glasbey CA, Allcroft DJ. A spatiotemporal auto-regressive moving average model for solar radiation. *Appl Stat*, 57, 343-355, 2007.
14. Mellit, A. Artificial Intelligence Technique for Modelling and Forecasting of Solar Radiation Data: A Review. *Int. J. Artif. Intell. Soft Comput.*, 1, 52-76, 2008.
15. Martin L, Zarzalejo LF, Polo J, Navarro A, Marchante, R, and Cony M. Prediction of Global Solar Irradiance Based on Time Series Analysis: Application to Solar Thermal Power Plants Energy Production. *Solar Energy*, 84, 1772-1781, Oct. 2010, doi.org/10.1016/j.solener.2010.07.002.
16. Mohamed A, Chowdhury C. Solar Power Forecasting Using Artificial Neural Networks. In 2015 North American Power Symposium (NAPS), 1-5, 2015.
17. Hamid E, Himdi K. Artificial Neural Network for Forecasting One Day Ahead of Global Solar Irradiance. SSRN Scholarly Paper. Rochester, NY: Social Science Research Network, May 29, 2018.
18. Daniel O, Kubby J. Feature Selection and ANN Solar Power Prediction. *Research Article. Journal of Renewable Energy*, 2017. <https://doi.org/10.1155/2017/2437387>.
19. Xu X, Qi Y, Hua Z. Forecasting demand of commodities after natural Disasters. *Expert Systems with Applications*, Volume 37, Issue 6, June 2010, Pages 4313-4317, doi.org/10.1016/j.eswa.2009.11.069.
20. Yu W, Mu-Chen C. Forecasting the short-term metro passenger flow with empirical mode decomposition and neural networks, *Transportation Research Part C*, Volume 21, Issue 1, April 2012, Pages 148-162, <https://doi.org/10.1016/j.trc.2011.06.009>.
21. Huang NE, Shen Z, Long SR, Wu MC, Shih HH, Zheng Q, Yen NC, Tung CC, Liu HH. The empirical mode decomposition and the Hilbert spectrum for nonlinear and non-stationary time series analysis. *Proceedings of the Royal Society of London A: Mathematical, Physical and Engineering Sciences* 454 (1998) 903-995. doi:10.1098/rspa.1998.0193.
22. Barnhart BL, Eichinger WE. Empirical mode decomposition applied to solar irradiance, global temperature, sun spot number and co2 concentration data. *J Atmos Solar Terr Phys* 2011; 73:1771.
23. Majumder I, Behera MK, Nayak N. Solar Power Forecasting Using a Hybrid EMD-ELM Method. *International Conference on Circuit, Power and Computing Technologies (ICCPCT)*, 20-21 April 2017, doi:10.1109/ICCPCT.2017.8074179.
24. Monjoly S, Andre M, Calif R, Soubdhan T. Hourly forecasting of global solar radiation based on multiscale decomposition methods: A hybrid approach. *Energy*, Volume 119, 15 January 2017, Pages 288-298, doi.org/10.1016/j.energy.2016.11.061.
25. Calif R, Schimtt FG, Huang Y, Soubdhan T. Intermittency study of high frequency global solar radiation sequences under a tropical climate. *Solar Energy*, 98, 349-365, 2013.
26. Huang NE, Wu ML, Qu W, Long SR, Shen SP. Applications of Hilbert Huang transform to non-stationary financial time series analysis. *Applied Stochastic Models in Business and Industry*, 19(3), (2003), 245-268.
27. Angela Z, Faltermeier R, Keck I, Tomé A, Puntonet C, Lang E. Empirical Mode Decomposition – an Introduction. *Proceedings of the International Joint Conference on Neural Networks*, 1-8, 2010.
28. Kutlu, C, Li J, Su Y, Wang Y, Pei G, Riffat S. Annual Performance Simulation of a Solar Cogeneration Plant with Sensible Heat Storage to Provide Electricity Demand for a Small Community: A Transient Model. *Hittite Journal of Science & Engineering*, 6(1), (2010), 75-81.
29. Epias, 2018, Gerçek Zamanlı Üretim, retrieved October 26, 2018, from: <https://seffaflik.epias.com.tr/transparency/uretim/gerceklesen-uretim/gercek-zamanli-uretim.xhtml>

An Energy Investigation of An Organic Rankine Cycle Utilizing Three Organic Fluids

Rabah Touaibi¹  Hasan Koten²  Ozlem Boydak² 

¹Djilali Bounaama University, Laboratory of FIMA, Khemis Miliana, Algeria

²Istanbul Medeniyet University, Department of Mechanical Engineering, Istanbul, Turkey

ABSTRACT

This study presents an energy study of an Organic Rankine Cycle (ORC) by comparing three organic fluids. The latter is considered as a promising cycle for the conversion of heat into mechanical energy adapted to low-temperature heat sources; it uses more volatile organic fluids than water, which generally has high molecular weights, thus allowing operating pressures at temperatures lower than those of the traditional Rankine cycle. This study devoted to the energy analysis of the ORC cycle, taking into account the effect of the operating temperatures and the choice of the organic fluid on the cycle performance. The utilized three fluids were Toluene, R245fa and R123. The results obtained show that the Toluene organic fluid has the best energy efficiency of the cycle with 7.45%.

Keywords:

ORC cycle, Energy Analysis, Organic Fluids, Performance, Toluene

INTRODUCTION

Currently, a continuous increase in energy consumption is noted which has led to environmental problems such as global warming and the depletion of fossil fuels. Total global energy consumption increased from 575 quadrillion British thermal units (BTUs) in 2015 to 736 quadruplets in 2040, with an increase of 28% [1]. Organic Rankine Cycle is one of the most commonly utilized technologies for producing electricity from low-grade heat [2], which can be derived from Geothermal [3,5], Biomass [6,7], Industrial waste [8] and solar energy [9,10]. The organic fluids used by organic Rankine rings are usually: hydrofluorocarbon refrigerants, ammonia, butane, isopentane, toluene depending on the nature of the fluid, isentropic expansion from the dew curve may conserve, decrease, or increase the vapor titer. It is, in fact, the slope of the dew curve in the Mollier diagram that explains this phenomenon specific to the nature of the fluid. The aim of this study is to estimate the mechanical power that can be provided by an organic rankine cycle by studying the effect of the evaporation temperature and the choice of the organic fluid adapted to this type of energy conversion system and to find the organic rankine cycle performance by comparing three different organic fluids; Toluene, R245fa and R123.

DESCRIPTION OF THE ORC CYCLE

The heat transfer fluid at high temperature transfers the heat stored to the evaporator of the ORC cycle. This fluid can reach relatively high temperatures. The organic fluid pressurized by the pump is heated, then evaporated and superheated in the evaporator, by the heat energy from the heat source, transferred to the latter. The superheated steam obtained at the outlet of the evaporator drives the turbine, which is a rotational movement drives an alternator for the production of electricity. The steam at the outlet of the turbine is directed to the condenser where it is cooled by a flow of cooling water.

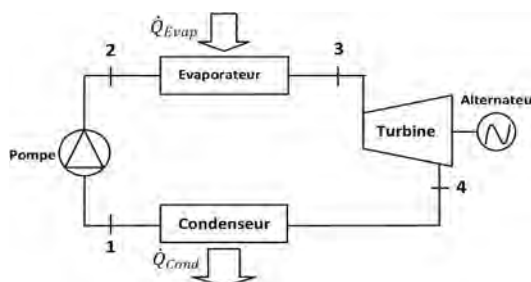


Figure 1. Scheme of Organic Rankine Cycle (ORC)

THERMODYNAMIC MODEL

The ORC cycle is analyzed by applying the principle of conservation of mass and energy according to the first law of thermodynamics, for each of the four

components of the organic Rankine cycle, taking the following hypotheses:

Changes in kinetic energy and potential energy are negligible.

The system is adiabatic (without thermal losses).

The system operates at steady-state.

Mass and Energy Balance of the ORC Cycle

The input and output mass flows are equal in steady state, we have:

$$\dot{m}_1 = \dot{m}_2 = \dot{m}_3 = \dot{m}_4 = \dot{m} \quad (1)$$

Pump

The circulation pump allows the movement of the organic fluid from the low pressure condenser to the evaporator at high pressure, it is possible to determine the consumption of the pump. The energy balance of the pump is written as follows:

$$\dot{W}_p = \dot{m}(h_2 - h_1) \quad (2)$$

The specific work consumed by the pump to compress the fluid is written:

$$W_p = (h_2 - h_1) = v(P_2 - P_1) \quad (3)$$

For an irreversible adiabatic compression, the mechanical efficiency of the pump is introduced as follows:

$$\eta_{Pis} = \frac{\dot{W}_{P\text{rév}}}{\dot{W}_{P\text{irrév}}} = \frac{\dot{W}_{Pis}}{\dot{W}_p} = \frac{(h_{2is} - h_1)}{(h_2 - h_1)} \quad (4)$$

Evaporator

The working fluid enters the evaporator in the liquid state and heated therein at constant pressure P2 to the evaporation temperature, then it evaporates at constant temperature and pressure. The energy balance of the evaporator is written as follows:

$$\dot{Q}_{\text{Evap}} = \dot{m}(h_3 - h_2) \quad (5)$$

Turbine

The expansion in the turbine is considered adiabatic and irreversible with a constant isentropic efficiency which is defined as follows:

$$\eta_{Tis} = \frac{\dot{W}_{T\text{irrév}}}{\dot{W}_{T\text{rév}}} = \frac{\dot{W}_T}{\dot{W}_{Tis}} = \frac{(h_3 - h_4)}{(h_3 - h_{4is})} \quad (6)$$

The energy balance of the turbine is written as follows:

$$\dot{W}_T = \dot{m}(h_3 - h_4) = \dot{m}(h_3 - h_{4is}) \eta_{T.méc} \quad (7)$$

The electric power of the turbine is given by:

$$\dot{W}_{T.ORG}^{elec} = \eta_{gen}^* \dot{W}_{T.ORG} \quad (8)$$

Condenser

The working fluid enters the condenser in the vapor state, condenses at constant temperature and pressure, and exits in the liquid state where it yields a quantity of heat.

The energy balance of the condenser is written as follows:

$$\dot{Q}_{\text{Cond}} = \dot{m}(h_4 - h_1) \quad (9)$$

Performances of the ORC System

The thermal efficiency of organic Rankine cycle is defined as:

$$\eta_{Th} = \frac{\dot{W}_{\text{net.ORG}}}{\dot{Q}_{\text{Evap.ORG}}} \quad (10)$$

$$\dot{W}_{\text{net.ORG}} = \dot{W}_T - \dot{W}_p \quad (11)$$

RESULTS

In this part we compared the thermodynamic behavior of three types of organic fluids R245fa, R123 and toluene. The input parameters of the organic Rankine cycle operation are as follows: $T_{\text{Evap}}=100\text{ }^\circ\text{C}$; $T_{\text{Cond}}=40\text{ }^\circ\text{C}$; $\dot{m}=1\text{ kg/s}$. The thermo-physical characteristics of the working fluids of the various points of the cycle are calculated by the Solkane and Coolpack software [11]. Table 1 represents the thermodynamic characteristics of the various points of the ORC cycle for the three working fluids.

In order to jointly consider the fluid having the highest net mechanical power, and the best energy efficiency. This study allowed us to compare the behavior of different types of working fluid under similar conditions. The thermodynamic performances of the ORC cycle of the three fluids are shown in Table 2.

The results show that the Toluene organic fluid appears to be a good compromise for these two criteria, it is the fluid

Table 1. Characteristic thermodynamic points of ORC cycle

| | T[°C] | P[bar] | h[kJ/kg] | s[kJ/kg.K] | x[-] |
|------------------------|-------|---------|----------|------------|------|
| Working fluid: Toluene | | | | | |
| 1 | 40 | 0.07907 | -132.3 | -0.3799 | 0 |
| 2 | 40.02 | 0.7475 | -132.3 | -0.3799 | 1 |
| 3 | 100 | 0.475 | 347.1 | 0.9306 | 1 |
| 4 | 45.37 | 0.07907 | 278.1 | 0.9306 | 1 |
| Working fluid: R123 | | | | | |
| 1 | 40 | 1.547 | 241.9 | 1.142 | 0 |
| 2 | 40.25 | 7.868 | 242.3 | 1.142 | 1 |
| 3 | 100 | 7.868 | 442.5 | 1.694 | 1 |
| 4 | 50.08 | 1.547 | 414.6 | 1.694 | 1 |
| Working fluid: R245fa | | | | | |
| 1 | 40 | 2.496 | 252.6 | 1.179 | 0 |
| 2 | 40.4 | 12.69 | 253.4 | 1.179 | 1 |
| 3 | 100 | 12.69 | 474.1 | 1.791 | 1 |
| 4 | 50.44 | 2.496 | 444.2 | 1.791 | 1 |

Table 2. Thermodynamic performances of the ORC cycle

| Performances | Working fluids | | |
|---------------------------------|----------------|--------|--------|
| | Toluene | R123 | R245fa |
| \dot{W}_{Pump} (kW) | 0.1089 | 0.4445 | 0.7853 |
| \dot{Q}_{Evap} (kW) | 479.4 | 200.1 | 220.8 |
| \dot{W}_{Turbine} (kW) | 69 | 27.82 | 29.91 |
| \dot{Q}_{Cond} (kW) | 410.5 | 172.7 | 191.7 |
| $\dot{W}_{\text{net. ORC}}$ | 68.92 | 27.38 | 29.12 |
| $\eta_{\text{th. ORC}}$ (%) | 14.38 | 13.68 | 13.19 |

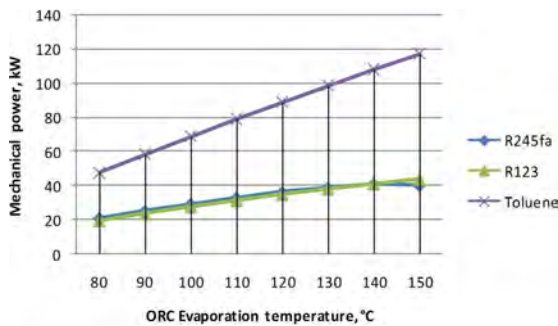


Figure 2. Variation of mechanical power of Turbine with ORC evaporation temperature according to the studied working fluids

that has the highest value of the net mechanical power $\dot{W}_{\text{net. ORC}} = 68.92$ kW compared with the other fluids, it is also a fluid which presents the best energetic efficiency of the cycle which equals $\zeta_{\text{ORC_Toluene}} = 14.38\%$ compared to that of the organic fluid R123 $\zeta_{\text{ORC_R123}} = 13.68\%$ and that of the organic fluid $\zeta_{\text{ORC_R245fa}} = 13.19\%$

Parametric Study

In this part, we studied the influence of the evaporation temperature of the ORC cycle on the performances of the organic Rankine cycle, namely the net power delivered by the ORC cycle and the cycle efficiency using the three organic fluids. To do this by keeping the condensing temperature constant, that is to say by fixing the condensation temperature ($T_{\text{Cond}} = 40^\circ\text{C}$), and by varying the evaporation temperature in the range of $[80^\circ\text{C} - 150^\circ\text{C}]$. Fig. 2 shows the effect of the evaporation temperature on the net mechanical power provided by the ORC cycle for the three organic fluids used. The results show that the mechanical power supplied increases with the increase of the evaporation temperature for the three fluids. The Toluene fluid gives a very high mechanical power relative to the other fluids.

Fig. 3 shows the effect of the evaporation temperature on the thermal power received by the evaporator to feed the organic Rankine cycle. The results show that the thermal power required for the supply of the ORC cycle is increased with the increase of the evaporation temperature, the working fluid Toluene uses a lot of energy during its vaporization at the evaporator.

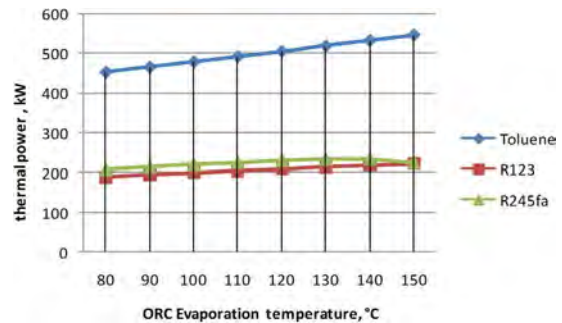


Figure 3. Variation of thermal power of evaporator with ORC evaporation temperature according to the studied working fluids

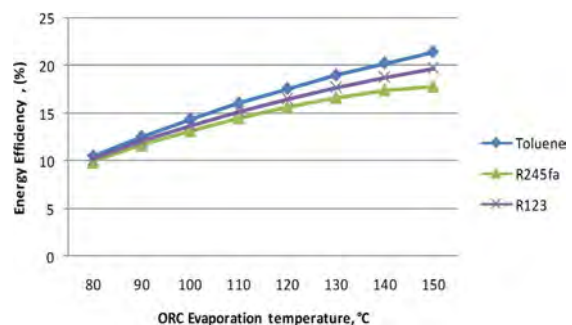


Figure 4. Variation of Energy Efficiency with ORC evaporation temperature according to the studied working fluids

CONCLUSION

This work focused on the energy study of an Organic Rankine Cycle (ORC) for the production of electrical energy, based on the use of an organic fluid. The parametric study of the organic Rankine cycle has made it possible

to select the best organic fluid with good thermodynamic performance, which is the Toluene which is the fluid with the highest value of the net mechanical power and a yield of high compared to other fluids. On the other hand, we have been able to analyze and highlight the influence of the evaporation temperature and to find that the cycle efficiency increases significantly with the increase of the evaporation temperature especially for the Toluene fluid where the efficiency energy increase from 10.5% to 21.45 % over a temperature range of 80°C-150 °C.

REFERENCES

1. Energy Information Administration (2017). International energy outlook, USA: Accessed from "<https://www.eia.gov/outlooks/ieo/#1>".
2. Braimakis, K., & Karellas, S. (2018). Energetic optimization of regenerative Organic Rankine Cycle (ORC) configurations. *Energy Conversion and Management*, 159, 353-370.
3. Heberle, F., & Brüggemann, D. (2010). Exergy based fluid selection for a geothermal Organic Rankine Cycle for combined heat and power generation. *Applied Thermal Engineering*, 30(11-12), 1326-1332.
4. Liu, Q., Duan, Y., & Yang, Z. (2013). Performance analyses of geothermal organic Rankine cycles with selected hydrocarbon working fluids. *Energy*, 63, 123-132.
5. Bu, X., Wang, L., & Li, H. (2013). Performance analysis and working fluid selection for geothermal energy-powered organic Rankine-vapor compression air conditioning. *Geothermal Energy*, 1(1), 2.
6. Drescher, U., & Brüggemann, D. (2007). Fluid selection for the Organic Rankine Cycle (ORC) in biomass power and heat plants. *Applied thermal engineering*, 27(1), 223-228.
7. Taljan, G., Verbič, G., Pantoš, M., Sakulin, M., & Fickert, L. (2012). Optimal sizing of biomass-fired Organic Rankine Cycle CHP system with heat storage. *Renewable Energy*, 41, 29-38.
8. Sun, W., Yue, X., & Wang, Y. (2017). Exergy efficiency analysis of ORC (Organic Rankine Cycle) and ORC-based combined cycles driven by low-temperature waste heat. *Energy Conversion and Management*, 135, 63-73.
9. Rayegan, R., & Tao, Y. X. (2011). A procedure to select working fluids for Solar Organic Rankine Cycles (ORCs). *Renewable Energy*, 36(2), 659-670.
10. Shaaban, S. (2016). Analysis of an integrated solar combined cycle with steam and organic Rankine cycles as bottoming cycles. *Energy Conversion and Management*, 126, 1003-1012.
11. Solkane 8.0.0, Solvay Special Chemicals.

Antimicrobial and Antioxidant Activities of *Zingiber officinale* (Ginger) and *Alpinia officinarum* (Galangal)

Gulcin Alp Avcı¹  Emre Avcı¹  Gizem Ozluk Cilak²  Sule Coskun Cevher³ 

¹Hitit University, Department of Molecular Biology and Genetics, Corum, Turkey

²Hitit University, Department of Food Engineering, Corum, Turkey

³Gazi University, Department of Biology, Ankara, Turkey

ABSTRACT

The use of spices in the treatment of health problems has been a tradition in the world since early ages. *Alpinia officinarum* Hance (galangal) and *Zingiber officinale* Roscoe (ginger) are aromatic plants, enriched with bioactive compounds providing the usage for their therapeutic properties. In this study, the ethanol and water (ultra-pure) extracts of galangal and ginger are used to determine the antimicrobial and antioxidant properties. Antioxidant effect was evaluated based on total antioxidant status performed by automated colorimetric measurement method and DPPH free radicals scavenging effects done by spectrophotometric method; whilst antimicrobial effect was observed on *Enterococcus faecalis*, *Escherichia coli*, *Staphylococcus aureus*, *Pseudomonas aeruginosa* and *Candida albicans*. The results indicate that, both ginger and galangal extracts demonstrated effective antimicrobial and antioxidant properties. Their consumption may restrain the oxidation and prevent or delay the degenerative diseases as well as their extracts can be used as antimicrobial agents.

Keywords:

Alpinia officinarum Hance; *Zingiber officinale* roscoe; Galangal; Ginger; Antimicrobial; Antioxidant; Free radical scavenging.

INTRODUCTION

The use of spices in the treatment of health problems has been a tradition in the world since early ages. As consumer preferences shift to natural products, the use of spices and natural aromatic plants as antioxidants and antimicrobials instead of synthetic food additives has been back on the agenda recently. The importance of spices and aromatic plants has increased due to the side effects of synthetic drugs and the fact that bacteria can easily develop resistance to these synthetic drugs [1–4].

Alpinia officinarum Hance (galangal) and *Zingiber officinale* Roscoe (ginger) are aromatic plants, both belong to Zingiberaceae family, rhizomes of which are used as spice [5]. Galangal is enriched with bioactive components providing the usage as medicine mostly in Far East countries in many diseases such as cold, bronchitis, stomach ache, diabetes, ulcer, abdominal swelling, diarrhea, vertigo, neuropathia, rheumatoid arthritis and inflammatory bowel diseases etc. [6, 7]. Ginger is well known for its bioactive constituents, revealing antimicrobial, antifungal and antioxidant effects. It is widely used for its anti-inflammatory and anti-tumorigenic functions in addition to aiding properties of cholesterol

lowering and digestive problems [8–10].

These therapeutic properties of spices derive from their chemical compounds that lead to have antioxidant and antimicrobial effects. Antimicrobial activity varies depending on the type and concentration of the spice as well as microbial density and diversity. Antimicrobial effect is mostly provided by phenolic and terpenoid compounds containing hydroxyl group which has the inhibitory effect via destroying the phospholipid layer of cell membrane. Thus, the increased permeability of cell membrane causes all the cell content comes out. Spices are effective at all stages of microbial growth such as lengthening the lag phase or decreasing the growth rate in exponential phase and the total reduction in cell count [5, 11]. The antimicrobial activity of ginger was studied on some microorganisms such as *Pseudomonas aeruginosa*, *Staphylococcus aureus*, *Salmonella Typhimurium* and *Listeria monocytogenes*; whereas *Bacillus subtilis*, *Candida albicans*, *Enterococcus faecalis*, *Enterobacter aerogenes*, *Enterococcus durans*, *Enterococcus faecium*, *Escherichia coli*, *Klebsiella pneumoniae*, *Listeria innocua*, *Pseudomonas fluorescence*, *Salmonella enteritidis*, *Salmonella infantis*, *Salmonella kentucky*

Article History:

Received: 2019/10/21

Accepted: 2020/03/06

Online: 2020/03/26

Correspondence to: Gizem Ozluk Cilak,
Hitit University Faculty of Engineering,
Department of Food Engineering, 19030,
Corum, Turkey

E-Mail: gizem.ozluk@gmail.com Phone:
+90 532 740 86 07

and *Staphylococcus epidermidis* were the microorganisms studied for galangal antimicrobial activity [10, 12, 13].

Oxidation is a chemical reaction that can produce free radicals and thus leads to chain reactions that can damage the cells of organism. Antioxidant substances prevent degenerative diseases via restraining oxidation. The oxidation blocking path of spices is provided by phenolic compounds whereby free radical scavenging, compounding with metal ions and preventing the formation of singlet oxygen. It was observed that the higher the number of hydroxyl groups in the aromatic ring are, the higher antioxidant activity of the spice is [5, 14-16]. It has been proposed to use free radical scavenging, one of the antioxidant mechanisms, for therapeutic purposes. Radical scavengers may directly affect peroxide radicals and end the oxidation chain reactions [16].

It was shown by the studies that the extractive value of the spices shows difference according to the solvent used [9, 16]. In this study, the ethanol, and water (ultra-pure) extracts of *Alpinia officinarum* Hance (galangal) and *Zingiber officinale* Roscoe (ginger) are used to determine the antimicrobial and antioxidant properties based on total antioxidant status and DPPH free radicals scavenging effects.

MATERIAL AND METHODS

Samples

Zingiber officinale (Ginger) and *Alpinia officinarum* (Galangal) samples were obtained commercially.

Preparation of Extracts

The preparation of extracts is schematized in Fig. 1. After extraction procedure samples were stored at 4°C.

Determination of Antimicrobial Activity

Microorganisms

Antimicrobial activities of extracts prepared with ethanol and water were used against five microorganisms. In order to represent gram positive bacteria, *S. aureus* ATCC 25923 and *E. faecalis* ATCC 29212 are used; whereas *E. coli* ATCC 25922 and *P. aeruginosa* (ATCC 27853) were used to represent gram negative bacteria. In addition, one fungus *C. albicans* ATCC 10231 were also used to determine the antimicrobial and antioxidant effects.

Agar-well and Disc Diffusion Method

The antimicrobial activity was determined by diffusion methods (disc and agar-well). Bacterial cultures were

grown at 37°C for 24 h and *C. albicans* was grown at 25°C for 48 h. Suspensions were adjusted according to McFarland 0.5 standard. 100 µl microbial cultures added with Mueller-Hinton Agar (MHA) in Petri plates. 6-mm agar-well opened or disc prepared using paper (Watmann no. 4) placed on MHA. Extracts (15 µL) were inoculated in wells or on discs. Then, plates were incubated for 24-48 hours. After incubation, diameter of the inhibition zone was measured.

Determination of Antioxidant Activity

DPPH Radical Scavenging Assay

Radical scavenging activity was determined by a spectrophotometric method developed by Blois (1958) and Khalaf et al. (2008) [18, 19]. Tests were repeated three times. Ascorbic acid was used as positive control. Inhibition ratio (%) of free radical was calculated according to formula given below where IDA is the inhibition of DPPH activity:

$$IDA(\%) = \frac{(A_{blank} - A_{sample})}{A_{blank}} \times 100 \quad (1)$$

Total Antioxidant Status assay

The extracts were examined in terms of total antioxidant

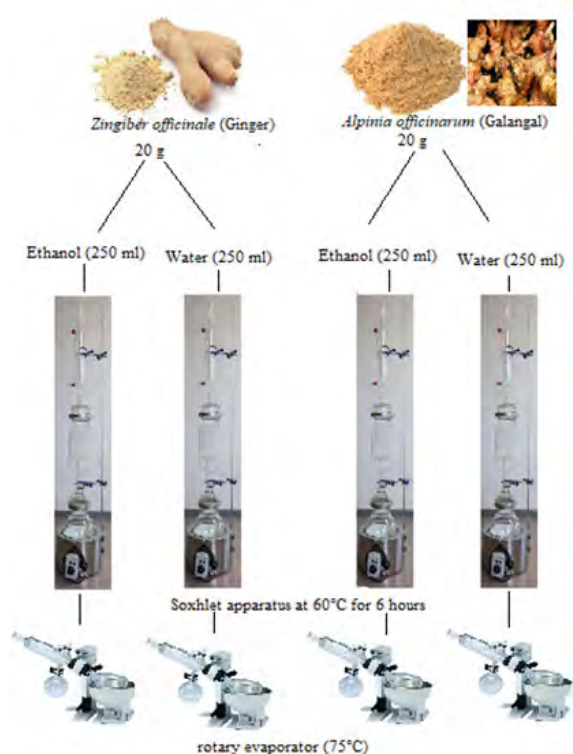


Figure 1. Extracts' preparation.

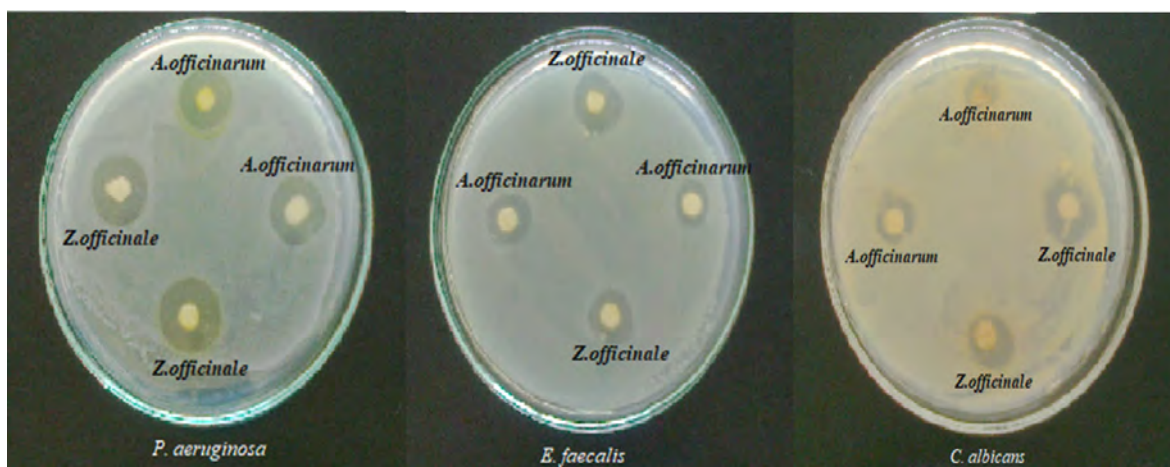


Figure 2. Antimicrobial effects on some pathogen strains of *Z. officinale* and *A.officinarum* by diffusion method.

status (TAS) by a colorimetric method developed by Erel (2004). In this method, Fenton reaction is used to produce hydroxyl radical and bright yellowish-brown dianisyl radical is produced by reacting with colorless substrate o-dianisidine. Results were expressed as micromolar Trolox equivalents per liter ($\mu\text{mol Trolox Eq/L}$).

Statistical analysis

Statistical analysis of this study was performed on the data by SPSS 22.0 (SPSS Inc., Chicago). The statistical significance determined at $p < 0.05$ in this study. All results were expressed as means \pm standard deviations (SD).

RESULTS AND DISCUSSION

Determination of antimicrobial and antifungal activity

Looking at the data observed in Table 1 and Fig. 2, it is available that ginger had slightly higher antimicrobial effect on all species than galangal ($P < 0.05$). The antimicrobial effect is considered as weak (< 12 mm), moderate ($12 \leq 20$ mm) and strong (≥ 20 mm) according to Pilla et al [20]. Ethanol extracts of the plants frankly made higher antimicrobial effect than distilled water extracts. Ethanol extracts showed significant antibacterial activity

Table 1. Antimicrobial activities of Ginger and Galangal extracts by Disc diffusion method and Agar diffusion method.

| | Strains (Inhibition zone diameter, mm) | | | |
|------------------------------|--|----------------|---------------------------------------|----------------|
| | <i>Zingiber officinale</i> (Ginger) | | <i>Alpinia officinarum</i> (Galangal) | |
| <i>Disc diffusion method</i> | | | | |
| <i>S. aureus</i> | 13.5 \pm 1.5 | 11.0 \pm 1.0 | 12.5 \pm 2.0 | 10.4 \pm 2.2 |
| <i>E. faecalis</i> | 13.2 \pm 2.8 | 10.2 \pm 1.8 | 12.0 \pm 1.5 | 9.7 \pm 1.6 |
| <i>P. aeruginosa</i> | 15.8 \pm 1.2 | 11.6 \pm 1.4 | 14.1 \pm 1.9 | 11.2 \pm 1.5 |
| <i>E. coli</i> | 8.4 \pm 0.6 | ND | 7.1 \pm 0.9 | ND |
| <i>C. albicans</i> | 11.2 \pm 1.3 | 9.4 \pm 0.6 | 10.8 \pm 1.2 | 8.8 \pm 0.7 |
| <i>Agar diffusion method</i> | | | | |
| <i>S. aureus</i> | 15.2 \pm 1.0 | 12.0 \pm 1.0 | 13.2 \pm 1.8 | 11.4 \pm 1.6 |
| <i>E. faecalis</i> | 14.8 \pm 0.5 | 11.6 \pm 1.5 | 13.5 \pm 1.5 | 10.8 \pm 1.2 |
| <i>P. aeruginosa</i> | 18.5 \pm 2.8 | 14.0 \pm 2.0 | 16.6 \pm 2.6 | 13.7 \pm 2.7 |
| <i>E. coli</i> | 10.2 \pm 1.4 | 6.0 \pm 1.5 | 9.1 \pm 0.6 | ND |
| <i>C. albicans</i> | 13.2 \pm 2.2 | 11.6 \pm 1.4 | 12.1 \pm 1.8 | 10.2 \pm 0.8 |

DW, Distilled water; ND, not determined.

Values are expressed as mean \pm standard deviation.

Ethanol extracts showed significant antibacterial activity ($P < 0.05$) against all tested bacterial strains

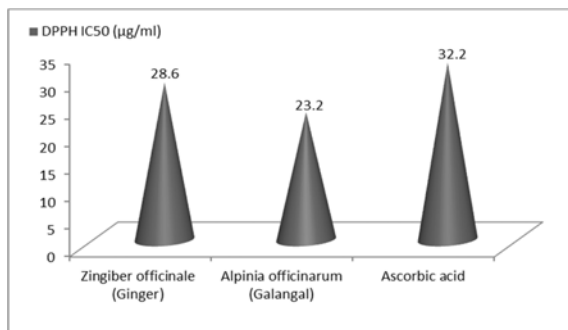


Figure 3. DPPH radical scavenging of Ginger and Galangal ethanol extracts.

vity against all tested bacterial strains ($P < 0.05$). Ginger and galangal extracts showed week antimicrobial effect on *E. coli* whereas the ethanol extracts of both plants showed moderate antimicrobial effect on *S. aureus*, *E. faecalis* and *P. aeruginosa* ($P < 0.05$). *E. coli* was the most durable strain whilst *P. aeruginosa* is the most unstable one. The antifungal activity of both ginger and galangal extracts were found to be week against *C. albicans* in disc diffusion; moderate in agar diffusion method.

The inhibition zones were found larger in agar diffusion method than those in disc diffusion method. The difference can easily be explained by the reason that the extracts are not absorbed well in discs as in agar diffusion method. However, standards are available for disc diffusion method, such as the type of media used, agar percentage, and thickness of media, which lead no ambiguity.

Srividya et al. [21] made experiments on hydro alcoholic extract by hot and cold maceration and methanol extract by percolation process of galangal antimicrobial effect. They found that all three extracts showed moderate antimicrobial activity against the *B. cereus*, *S. aureus*, *P. aeruginosa*, *E. coli* but no antifungal activity against *A. niger* and *C. albicans*. This can be concluded by the reason that extraction method can show an alteration in the result because in the present study antifungal activity was observed. Sharef et al. [22] studied the antimicrobial effect of ginger methanolic extract comparing with the standard

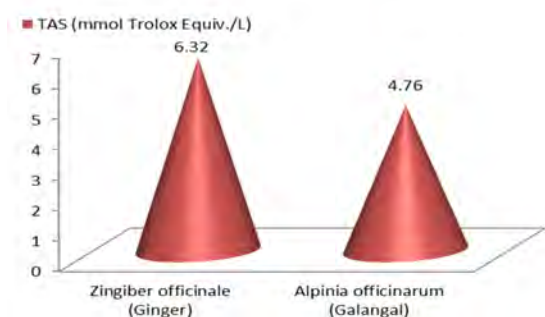


Figure 4. The antioxidant activities of Ginger and Galangal ethanol extracts.

antibiotics on *Escherichia coli*, *Pseudomonas aerogenosa*, *Proteus mirabilis*, *Staphylococcus aureus* and *Klebsiella pneumonia* by using the agar diffusion method. They have revealed that methanolic extracts of ginger showed stronger antimicrobial effect compared to Streptomycin, Rifambin and Cefotixime. This study can clearly help interpreting the present results of ginger and galangal extracts have effective antimicrobial properties than the standard antibiotics, though their moderate and week inhibition zones.

Determination of Antioxidant Activity as DPPH Radical Scavenging and Total Antioxidant Status

The antioxidant properties were determined based on DPPH free radicals scavenging effects and total antioxidant status. DPPH radical scavenging and antioxidant activities of ginger and galangal ethanol extracts are presented in Fig. 3 and Fig. 4. The effect of antioxidants on DPPH derives from their hydrogen donating ability [23]. The results obtained showed that the ethanol extracts of ginger and galangal radical scavenging abilities were nearly the same when compared to ascorbic acid. The lower IC50 value is, the higher radical scavenging effect is; therefore, galangal was found to have higher scavenging ability than ginger. Khalaf et al. [18] found similar results in their own study when comparing the radical scavenging effect of *Zingiber officinale* Roscoe with ascorbic acid. These results can be interpreted as ginger and galangal have antioxidant effect as much as ascorbic acid has. Scavenging free radicals are proposed to be used for therapeutic expectations [16]. Ghazemzadeh et al [23] found in their study that methanol extracts of ginger have good free radical scavenging ability comparing with alpha-tocopherol. Köse et al. [24] found high but different DPPH radical scavenging values of water, water-ethanol and ethanol extracts of galangal comparing with BHA, BHT, trolox and alpha-tocopherol. These studies indicate that the extract chemical as well as the compared material makes disparate effect on the results.

In this study, the total antioxidant status was found to be higher in ginger than galangal in contrast with the scavenging effect. Çiftçi et al. [25] expressed their study results in beneficial usage of ginger on total antioxidant status which they used the Erel [19] method to analyse. No total antioxidant status essays of galangal has been recorded in researches, hence, our study is expected to have contribution to literature.

CONCLUSION

The present study demonstrated that both ginger and galangal extracts have effective antimicrobial and antioxidant properties. Their consumption may restrain the

oxidation and prevent or delay the degenerative diseases. Discovering novel antimicrobial agents have become important against the microbial infections. This study shows that ginger and galangal extracts can be used as antimicrobial agents.

References

1. Çoban Ö.E., Patır B. Use of Some Spices and Herbs Antioxidant Affected in Foods. *Electronic Journal of Food Technologies*, 5(2): 7-19, 2010.
2. Bérty J. Thoughts and facts about antibiotics: Where we are now and where we are heading. *The Journal of Antibiotics*. 65: 385-395, 2012.
3. Iyer A, Panchal S, Poudyal H, Brown L. Potential Health Benefits of Indian Spices in the Symptoms of the Metabolic Syndrome: A Review. *Indian Journal of Biochemistry and Biophysics*, 46 (6):467-81, 2009.
4. Martins JJ. Indian Spices and Biotherapeutics in Health and Chronic Disease. *Health*, 10 (4): 374-380, 2018.
5. Akgül, A. Baharat Bilimi ve Teknolojisi. *Gıda Teknolojisi Dergisi Yayınları*, No:15, 450 s., Ankara, 1993.
6. Honmore VS, Kandhare AD, Kadam PP, Khedkar VM, Sarkar D, Bodhankar SL, Zanwar AA, Rojatkar SR, Natu AD. Isolates of *Alpinia officinarum* Hance as COX-2 inhibitors: Evidence from anti-inflammatory, antioxidant and molecular docking studies. *International Immunopharmacology*, 33: 8-17, 2016.
7. Basri AM, Taha H, Ahmad N. A Review on the Pharmacological Activities and Phytochemicals of *Alpinia officinarum* (Galangal) Extracts Derived from Bioassay-Guided Fractionation and Isolation. *Pharmacogn Rev*. 11(21): 43-56, 2017.
8. Srinivasan K. Ginger rhizomes (*Zingiber officinale*): A spice with multiple health beneficial potentials. *PharmaNutrition*, 5 (1): 18-28, 2017.
9. Arawande JO, Akinnusotu A, Alademeyin JO. Extractive Value and Phytochemical Screening of Ginger (*Zingiber officinale*) and Turmeric (*Curcuma longa*) Using Different Solvents. *International Journal of Traditional and Natural Medicines*, 8 (1): 13-22, 2018.
10. Noori S, Zeynali F, Almasi H. Antimicrobial and antioxidant efficiency of nanoemulsion-based edible coating containing ginger (*Zingiber officinale*) essential oil and its effect on safety and quality attributes of chicken breast fillets. *Food Control*, 84: 312-320, 2018.
11. Aybakır M. Investigating antimicrobial effects of spices in hurdle technology. Master Thesis. Ankara University, Graduate School of Applied Sciences, Department of Food Engineering. Ankara, 2015.
12. Azadpour M, Azadpour N, Bahmani M, Hassanzadazar H, Kopaei MR, Naghdi N. Antimicrobial effect of Ginger (*Zingiber officinale*) and mallow (*Malva sylvestris*) hydroalcoholic extracts on four pathogen bacteria. *Der Pharmacia Lettre*, 8 (1):181-187, 2016.
13. Özkinalı S, Şener N, Gür M, Güney K, Olgun Ç. Antimicrobial Activity and Chemical Composition of Coriander & Galangal Essential Oil. *Indian Journal of Pharmaceutical Education and Research*. 51 (3): 221-224, 2017.
14. Baublis AJ, Clydesdale FM, Decker EA. Antioxidants in Wheat-Based Breakfast Cereals. *Cereals Foods World*. 45: 71-74, 2017.
15. Serafini M, DelRio D. Understanding the association between dietary antioxidants, redox status and disease: is the total antioxidant capacity the right tool. *Redox report*. 9 (3): 145-52, 2004.
16. Tohma H, Gülçin İ, Bursal E, Gören AC, Alwasel SH, Köksal E (2017). Antioxidant activity and phenolic compounds of ginger (*Zingiber officinale* Rosc.) determined by HPLC-MS/MS. *Journal of Food Measurement and Characterization*, 11 (2): 556-566, 2017.
17. Blois MS. Antioxidant determinations by the use of a stable free radical. *Nature*. 29: 1199-1200, 1958.
18. Khalaf NA, Shakya AK, Al-Othman A, El-Agbar Z, Farah H. Antioxidant Activity of Some Common Plants. *Turk J Biol*. 32: 51-55, 2008.
19. Erel Ö. A novel automated direct measurement method for total antioxidant capacity using a new generation, more stable ABTS radical cation. *Clinical Biochemistry*. 37: 277- 285, 2004.
20. Pillai MK, Ismail R, Sasidharan S, Asmawi MZ. Antioxidant and antimicrobial activities of rhizome extracts from Malaysian species of *Alpinia galanga* and *Alpinia officinarum*. *Pharmacologyonline*. 1: 366-375, 2019.
21. Srividya AR, Dhanabal SP, Misra VK, Suja G. Antioxidant and Antimicrobial Activity of *Alpinia officinarum*. *Indian Journal of Pharmaceutical Sciences*. 72 (1): 145-148, 2010.
22. Shareef HK, Muhammed HJ, Hussein HM, Hameed IH. Antibacterial Effect of Ginger (*Zingiber officinale*) Roscoe and Bioactive Chemical Analysis using Gas Chromatography Mass Spectrum. *Oriental Journal of Chemistry*. 32 (2): 817-837, 2016.
23. Ghasemzadeh A, Jaafar HZE, Rahmat A. Antioxidant Activities, Total Phenolics and Flavonoids Content in Two Varieties of Malaysia Young Ginger (*Zingiber officinale* Roscoe). *Molecules*. 15: 4324-4333, 2010.
24. Köse LP, Gülçin İ, Görenc AC, Namiesnikd J, Martinez-Ayala AL, Gorinsteinf S. LC-MS/MS analysis, antioxidant and anticholinergic properties of galanga (*Alpinia officinarum* Hance) rhizomes. *Industrial Crops and Products*. 74: 712-721, 2015.
25. Çifci A, Tayman C, Yakut Hİ, Halil H, Çakır E, Çakır U, Aydemir S. Ginger (*Zingiber officinale*) prevents severe damage to the lungs due to hyperoxia and inflammation. *Turk J Med Sci*. 48 (4): 892-900, 2018.

Stress Degradation Studies of Macrolide Antibiotics “Roxithromycin, Tilmicosin and Tylosin” by Using HPLC

Bediha Akmesse 

Hitit University, Department of Chemistry, Corum, Turkey

ABSTRACT

Stress degradation studies control the behavior and impurities of drugs under various stress conditions. The present research is related to all degradation studies including acidic, alkaline, thermal and photo stability on the drug substance according to International Conference on Harmonization (ICH) guidelines. In this study, the degradation profiles of macrolide antibiotics “roxithromycin (ROX), tilmicosin (TIL) and tylosin (TYL)” under varied stress conditions were investigated. The behavior of these drugs under hydrolytic, oxidative, thermal and photolytic conditions were determined by high performance liquid chromatography (HPLC).

Keywords:

Degradation; Macrolide; Roxithromycin; Tilmicosin; Tylosin.

INTRODUCTION

Antibiotics are natural or synthetic chemical substances produced by microorganisms to kill or stop the growth of another microorganisms [1]. They are used in treatment of diseases in humans. They are used in animals for the treatment of diseases and as feed-additives for rapid growth of animals [2]. ROX is 14-membered ring macrolide antibiotic, which is effective against certain respiratory tract, urinary and soft tissue infections [3]. It is a semi-synthetic, derived from erythromycin. TIL is a semi-synthetic, derived from desmycosin, commonly used in veterinary treatment for bacterial respiratory diseases. It is 16-membered ring macrolide antibiotic [4-6]. TYL is a complex of 16-member macrolides obtained from the fermentation of *Streptomyces fradie*. It is generally used as a growth promotant for food-producing animals (Fig. 1). It is effective against Gram-positive bacteria [7].

Stability is a critical parameter affecting the purity, potential and safety of the drugs, so stability studies are one of important parameters of the quality control of drugs [8, 9]. Stability studies are important to indicate the expiration date, appropriate storage and transport conditions of drugs. In addition, stress degradation studies are important to simulate the unintended exposure of drugs to undesirable conditions during production, storage, usage and administration.

The present manuscript describes the stress degradation studies of ROX, TIL and TYL under various

Article History:

Received: 2019/11/11

Accepted: 2020/01/14

Online: 2020/03/26

Correspondence to: Bediha Akmesse, Hitit University, Department of Chemistry, Faculty of Arts and Sciences, 19030, Corum, Turkey

E-Mail: bedihaakmesse@hitit.edu.tr Phone: +90 364 227 7000

Fax: +90 364 227 7005

conditions prescribed by ICH. The ICH guidelines are important not only to ensure the stability of drug molecules, but also for the identification and structure of degradation products and for the selection of possible stabilizers to prevent from degradation [10].

In this study, degradation of ROX, TIL and TYL under acidic and alkaline, thermal, oxidation and ultraviolet (UV) light conditions were investigated. This study will be valuable for ensuring the chemical stability

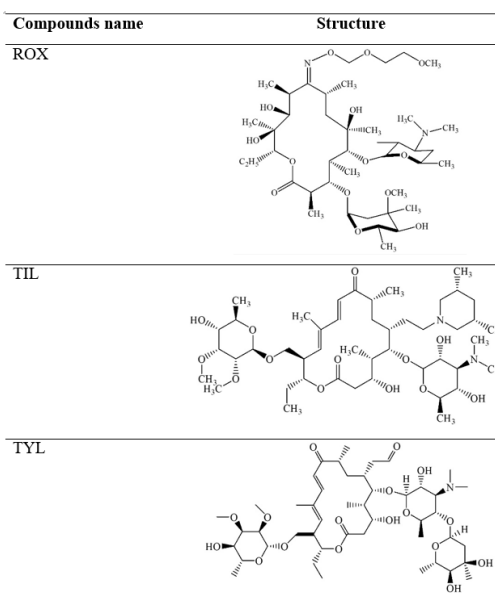


Figure 1. Molecular forms of compounds studied.

of these substances and for developing appropriate formulations and screening for appropriate storage conditions. To our knowledge, only one study in the literature demonstrated the stress degradation conditions for ROX. Degradation products were determined and kinetic studies were conducted in the study however degradation rates following stress conditions were not calculated. So, our study was the first study that calculated the degradation rates for ROX after treatment with stress parameters [11]. No reports have been found in the literature about the identification of stability and degradation products of TIL and TYL.

MATERIAL AND METHODS

Chemical and Reagents

ROX, TIL, TYL and Methanol (HPLC- grade) were purchased from Sigma–Aldrich. Acetonitrile (HPLC-grade) and sodium hydroxide were purchased from Merck. Ortho-phosphoric acid (min. 85%), hydrochloric acid (37%, d: 1.19 g cm⁻³) and hydrogen peroxide (35%, d: 1.13 g cm⁻³) were purchased from Riedel de Haen.

Apparatus and Chromatographic Procedure

The chromatographic apparatus consisted of a model LC-20 AD quaternary pump, a model DGU 20A vacuum degasser and a model SPD-M 20A DAD detector, a model CTO-20AC column oven, all from Shimadzu (Kyoto, Japan). The separation was performed on Intertsil® ODS-4V (5µm, 4.60 x 250 mm) column. The wavelengths were set at 210 nm for ROX, 288 nm for TIL and TYL. Mettler Toledo (Greifensee, Switzerland) was used for pH measurements. Ultra-pure water device, Human Corp. Zener Power I brand was used. The mobile phase was a mixture of 40:60% (v/v) acetonitrile: water containing 20 mM ortho-phosphoric acid and pH was adjusted to 2.8 with 1.0 M NaOH. Isocratic flow rate is 1.0 mL/min. The column temperature is 35 °C. [12-14]. Injection volume was 20 µL. The mobile phase was prepared daily and degassed with ultrasonicator before use.

Preparation of Stock Solutions

Stock solutions (200 ppm) were prepared by dissolving the studied drugs in methanol. 2.0 M HCl, 2.0 M NaOH, 30% H₂O₂ and 6% H₂O₂ solution were dissolved in purified water. All stock solutions were stored in the dark and at +4 °C.

Stress-Degradation Studies

Stress degradation studies were attempted to stress conditions of acidic, alkaline, oxidation, heat in oven (at 100°C)

and UV light to detect the degradation products of ROX, TIL and TYL under chromatographic conditions previously described [15]. For acidic degradation, to a 5.0 mL stock solutions of each drug was added an appropriate volume of 2.0 M HCl and the mixture was diluted to 10 mL with water to achieve a molarity of 0.1 M and 1.0 M HCl, respectively. The mixtures were kept at room temperature for 24 h. Alkaline degradation studies were carried out in a similar manner to that of acidic degradation with molarities of 0.1 M and 1 M NaOH. The mixtures were kept at room temperature for 24 h. For oxidative stress, to a 5.0 mL stock solutions of each drug 5.0 mL of 6% (v/v) H₂O₂ and 30% (v/v) H₂O₂ were separately added to reach final concentrations of 3% and 15% (v/v) H₂O₂, respectively. The mixtures were kept at room temperature for 24 h. These experiments also were conducted at 75°C for 30 min while keeping all other conditions constant.

The studied drugs were exposed at 100°C for 6 h and 24 h to determine whether the drugs were degraded by heat. They were dissolved and diluted with methanol to achieve final concentrations of 100 ppm. For photolytic stress, drug samples, in solid state, were irradiated with UV radiation having peak intensities at 254 and 360 nm for 6 and 24 h. They were dissolved and diluted with methanol to achieve final concentrations of 100 ppm.

RESULTS AND DISCUSSION

Stress degradation studies are critical parameters that help to determine the stability of the drug substance, the ways of degradation and the possible degradation products. The rates of degradation of ROX, TIL and TYL under different degradation conditions were calculated (Table 1). Fig. 2-4 represented the chromatograms for degradation of ROX, TIL and TYL, respectively, under different stress conditions.

ROX was completely degraded under alkaline conditions (1.0 M NaOH solution) at 75 °C indicating that ROX has much better stability under alkali conditions than acidic ones at room temperature. It was found that ROX was sensitive to both concentrations of H₂O₂ at 75 °C temperature. The drug was highly stable to thermal and photolytic conditions. It was observed that TIL was resistant to acidic conditions and oxidation. TIL was partially degraded in 1.0 M NaOH solution at 75 °C indicating that degradation under basic conditions was found to be concentration and temperature dependent. It was also partially degraded under thermal and photolytic conditions. TYL was found to be sensitive to acidic, basic and oxidative conditions and almost all drug were degraded. It was partially degraded under thermal and photolytic conditions.

Table 1. The rates of degradation calculated for ROX, TIL and TYL.

| Degradation Conditions | | ROX% | TIL% | %TYL |
|------------------------|--|-------|-------|-------|
| Acidic conditions | 0.1 M HCl | - | - | 92.31 |
| | 1.0 M HCl | 100 | 6.78 | 97.67 |
| | 0.1 M HCl at 75 °C | 10.27 | 11.23 | 96.28 |
| | 1.0 M HCl at 75 °C | 100 | 11.66 | 98.49 |
| Alkaline conditions | 0.1 M NaOH | - | - | 99.23 |
| | 1.0 M NaOH | 37.93 | 5.59 | 99.51 |
| | 0.1 M NaOH at 75 °C | - | 9.89 | 99.69 |
| | 1.0 M NaOH at 75 °C | 100 | 68.02 | 99.76 |
| Oxidative Conditions | 3% H ₂ O ₂ | 11.08 | 16.72 | 87.98 |
| | 15% H ₂ O ₂ | 12.71 | 21.43 | 97.29 |
| | 3% H ₂ O ₂ at 75 °C | 100 | 21.21 | 89.23 |
| | 15% H ₂ O ₂ at 75 °C | 100 | 22.13 | 99.32 |
| Thermal Conditions | 6 h at 100 °C | - | 23.65 | 31.31 |
| | 24 h at 100 °C | - | 33.21 | 59.39 |
| Photolytic Conditions | 254 nm for 6 h | 10.88 | - | 1.81 |
| | 254 nm for 24 h | 12.91 | 13.99 | 76.09 |
| | 360 nm for 6 h | 0.13 | 19.76 | 68.76 |
| | 360 nm for 24 h | 2.12 | 39.81 | 69.64 |

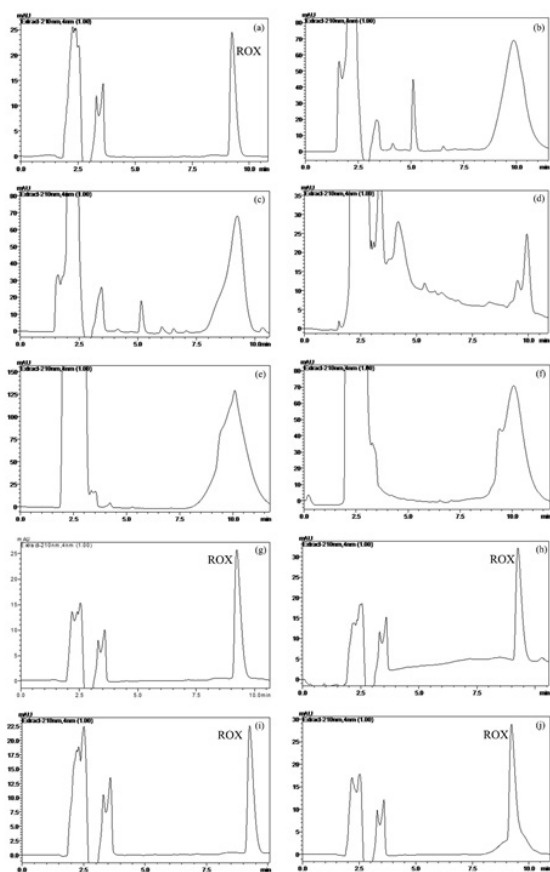


Figure 2. Chromatograms of (a):100 ppm ROX and degradation of ROX under (b): 1.0 M HCl, (c): 1.0 M HCl at 75 °C, (d): 1.0 M NaOH at 75 °C, (e): 3% H₂O₂ at 75 °C, (f): 15% H₂O₂ at 75 °C, (g): 6 h at 100 °C, (h): 24 h at 100 °C, (i): 254 nm for 24 h, (j): 360 nm for 24 h.

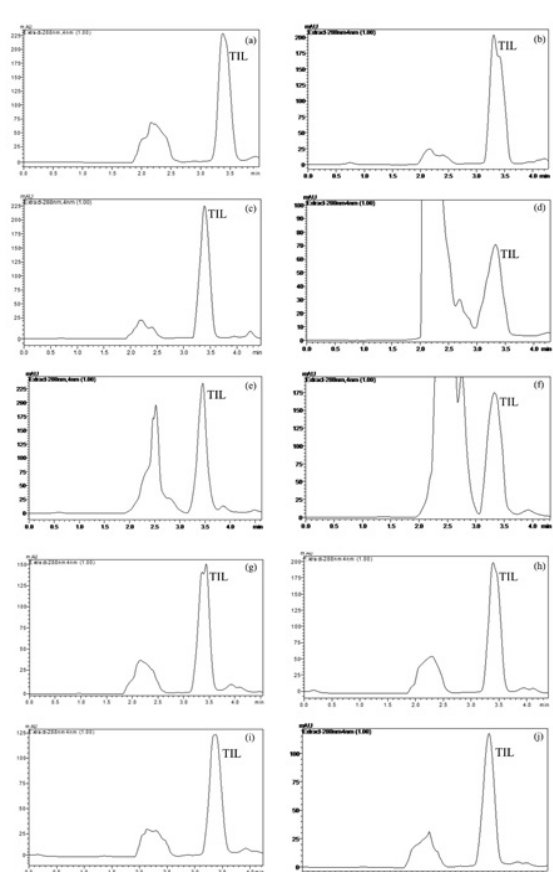


Figure 3. Chromatograms of (a):100 ppm TIL and degradation of TIL under (b): 1.0 M HCl, (c): 1.0 M HCl at 75 °C, (d): 1.0 M NaOH at 75 °C, (e): 3% H₂O₂ at 75 °C, (f): 15% H₂O₂ at 75 °C, (g): 6 h at 100 °C, (h): 24 h at 100 °C, (i): 254 nm for 24 h, (j): 360 nm for 24 h.

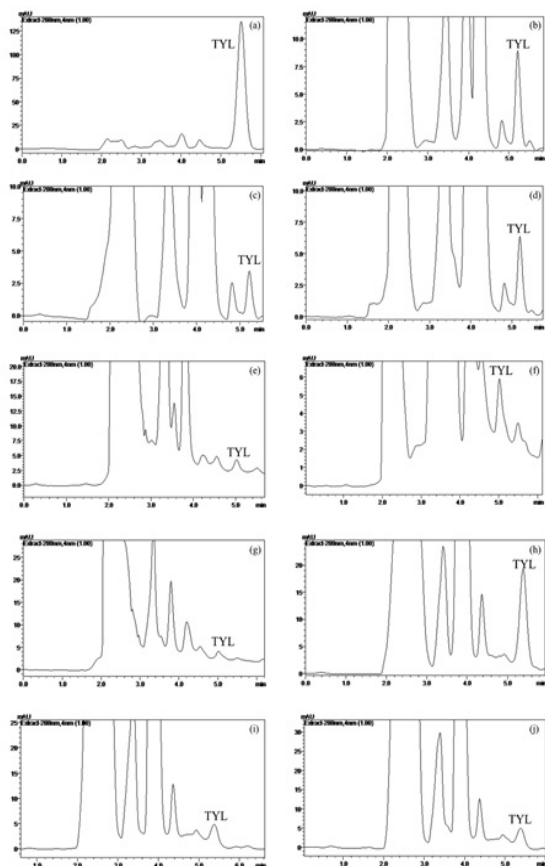


Figure 4. Chromatograms of (a):100 ppm TYL and degradation of TYL under (b): 1.0 M HCl, (c): 1.0 M HCl at 75 °C, (d): 1.0 M NaOH at 75 °C, (e): 3% H₂O₂ at 75 °C, (f): 15% H₂O₂ at 75 °C, (g): 6 h at 100 °C, (h): 24 h at 100 °C, (i): 254 nm for 24 h, (j): 360 nm for 24 h.

CONCLUSION

In this study, the degradation products of ROX, TIL and TYL were analyzed by subjecting them to various stress degradation conditions recommended by ICH. This study provides guidance for identifying instabilities of these drugs created in accordance with the recommendations of ICH guidelines. The information obtained as a result of degradation studies will help to stabilize these substances and facilitate the further study of their clinical applications.

References

1. Rensen B.H. Algal toxicity of antibacterial agents used in intensive farming. *Chemosphere* 40 (2000) 731–739.
2. Ying GG, He LY, Ying AJ, Zhang QQ, Liu YS, Zhao JL. China must reduce its antibiotic use. *Environmental Science & Technology* 51 (2017) 1072–1073.
3. Chun-Xiang L, Han J, Wang Y, Yong-Sheng Y, Xiao-Hui X, Jian-Ming P, *Analytica Chimica Acta* 653 (2009) 178–183.
4. Zhang H, Lu Y, Zhang G, Gao S, Sun D, Zhong Y. Bupivacaine-loaded biodegradable poly(lactic-co-glycolic) acid microspheres I. Optimization of the drug incorporation into the polymer matrix and modelling of drug release. *International Journal of Pharmaceutics* 351 (2008) 244–249.
5. Yang Y, Yuan L, Li J, Muhammad I, Cheng P, Xiao T, Zhang X. Preparation and evaluation of tilmicosin microspheres and lung-targeting studies in rabbits. *The Veterinary Journal* 246 (2019) 27–34.
6. Cheng J, Ye Q, Yang Z, Yang W, Zhou J, Cen K. Chlorella PY-ZU1 during tilmicosin removal from wastewater under 15% CO₂. *Journal of Hazardous Materials* 324 (2017) 414–419.
7. Paesen J, Cypers W, Busson R, Roets E, Hoogmartens J. Isolation of decomposition products of tylosin using liquid chromatography. *Journal of Chromatography A* 699 (1995) 99–106.
8. Daugherty AL, Mrsny RJ. Formulation and delivery issues for monoclonal antibody therapeutics. *Advanced Drug Delivery Reviews* 58 (2006) 686–706.
9. Filipe V, Hawe A, Carpenter JF, Jiskoot W. Analytical approaches to assess the degradation of therapeutic proteins. *Trac-Trends in Analytical Chemistry* 49 (2013) 118–125.
10. Tamizi E, Jouyban A. Forced degradation studies of biopharmaceuticals: Selection of stress conditions. *European Journal of Pharmaceutics and Biopharmaceutics* 98 (2016) 26–46.
11. Wahba MEK. Liquid chromatographic determination of roxithromycin: application to stability studies. *Journal of Chromatographic Science* 51 (2013) 44–52.
12. Prats C, Francesch R, Arboix M, Pérez B. Determination of tylosin residues in different animal tissues by high performance liquid chromatography. *Journal of Chromatography B* 766 (2001) 57–65.
13. Zhang Y, Pan Z, Ronga C, Shao Y, Wang Y, Yu K. Transformation of antibacterial agent roxithromycin in sodium hypochlorite disinfection process of different water matrices. *Separation and Purification Technology* 212 (2019) 528–535.
14. Şanlı S, Palabiyik IM, Şanlı N, Guzel-Seydim SB, Alsancak G. Optimization of the experimental conditions for macrolide antibiotics in high performance liquid chromatography by using response surface methodology and determination of tylosin in milk samples. *Journal of Analytical Chemistry* 66 (2011) 838–847.
15. ICH, *Stability Testing of New Drug Substances and Products (Q1A)*: International Conference on Harmonization, IFPMA, Geneva, 2000.

Some Serum Oxidative Parameters in Normoglycemic Rats: Vascular Endothelial Growth Factor (VEGF) Application

Kaan Kaltalioglu¹  Sule Coskun Cevher² 

¹Giresun University, Espiye Vocational School, Giresun, Turkey

²Gazi University, Department of Biology, Ankara, Turkey

ABSTRACT

VEGF has the positive effect on wound healing. In this study, the effect of VEGF application on some serum parameters during wound healing process were investigated. 36 female normoglycemic Wistar rats were used (200–250 g). Dorsolateral incisional wounds (length: 4 cm) were made on the two sides of the medulla spinalis in rats. They were divided into 3 groups: untreated group (n=12), chitosan group (n=12) and chitosan+VEGF group (n=12). The rats were sacrificed on the 3rd and 7th days of post wounding. NO_x, TBARs and RSH levels were determined spectrophotometrically in serum. Results were compared by one-way ANOVA (p<0.05). Serum TBARs levels both the chitosan treated group and the VEGF application group was found decreased when compared with untreated groups (3rd and 7th days) (p<0.05). Chitosan and VEGF application were effective increasing antioxidant capacity of serum on the 7th day. Serum NO_x levels decreased in the VEGF treated groups on 3rd and on 7th days (p<0.05). It can be considered that VEGF administration has a more positive systemic effect to eliminate increased oxidative damage in the serum of normoglycemic rats.

Keywords:

VEGF application; Chitosan; Wound healing; Oxidative stress; Antioxidant.

INTRODUCTION

Wound healing is essentially a science in which physiological and biochemical events occur at the highest level. The phases of normal wound healing are inflammation, proliferation and remodeling which cannot be completely separated from each other [1-5].

VEGF have different biological properties and bioavailability which consists of 6 isoforms in humans [6-8]. VEGF shows its effects via binding to tyrosine kinase receptors, VEGF receptor 1 and VEGF receptor 2. It has been known that hypoxia and also numerous cytokines and growth factors such as interleukin-6 (IL-6), IL-1 β , epidermal growth factor (EGF) and transforming growth factor- β (TGF- β) increase VEGF expression [9].

VEGF, which contains cysteine-cysteine bonds, and chitosan, which contains active -OH/-NH₂ groups [9,10], may influence the redox balance besides their contributions to wound healing process.

VEGF is produced by various cell types such as thrombocytes, fibroblasts, macrophages, smooth mus-

cle cells and neutrophils during wound healing process and it has receptors on endothelial cells and monocytes [9]. VEGF is a powerful mitogen factor for the endothelial cells of the lymph, arteries and veins, but lacks any mitogenic activity on other cells [9]. It has been known that VEGF synthesized in the wound bed peaked at 3-7 days and then gradually decreased at 7-14 days [9].

At very low concentrations (μ M), H₂O₂ induces VEGF-A expression. It has also been proven that oxidants such as H₂O₂ and NO promote VEGF synthesis, and N-Acetyl-L-cysteine, a GSH precursor, also inhibits angiogenesis by suppressing VEGF gene expression [11, 12].

It has been reported that the disruption of synthesis of VEGF and its mediator (NO) due to excessive oxidative stress in diabetes leads to the deterioration of wound healing phases [1-4, 13,14].

Chitosan is a polysaccharide consists of β -(1-4)-linked D-glucosamine and N-acetyl-D-glucosamine units. It is obtained commercially from chitin by dea-

Article History:

Received: 2019/11/17

Accepted: 2020/02/13

Online: 2020/03/26

Correspondence to: Sule Coskun Cevher,
Gazi University, Science Faculty, Biology
Department, 06500, Ankara, Turkey
E-Mail: sule@gazi.edu.tr
Phone: +90 312 202 1196
Fax: +90 312 202 1171

cetylation, which is in the cell walls of some bacteria and fungi. It has been shown that chitosan attracts inflammatory cells and growth factors released from them into the wound site in the early period of wound healing process [15]. Moreover, it has been reported that it has antioxidant effect thanks to its hydroxyl and amino groups [10].

On this basis, in our study, VEGF in chitosan gel were topically administered to the wound in normoglycemic rats. It was investigated how they affect the values of serum oxidative parameters such as TBARs and NOx levels, and RSH levels.

MATERIAL AND METHODS

Ethical approval for this study was obtained from Gazi University Local Ethics Committee for Animal Experiments (G.ET-10.117). Chitosan (C3646) and VEGF (Sigma V3638) were obtained from Sigma-Aldrich. 1% Lactic acid was added to 50 mL deionized water. 3 g chitosan was added to solution and stirred. After, 50 mL deionized water was added and mixed. Obtained gel was kept at room temperature overnight before the application. Finally, 417 ng VEGF was added to obtained chitosan gel (last concentration 7 ng/mL).

Animals

All of the rats were kept on standard rodent cages with appropriate amounts of rat food and water. Rats were kept with normal light-dark cycle (12:12 h) at room temperature (25 ± 2 °C).

Wound Model

The animals were anaesthetized with a combination of xylazine and ketamine intramuscularly. The dorsal section of rats was shaved an electric razor, and cleaned with 1% iodine tincture. 4 cm lengthy - incisional wound models were made on the two sides of medulla spinalis on the rats. 36 healthy normoglycemic rats were divided into 3 groups. There were 6 rats in each group: untreated group ($n = 12$), chitosan treated group ($n = 12$) and chitosan + VEGF group ($n = 12$) (7 ng/ml VEGF). Each group was divided into two in itself to be sacrificed on the 3rd and the 7th days.

Biochemical Analyses

Determination of TBARs levels

The TBARs levels of serum samples were analyzed according to Kurtel et al. [16]. The absorbance was read at 532 nm.

Determination of RSH levels

Plasma RSH was determined by spectrophotometric method [17]. The absorbance was read at 412 nm. RSH amount was determined assuming a molar absorption coefficient of 13.000 at 412 nm for 5-thio-2-nitrobenzoic acid (TNB).

Determination of NOx levels

The plasma NOx levels were measured using Griess reaction. Sodium nitrite and sodium nitrate solutions were used as standards [18].

Statistical Analysis

The data were given as the mean \pm standard deviation (SD). Mean values were compared by one-way ANOVA. The level of statistically significance was set at $P < 0.05$.

RESULTS

The obtained results are shown in Table 1.

Serum TBARs Level

Serum TBARs levels both the chitosan treated group and the VEGF application group was found decreased when compared with untreated groups (day 3 and day 7) ($p < 0.05$). The most significant reduction occurred in the chitosan group. It can be said that use of chitosan decreased lipid peroxidation in the rat serum. There weren't any significant alterations between the chitosan and VEGF treated group when compared with each other both 3 and 7 days ($p > 0.05$) (Fig 1).

Serum RSH Level

When the chitosan group were compared with the untreated group on the 7th day, the serum RSH levels of the chitosan group showed a statistically significant increase. In addition, when the VEGF treated group were compared with the untreated group, the serum RSH level

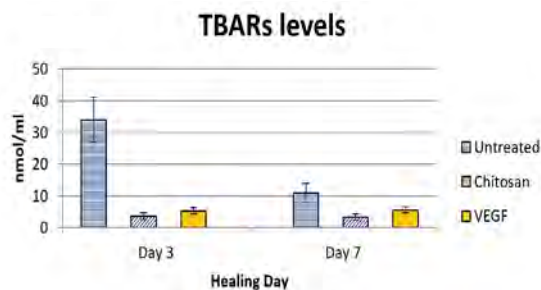


Figure 1. Serum TBARs levels.

Table 1 Serum TBARS, RSH and NOx levels in rats

| | TBARS level (nmol/ml) | RSH level (nmol/ml) | NOx level ($\mu\text{mol/l}$) |
|-------------------------|-----------------------------------|------------------------------------|----------------------------------|
| Untreated groups | | | |
| Day 3 | 33.99 \pm 7.73 ^{c,e} | 234.32 \pm 2.54 ^g | 9.51 \pm 1.94 |
| Day 7 | 10.98 \pm 3.03 ^{d,f,g} | 51.47 \pm 4.80 | 10.50 \pm 2.28 ^f |
| Chitosan treated groups | | | |
| Day 3 | 3.57 \pm 1.14 ^a | 223.15 \pm 2.78 ^g | 8.28 \pm 2.78 |
| Day 7 | 3.32 \pm 0.84 ^b | 393.55 \pm 9.20 ^b | 10.62 \pm 2.67 ^f |
| Chitosan + VEGF groups | | | |
| Day 3 | 5.23 \pm 1.85 ^{a,c} | 146.18 \pm 3.12 ^{a,c,g} | 4.22 \pm 0.74 ^{a,c} |
| Day 7 | 5.60 \pm 1.13 ^{b,d} | 248.78 \pm 5.40 ^{d,b} | 1.45 \pm 0.37 ^{b,d,g} |

^a $p < 0.05$ when compared to untreated group (day 3), ^b $p < 0.05$ when compared to untreated group (day 7), ^c $p < 0.05$ when compared to chitosan treated group (day 3), ^d $p < 0.05$ when compared to chitosan treated group (day 7), ^e $p < 0.05$ when compared to VEGF treated group (day 3), ^f $p < 0.05$ when compared to VEGF treated group (day 7), ^g $p < 0.05$ when compared to 3 and 7 day in the same group

of VEGF treated group showed a statistically significant increase on the 7th day. The serum RSH levels increased both chitosan treated group and VEGF group on the 7th day. Chitosan and VEGF application were effective increasing antioxidant capacity of serum on the 7th day (Fig 2).

Serum NOx Level

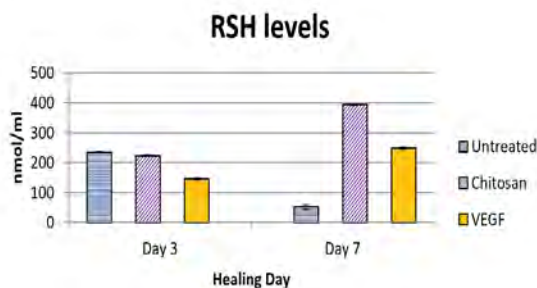
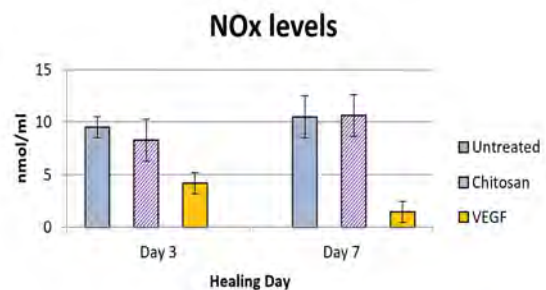
When VEGF treated groups were compared both the untreated groups and chitosan groups, NOx levels decreased in the VEGF treated groups on 3rd and on 7th days ($p < 0.05$). According to these results, it is seen that chitosan application did not change NOx levels when compared to untreated group. VEGF application decreased statistically significant in point of serum NOx levels ($p < 0.05$). VEGF administration decreased serum NO levels on both 3rd and 7th days of wound healing independent of chitosan. These results suggested that VEGF administration may have been effective by suppressing NOS enzyme levels in healthy rats (Fig 3).

DISCUSSION

There is information about that high levels of ROS are harmful by suppressing the synthesis of VEGF and its

mediator (NO) in the newly developed wound tissue and that micro-levels of ROS (H₂O₂ and NO) are beneficial by stimulating VEGF synthesis and signaling [19-21]. Although there is no infection in the wound, it has been understood that micro-levels of oxidants formed by respiratory burst are necessary to initiate various signal processes.

Jones et al. [22] reported that cysteine-cysteine bonds present in proteins received oxidative signals from the surrounding area by the conversion of thiols to disulfides. It has been indicated that the conversion of thiols to disulfides stimulates various molecular pathways in both mitochondria and cell nuclei by leading a change in protein-DNA and protein-protein interactions [23,24]. VEGF is also a growth factor that carries cysteine-cysteine bonds in its structure. Its synthesis and signaling are stimulated by oxidants such as H₂O₂ and NO and are inhibited by antioxidants such as GSH and N-acetyl cysteine (NAC) [21]. It has also been reported that inadequate VEGF synthesis is effective in disrupting the redox balance of the cell. Because it has been suggested that when VEGF is released, it initiates contradictory processes that show an antioxidant effect with mitochondrial Mn-SOD and an oxidant effect with NADPH oxidase [21]. VEGF may provide a balance between oxidant

**Figure 2.** Serum RSH levels.**Figure 3.** Serum NOx levels.

and antioxidants.

In the current study, firstly, when the chitosan and VEGF+chitosan groups were compared with the untreated group TBARS levels of the chitosan and VEGF+chitosan groups showed a decrease from the 3rd day to the 7th day. The most significant reduction occurred in the chitosan group. Both chitosan and VEGF are agents that affect the oxidation process in the media. It can be said that chitosan and VEGF showed an antioxidant effect in wound serum of healthy rats by reducing the lipid oxidation. Sönmez Çoban and Coşkun-Cevher [25] suggested that VEGF administration decreased serum TBARS levels compared to both diabetic control groups and chitosan treated diabetic groups. These results indicate that both chitosan and VEGF administration reduced lipid peroxidation in both normoglycemic and hyperglycemic rats.

When the chitosan group were compared with the untreated group on the 7th day, the serum RSH levels of the chitosan group showed a dramatically significant increase. In addition, when the VEGF treated group were compared with the untreated group, the serum RSH level of VEGF treated group showed a statistically significant increase on the 7th day. The serum RSH levels increased both chitosan treated group and VEGF group on the 7th day. Chitosan and VEGF application were effective increasing antioxidant capacity of serum on the 7th day (Table 1). On the 7th day corresponding to the proliferation phase of wound healing, serum RSH levels were increased. Both chitosan and VEGF administration increased serum antioxidant capacity. This increase was most prominent on day 7. Similarly, in the study performed by Sönmez Çoban and Coşkun-Cevher [25] in diabetic rats, increased serum RSH levels were detected on the 7th day of wound healing compared to diabetic control by VEGF application. In our study, it is thought that this effect may be due to the molecular structure of VEGF itself as an antioxidant.

According to our results, chitosan application did not change NOx levels when compared to untreated group. VEGF administration decreased serum NO levels on both 3rd and 7th days of wound healing independent of chitosan. These results suggested that VEGF administration may have been effective by suppressing NOS enzyme levels in healthy rats. Sönmez Çoban and Coşkun-Cevher [25] in their study, showed that both chitosan administration and exogenous VEGF administration increased serum NO levels in hyperglycemic rats. In contrast, we found that topical administration of VEGF reduced serum NO levels in normoglycemic rats. There is a relation between NO and VEGF in wound healing process; namely NO is one of the mediators of VEGF activity in terms of collagen deposition, nerve conduction, tissue oxygenation and restoration of en-

dothelial function [20,26].

CONCLUSION

It may be thought that the application may have an effect on reducing oxidative stress. Further studies are needed to determine the under various conditions in relation to VEGF applications, which have an important role in wound healing.

ACKNOWLEDGEMENT

The authors would like to thanks Gazi University Research fund (Project number: G.Ü. BAP 05/2011-01) for their financial supports.

References

1. Harding KG, Morris HL, Patel GK. Science, medicine and the future: Healing chronic wounds. *BMJ* 324 (2002) 160-163.
2. Fahey TJ, Sadaty A, Jones WG, Barbe A, Smoller B, Shires GT. Diabetes impairs the late inflammatory response to wound healing. *J Surg Res* 50 (1991) 308-313.
3. Lerman OZ, Galiano RD, Armour M, Levine JD, Gurtner, GC. Cellular dysfunction in the diabetic fibroblast. *Am J Pathol* 162 (2003) 303-312.
4. Komesu MC, Tanga MB, Buttros KR, Nakao C. Effects of acute diabetes on rat cutaneous wound healing. *Pathophysiology* 11 (2004) 63-67.
5. Lobmann R, Ambrosch A, Schultz G, Waldmann K, Schiweck S, Lehnert H. Expression of matrix-metalloproteinases and their inhibitors in the wound of diabetic and non-diabetic patients. *Diabetologia* 45 (2002) 1011-1016.
6. Ferrara N, Gerber HP, LeCouter J. The biology of VEGF and its receptors. *Nat Med* 9 (2003) 669-676.
7. Poltorak Z, Cohen T, Neufeld G. The VEGF splice variants: properties, receptors, and usage for the treatment of ischemic diseases. *Herz* 25 (2000) 126-129.
8. Tammela T, Enholm B, Alitalo K, Paavonen K. The biology of vascular endothelial growth factors. *Cardiovasc Res* 65 (2005) 550-563.
9. Ferrara N, Davis-Smith T. The biology of vascular endothelial growth factor. *Endocr Rev* 18 (1997) 4-25.
10. Sun T, Yao Q, Zhou D, Mao F. Antioxidant activity of N-carboxymethyl chitosan oligosaccharides. *Bioorg Med Chem Lett* 18 (2008) 5774-5776.
11. Sen CK, Khanna S, Babior BM, Hunt TK, Ellison EC, Roy S. Oxidant-induced vascular endothelial growth factor expression in human keratinocytes and cutaneous wound healing. *J Biol Chem* 277 (2002) 33284-33290.
12. Aktunc E, Ozacmak VH, Ozacmak HS, Barut F, Buyukates M, Kandemir O, Demircan N. N-acetyl cysteine promotes angiogenesis and clearance of free oxygen radicals, thus improving wound healing in an alloxan-induced diabetic mouse model of incisional wound. *Clin Exp Dermatol* 35(2010) 902-909.
13. Roy S, Khanna S, Sen CK. Redox regulation of the VEGF signaling path and tissue vascularization: Hydrogen peroxide the common link between physical exercise and cutaneous wound healing. *Free Radic Biol Med* 44 (2008) 180-192.

14. Fraisl P. Crosstalk between oxygen- and nitric oxide-dependent signaling pathways in angiogenesis. *Experimental Cell Research* 319 (2013) 1331–1339.
15. İnan ZDŞ. Deneysel Diyabetli Sıçanlarda Kitozanın Yara İyileşmesine Etkisinin İncelenmesi. Yüksek Lisans Tezi. Histoloji-Embriyoloji Abd. Sivas Cumhuriyet Üniversitesi Fen/Sağlık Bilimleri Enstitüsü (2009)
16. Kurtel H, Granger DN, Tso P, Grisham MB. Vulnerability of intestinal interstitial fluid to oxidant stress. *Am J Physiol* 262 (1992) G573-578.
17. Elmann GL. Tissue sulphydryl groups. *Arch Biochem Biophys* 82 (1959) 70-77.
18. Miranda KM, Espey MG, Wink DA. A rapid, simple spectrophotometric method for simultaneous detection of nitrate and nitrite. *Nitric Oxide* 5 (2001) 62-71.
19. Osman AE. Vasküler Endotelial Büyüme Faktörünün Diyabetik Yara İyileşmesi Üzerine Etkileri: Farelerde Deneysel Çalışmalar. Uzmanlık Tezi. Plastik Rekonstrüktif ve Estetik Cerrahi Abd. Dokuz Eylül Üniversitesi Tıp Fakültesi (2006)
20. Bao P, Kodra A, Tomic-Canic M, Golinko MS, Ehrlich HP, Brem H. The Role of Vascular Endothelial Growth Factor in Wound Healing. *Journal of Surgical Research* 153 (2008) 347–358.
21. Roy S, Khanna S, Nallu K, Hunt TK, Sen CK. Dermal wound healing is subject to redox control. *Mol Ther* 13 (2006) 211–220.
22. Jones DP, Go YM, Anderson CL, Ziegler TR, Kinkade JM, Kirilin WG. Cysteine/cystine couple is a newly recognized node in the circuitry for biologic redox signaling and control. *FASEB J* 18 (2004) 1246-1248.
23. Nathan C, Cunningham BA. Beyond oxidative stress: an immunologist's guide to reactive oxygen species. *Nature Reviews Immunology* 13 (2013) 349-361.
24. Reuter S, Gupta SC, Chaturvedi MM, Aggarwal BB. Oxidative stress, inflammation, and cancer: how are they linked?. *Free Radic Biol Med* 49 (2010) 1603–1616.
25. Sönmez Çoban V, Coşkun Cevher Ş. The Investigation of the Effect of Topical Vascular Endothelial Growth Factor (VEGF) Administration on Serum Oxidative Parameters in Diabetic Rats. *Gazi University Journal of Science* 29 (2016) 543-547.
26. Stojadinovic O, Kodra A, Golinko MS, Tomic-Canic M, Brem H. A novel, non-angiogenic mechanism of VEGF: Stimulation of keratinocyte and fibroblast migration. *Wound Repair Regen* 15 (2007) 30.

Microwave Assisted Green Synthesis of Ag/AgO Nanocatalyst as An Efficient OER Catalyst in Neutral Media

Gokhan Elmaci 

Adiyaman University, Department of Chemistry, Adiyaman, Turkey

ABSTRACT

The development of robust, stable and abundant materials that are operating under neutral conditions are of great importance for the electrocatalytic conversion of water to hydrogen using sunlight. Here, a robust and highly stable, silver oxide based electrocatalyst composite system for the efficient Oxygen Evolution Reaction (OER) was presented. The developed Ag/AgO composite catalyst with a small (10-15 nm) and homogenous particle size distribution was fabricated using microwave synthesis. In the neutral media, the Ag/AgO electrocatalyst achieved 1 mA cm⁻² current density at 600 mV overpotential, and exhibited a lower Tafel slope of 80 mV dec⁻¹ compared to MnOx-based catalysts in the range of 450–600 mV. These values are comparable to those of the promising catalysts such as Mn, Co, Ni oxide based systems in the neutral media. The results showed that the developed electrocatalyst system based on Ag/AgO composite could be used in multi-layer electrocatalyst system designs.

Keywords:

Silver nanoparticles; Microwave; Catalytic activity; Oxygen evolution reaction.

Article History:

Received: 2019/11/17

Accepted: 2019/12/17

Online: 2020/03/26

Correspondence to: Gokhan Elmaci,
Adiyaman University, Department of
Chemistry, Faculty of Arts and Sciences,
02040, Adiyaman, Turkey
E-Mail: gelmaci@adiyaman.edu.tr
Phone: +90 416 223 38 00/3667
Fax: +90 416 223 38 09

INTRODUCTION

In the next 50 years, there is an urgent need for the sustainable and clean alternative energy sources to meet the increasing energy demands. Among the alternative energy sources, hydrogen energy is one of the most promising candidates [1-3]. Water, as an inexpensive and mostly abundant at around the world, is the main source for the generation of the hydrogen; however, obtaining hydrogen from water is thermodynamically unfavorable and requires a high amount of energy [4]. For this reason, economic energy conversion systems are required for the production of hydrogen gas from water [5]. In this point, catalysts are considered as one of the most important parts of the energy transformation. Nevertheless, designing new sustainable catalysts, which can achieve energy conversions at low costs and improved in terms of shape, size and chemical composition, is a great criterion. Therefore, there has been a growing interest for the solution of this task [5-7].

In the last decades, nanomaterials have received much attention due to their unique physical, chemical, optical, magnetic, and electrical properties [8, 9]. Among these materials, precious metals such as Pd, Pt, Au and metal oxides; Ru₂O and Ir₂O are the inevitable part of the production of energy from water through its

splitting to H₂ and O₂ [10, 11].

However, their high costs and low abundances on the earth make handicap for their easy availability in the sustainable energy system [12, 13]. Regarding these disadvantages, there have been a long-term demand for the development of robust, inexpensive and highly efficient electrocatalyst systems for the energy applications. In this perspective, earth-abundant metals such as Ag, Co, and Ni are considered as more economic alternatives [14, 15]. Nevertheless, a little attention has been devoted to the preparation of electrocatalyst from silver nanocomposites so far [16]. As well as the preparation of the silver nanocomposites, their stabilities in the media where they take a role in the energy applications are of great importance [17, 18]. The nanocomposites may exhibit different characteristics owing to their unique structures and morphologies depending on their synthesis conditions [19]. Therefore, alternative approaches for the synthesis of silver nanocomposites are necessary and important as much as the application field where they take action.

In material synthesis, microwave technology (MT) is a promising alternative to the conventional methods depending on its superiority, especially in terms of spe-

ed, low consumption of chemicals and energy [20]. MT not only keeps the reaction media steady state but also; therefore, promotes uniform product formation [20, 21]. In this way, it also enhances the large-scale production of the advanced materials with the desired quality of interest. Recent studies showed that MT has also a significant role on the reaction kinetics, particle-size and morphology of the resulting products [22]. Due to these advantages, the MT has received an increasing attention in the synthesis of various materials such as metal oxides, carbon and precious metal based catalysts, peroxides and many mores [20-22]. In recent years, MT has also been facilitated in the fabrication of advanced materials, as well [23, 24].

Considering the above-mentioned advantages of MT, herein, we report the rapid, simple and highly reproducible synthesis of Ag/AgO nanoparticles via microwave irradiation. The as synthesized nanoparticles were used as an efficient OER electrocatalyst for water splitting reactions. The prepared Ag/AgO nanocatalysts showed excellent water splitting activity under neutral media conditions.

EXPERIMENTAL SECTION

Materials

Silver nitrate (AgNO_3), oleic acid, oleylamine, ethanol and 1-octanol were purchased from Merck and used as received

Synthesis of Ag/AgO nanoparticles

In a typical procedure, a mixture of oleic acid (40 ml v/v 1/1), 1-octanol and oleylamine along with 100 mg AgNO_3 was added into a 100 mL flask equipped with a stirring bar under nitrogen atmosphere. The as-prepared solution was refluxed under microwave irradiation according to the desired program (100 W, 110 °C, hold for 10 min). Subsequently, ethanol was added to the original reaction solution to precipitate Ag/AgO NPs. Ag/AgO NPs was filtered, washed with deionized water several times, and then dried at 65°C for 24 h.

Instrumentation

Powder X-ray diffraction patterns (XRD) of samples were collected using a Pan Analytical Empyrean instrument with $\text{Cu K}\alpha$ radiation ($\lambda=1.54056 \text{ \AA}$) from 3 to 70° (2θ) at a scanning rate of 2° min^{-1} . The morphologies and structure of the samples were examined by scanning electron microscopy (SEM, ZEISS Sigma 300) and Transmission electron microscopy (TEM, Hitachi HT 7700). Microwave-irradiated reactions were carried out with a microwave reactor (Discover SP, CEM, Matthews, NC, USA). The

electrochemical measurements were carried on Autolab workstation (PGSTAT204, Metrohm, Switzerland) using three-electrode system.

Electrochemical measurements

The electrocatalytic activity of Ag NPs was tested in deoxygenated 0.2 M phosphate (at pH 7) buffer solutions by using typical three electrode set-up similar to that reported by Joya et al. [16]. Ag/AgCl electrode (sat. KCl, +204 mV vs. NHE at 25°C) was used as the reference and a Pt plate as the counter electrode (1 cm^2). The potential, measured against an Ag/AgCl electrode, was converted to the potential versus the reversible hydrogen electrode (RHE) according to ($E_{\text{RHE}} = E_{\text{Ag/AgCl}} + 0.204 + 0.059 \text{ pH}$). The cyclic voltammogram (CV) and linear sweep voltammogram (LSV) were collected with a scan rate of 20 $\text{mV}\cdot\text{s}^{-1}$ between 0.2 V - 1.3 V vs. Ag/AgCl. Tafel slope was calculated by using the following equation, $\eta = a + b \log(j)$, where b is the Tafel slope, J is the current density, η is the overpotential value.

Preparation of the electrode

Ag/AgO NPs were obtained in solid form by simple centrifugation from ethanol. A homogeneous suspension for electrode was prepared using the solid Ag/AgO NPs by thoroughly mixing 10 mg of the catalyst with 10 μL of 0.5 wt % Nafion solution, 0.1mL of isopropanol. The electrode was prepared by drop-coating 11 μL of the prepared suspension onto a clean 1 cm^2 Fluorine doped Tin Oxide (FTO). The coated electrode was then dried at 60°C in oven for 30 min.

RESULTS AND DISCUSSION

Characterization of Ag/AgO thin film

The surface of the Ag nanoparticles may be oxidized during the synthesis or film preparation steps (Fig. 1). This change was observed in the XRD results of Ag NPs composed of thin films. The cubic phase of Ag can be indexed to the peaks at 38.1°, 44.3°, 64.4°, and 77.5° corresponding to (111), (200), (220), and (311) of Ag (JCPDS No. 04-0783)

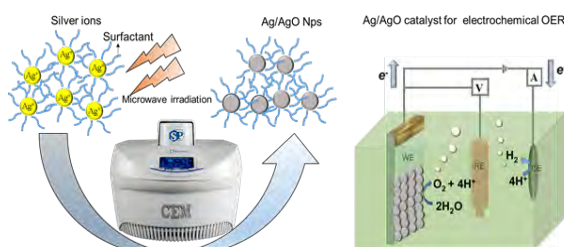


Figure 1. Schematic illustration of Ag/AgO NPs fabrication and its evolution as OER catalyst..

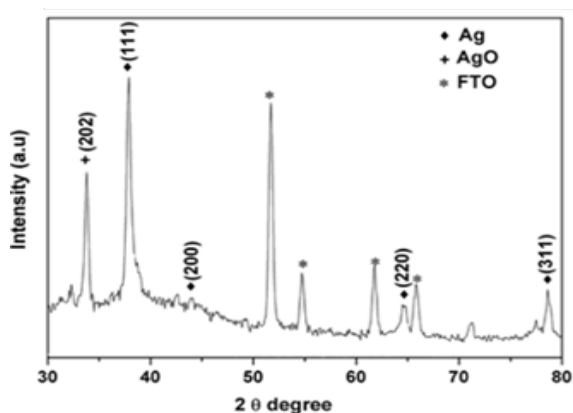


Figure 2. SX-ray diffraction (XRD) pattern for Ag NPs film on FTO glass.

[25], respectively. The peaks of AgO at 32.6° is consistent with the (202) of the standard card of AgO (JCPDS No. 84-1108) [26].

The morphological study was performed using SEM analysis. Fig. 3 shows SEM images of Ag/AgO nanoparticles. SEM image of the electrode surface displays that the coated film consists of Ag-AgO NPs with homogeneous particle size. Film formation on FTO with Ag/AgO catalyst was very smooth and homogeneous. This film preparation demonstrates that the applied procedure and method of application are suitable for the catalyst.

To further observe the morphology of Ag/AgO, the TEM analysis is showed in Fig 4. This image shows the spherical and plate-like morphologies of the NPs. The sizes of sphere-like particles were found to be in the range of 10-15 nm. Although the TEM analysis showed particle size of 10-15 nm, the nanoparticles in the thin film examined by SEM analysis were about 100 nm in size. The difference in particle size in TEM and SEM analysis may be due to agglomeration of Ag/AgO nanoparticles during film preparation.

Water oxidation performance of Ag/AgO NP type electrocatalyst

In recent years, in addition to metal oxides, plasmonic

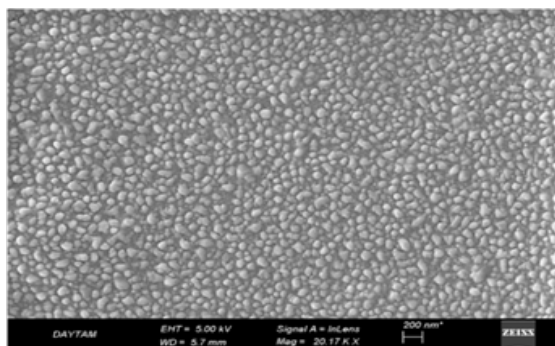


Figure 3. SEM image of Ag/AgO NPs film (top view).

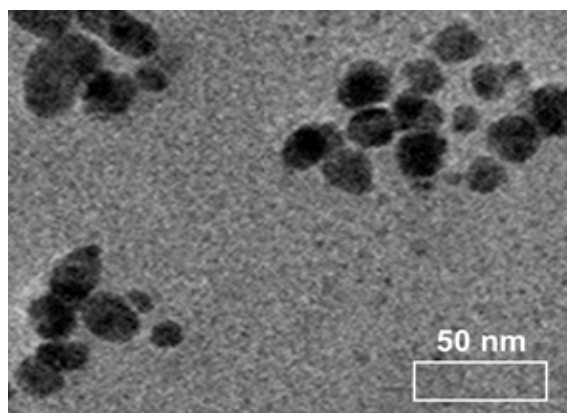


Figure 4. (TEM image of Ag/AgO NPs film).

nanostructures of noble metals (especially Ag and Au) have gained importance in the conversion of solar energy [27, 28]. The particle size, shape and morphology of these nanoparticles can be observed in the SPR band [29]. These physical properties also affect their catalytic activity and stability [28]. Monitoring of physical parameters for the design of electrocatalysts and photocatalysts plays a vital role in the catalyst production process [30]. Therefore, we investigated the electrocatalytic activity of Ag/AgO NPs, as “model” catalyst in water oxidation.

The synthesized Ag/AgO NPs was prepared as a film by 11 μ L drop-coating of homogeneous suspension onto FTO coated glass. Electrochemical water oxidation activity of Ag/AgO NPs electrodes was evaluated in deoxygenated 0.2 M phosphate (pH=7) buffer solutions similar to that reported by Joya et al. [16]. Fig. 5a (CV) shows a sharp increase at 1.3 V (E vs NHE) ($\eta \approx 480$ mV), associated with oxygen evolution from the electrode surface. In the neutral medium, Ag/AgO electrocatalyst achieved 1 mA cm^{-2} current density at 600 mV overpotential. At the same time, electrocatalyst exhibited a lower Tafel slope of 80 mV dec^{-1} , compared to MnOx-based catalysts which have operating overpotential in the range of 450–600 mV [31] (Fig. 5a inset). These overpotential value and lower Tafel slope of the Ag/AgO based composite electrocatalyst are comparable to the promising catalyst candidates such as Mn, Co, Ni oxide based systems in neutral medium [32]. In addition, Ag electrocatalysts are quite stable at a neutral pH compared to the loss of activa-

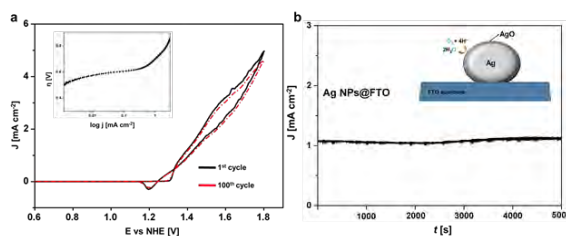


Figure 5. (a) Cyclic voltammetry (CV) (under a scanning rate of 20 mV s⁻¹), (b) Long-term chronoamperometry (LC) (in deoxygenated 0.2 M phosphate buffer) at a constant potential of 1.40 V (E vs NHE).

tion observed in Cyclic voltammetry and Long-term chronoamperometric measurements (Fig. 5a, 5b) in such oxide systems. As a result, electrocatalyst systems based on Ag/AgO composite can be used in multi-layer electrocatalyst system designs.

CONCLUSION

In summary, Ag/AgO based catalysts were prepared as homogenous spherical nanoparticles within 10 minutes using a microwave-assisted protocol. The as-synthesized Ag/AgO nanocomposites were fully characterized by means of X-ray diffraction (XRD), Scanning electron microscopy (SEM), Transmission electron microscopy (TEM) methods and their electrocatalytic activities were evaluated for OER in the neutral media. The electrocatalytic activity exhibited by the Ag/AgO composite was found to be comparable to the well-known metal oxide-based catalysts. This catalyst could be one of the promising catalysts in the energy conversion reactions.

ACKNOWLEDGEMENT

Author declares no conflicts of interest.

References

- Owusu PA, Asumadu-Sarkodie, S. A. Review of renewable energy sources, sustainability issues and climate change mitigation. *Cogent Engineering* 3 (2016) 1167990.
- de Vasconcelos BR, Lavoie JM. Recent advances in Power-to-X technology for the production of fuels and chemicals. *Frontiers in Chemistry* 7 (2019) 392.
- Tuller HL. Solar to fuels conversion technologies: a perspective. *Materials for Renewable and Sustainable Energy* 6 (2017) 3.
- Zeng K, Zhang, D. Recent progress in alkaline water electrolysis for hydrogen production and applications. *Progress in Energy and Combustion Science* 36 (2010) 307-326.
- Kothari R, Buddhi D, Sawhney, R. Comparison of environmental and economic aspects of various hydrogen production methods. *Renewable and Sustainable Energy Reviews* 12 (2008) 553-563.
- Leong G J, Schulze MC, Strand MB, Maloney D, Frisco S L, Dinh HN, Pivovar B, Richards RM, Shape-directed platinum nanoparticle synthesis: nanoscale design of novel catalysts. *Applied Organometallic Chemistry* 28 (2014) 1-17.
- Lauritsen JV, Kibsgaard J, Helveg S, Topsøe H, Clausen BS, Lægsgaard E, Besenbacher F. Size-dependent structure of MoS₂ nanocrystals. *Nature Nanotechnology* 2 (2007) 53-58.
- Kim BH, Hackett MJ, Park J, Hyeon T. Synthesis, characterization, and application of ultrasmall nanoparticles. *Chemistry of Materials* 26 (2013) 59-71.
- Ray PC. Size and shape dependent second order nonlinear optical properties of nanomaterials and their application in biological and chemical sensing. *Chemical Reviews* 110 (2010) 5332-5365.
- Hu C, Zhang L, Gong J. Recent progress of mechanism comprehension and design of electrocatalysts for alkaline water splitting. *Energy & Environmental Science* 12 (2019) 2620-2645.
- Jafari T, Moharreri E, Amin AS, Miao R, Song W, Suib SL. Photocatalytic water splitting the untamed dream: a review of recent advances. *Molecules* 21 (2016) 900.
- Tachibana Y, Vayssieres L, Durrant JR. Artificial photosynthesis for solar water-splitting. *Nature Photonics* 6 (2012) 511-518.
- Hisatomi T, Kubota J, Domen, K. Recent advances in semiconductors for photocatalytic and photoelectrochemical water splitting. *Chemical Society Reviews* 43 (2014) 7520-7535.
- Li L, Shao Q, Huang X. Amorphous oxide nanostructures for advanced electrocatalysis. *Chemistry A European Journal* 25 (2019) 1-19.
- Hu J, Zhang C, Meng X, Lin H, Hu C, Long, X, Yang, S. Hydrogen evolution electrocatalysis with binary-nonmetal transition metal compounds. *Journal of Materials Chemistry A* 5 (2017) 5995-6012.
- Joya KS, Ahmad Z, Joya YF, Garcia-Esparza AT, de Groot HJ. Efficient electrochemical water oxidation in neutral and near-neutral systems with a nanoscale silver-oxide catalyst. *Nanoscale* 8 (2016) 15033-15040.
- Cozzoli PD, Comparelli R, Fanizza E, Curri ML, Agostiano A, Laub D. Photocatalytic synthesis of silver nanoparticles stabilized by TiO₂ nanorods: A semiconductor/metal nanocomposite in homogeneous nonpolar solution. *Journal of the American Chemical Society* 126 (2004) 3868-3879.
- Dallas P, Sharma VK, Zboril R. Silver polymeric nanocomposites as advanced antimicrobial agents: classification, synthetic paths, applications, and perspectives. *Advances in Colloid and Interface Science* 166 (2011) 119-135.
- Camargo C, Satyanarayana KG, Wypych F. Nanocomposites: synthesis, structure, properties and new application opportunities. *Materials Research* 12 (2009) 1-39.
- Clark DE, Sutton WH. Microwave processing of materials. *Annual Review of Materials Science* 26 (1996) 299-331.
- Singh S, Gupta D, Jain V, Sharma AK. Microwave processing of materials and applications in manufacturing industries: a review. *Materials and Manufacturing Processes* 30 (2015) 1-29.
- Thostenson E, Chou TW. Microwave processing: fundamentals and applications. *Composites Part A: Applied Science and Manufacturing* 30 (1999) 1055-1071.
- Fan X, Guan J, Li Z, Mou F, Tong G, Wang W. One-pot low temperature solution synthesis, magnetic and microwave electromagnetic properties of single-crystal iron submicron cubes. *Journal of Materials Chemistry* 20 (2010) 1676-1682.
- Cao JM, Feng J, Deng SG, Chang X, Wang J, Liu JS, Lu P, Lu HX, Zheng MB, Zhang F. Microwave-assisted solid-state synthesis of hydroxyapatite nanorods at room temperature. *Journal of Materials Science* 40 (2005) 6311-6313.
- Han Y, Zheng J, Dong E. A novel nonenzymatic hydrogen peroxide sensor based on Ag-MnO₂-MWCNTs nanocomposites. *Electrochimica Acta* 90 (2013) 35-43.
- Yang H, Ren Y, Wang T, Wang C. Preparation and antibacterial activities of Ag/Ag⁺/Ag₃⁺ nanoparticle composites made by pomegranate (*Punica granatum*) rind extract. *Results in physics* 6 (2016) 299-304.
- Osterloh F. Inorganic nanostructures for photoelectrochemical and photocatalytic water splitting. *Chemical Society Reviews* 42 (2013) 2294-2320.
- Yi S, Zhang XB, Wulan BR, Yan JM, Jiang Q. Non-noble metals applied to solar water splitting. *Energy & Environmental Science* 11 (2018) 3128-3156.
- Jones MR, Osberg KD, Macfarlane RJ, Langille MR, Mirkin CA. Templated techniques for the synthesis and assembly of plasmonic nanostructures. *Chemical Reviews* 111 (2011) 3736-3827.
- Seh ZW, Kibsgaard J, Dickens CF, Chorkendorff I, Norskov JK,

- Jaramillo TF. Combining theory and experiment in electrocatalysis: Insights into materials design. *Science* 355 (2017) eaad4998.
31. Melder J, Kwong WL, Shevela D, Messinger J, Kurz P. Electrocatalytic water oxidation by MnOx /C: In situ catalyst formation, carbon substrate variations, and direct O₂/CO₂ monitoring by membrane-inlet mass spectrometry. *ChemSusChem* 10 (2017) 4491-4502.
32. Lee SY, Gonzalez-Flores D, Ohms J, Trost T, Dau H, Zaharieva I, Kurz P. Screen-printed calcium-birnessite electrodes for water oxidation at neutral pH and an "Electrochemical Harriman series". *ChemSusChem* 7 (2014) 3442-3451.

Hair Morphology Examination of Badger *Meles Meles* (L., 1758) in Turkey By Using Light And Scanning Electron Microscopes

Didem Atasever  Nahit Pamukoglu 

Kirikkale University, Department of Biology, Kirikkale, Turkey

ABSTRACT

In this study, the hairs of the badger (*Meles meles*) in the collection and various museums were examined and was tried to determine whether there were variations. For the morphological analysis of the guard hair samples taken from the middle part of the ridge, the guard hairs were examined by both light microscopy and scanning electron microscopy (SEM). The root of the guard hairs on the back and sides was dirty white, the body was brownish black and the tip was white. The length of the hairs on the back and sides was determined to be about 75 mm. It was determined that 21 of the samples had summer fur, the dorsal part had brown and transition tones had dark brown hairs, and 4 had winter fur, the dorsal part had grayish brown hairs and the ventral part had blackish light brown hairs. In addition, winter fur was found to be covered more frequently and with long guard hairs.

Keywords:

Badger; *Meles meles*; Hair morphology; Turkey

INTRODUCTION

One of the factors that ensure the survival of mammals in the face of environmental changes is that their bodies are covered with hair [1]. Mammals have adapted to various environments with changes in their furs, which consist of various types of hair including protection and under fur hairs.

Carnivores naturally have hairs in digestive organs and stools and their location show little or no change and which give some informations about analysis of nutritional habits in animal ecology, wildlife biology and nature management. For these reasons, the first hair morphology studies were carried out by Tupinier [2], Kondo and Watanabe [3] and Kondo and Nishiumi [4] by using guard hair to be used as a key in order to identify the species. Then in 2003 Western European mammals by examining the structure of the differences between the species in terms of hair morphology was detaily reviwed by Teerink [5].

In Turkey, some researches were investigated by using hair morphology to identify some species from different regions. For instance, Blackler [6] noted that the bottom of the bristles was whitish camel-haired and the rest was camel-haired. The researcher stated that approximately 1/3 of the hair length near the tip was whitish with a black band and about 5 mm in length,

and that fur gold was usually darker than camel hair (pale yellow) than long hairs.

Ognev [7] states that the maximum length of the guard hairs is about 50 mm in the middle of the rear; hair roots, dirty rusty straw white, black preterminal band, wider than winter fur and these bands started with mixed shades of cinnamon and the tip of the feathers, yellowish color and winter individuals less white color, snow in the abdomen rather sparse and bare skin in the abdomen and that the badger's summer fur is darker, blacker and more orange than winter fur.

Huş [8] and Erençin [9] claimed that the badger had hard thick hairs and the hairs on the abdomen were thin and sparse.

Turan [10] claimed that the guard hairs are long hard, the pile hairs are short and soft, the head and tail hairs are short and flat, the other parts are long and drooping, the skin is sparsely hairy enough to be seen in the abdomen.

Albayrak and Çoban [11] examined hair samples a total of 46 species belongs to Insectivora, Chiroptera, Lagomorpha, Rodentia, Carnivora and Artiodactyla orders morphologically. The researchers identified nine

Article History:

Received: 2019/11/22

Accepted: 2019/12/28

Online: 2020/03/26

Correspondence to: Nahit Pamukoglu,

Kirikkale University, Department of

Biology, Yahsiyan, Kirikkale, Turkey

E-Mail: pamukoglu2003@yahoo.com

Phone: +90 535 783 84 99

Fax: +90 318 357 24 61

different types of guard hairs: vase, cone, fringed tail, mosaic, wavy serrated, wedge, irregular V, baklava and diamond pattern.

Özen and Uluçay [12] stated that the hairs on the dorsal part of all badger samples were longer. The researchers mentioned that the hairs were lying down in the direction of the ground. They claimed that the basal parts of the dorsal hair were white, the middle parts were mostly black and sometimes brown, and the most extreme parts were white.

Baydemir et al. [13] stated that general coloration of the guard hair is composed of three colours; black, rufous brown and creamy white. The structure of the hair scale was flattened imbricate and irregular crenate coronal at the base, shaft and the tip.

Pamukoğlu [14] found that the structure and some properties of the badger hair are different in terms of morphology and size when compared with other carnivore species. The researcher claimed that other carnivores were as short as hairy fur (skunk, weasel, otter and sea otter) and long haired fur (such as voracious animal and bear). The researcher also noted that some parts of badger fur are different from other carnivore species because of their coarse, sparse and heterogeneous appearance and having both short and long hair structure.

Pamukoğlu and Albayrak [15] stated that guard hairs are denser and longer in winter fur. Pamukoğlu and Tunçer [16] claimed that in a badger sample obtained from Çanakale province, the hairs in the fur were short and the length of the guard hairs was approximately 45 and 60 mm.

Demirbaş [17] found that the structure of the hair scale type was found to be “mosaic” at the proximal of the shaft, “elongate petal” at the distal of the shaft, “streaked” at the proximal of the shield, and “regular wave” at the distal of the shield. It was determined that there were not any variations in terms of hair morphology among the three analysed regions of Turkish hare populations.

The main purpose of this study is to determine whether the badger, *Meles meles* shows the hair variation by using with light microscope and SEM and do the sybolytic comparison studies, the hair morphology of *Meles meles* with previous studies.

MATERIAL AND METHODS

For morphological analysis of guard hair samples taken from the middle part of the dorsum, the hairs were examined by both light and SEM [18, 19]. Hair samples were placed in a mixture of acetone, distilled acetone and dis-

tilled water (1: 1 ratio) for 30 minutes and finally in distilled water for 10 minutes and dried. Morphological structures of the hairs were examined with light microscope (Leica DM5000 B, Leica Microsystems Europe, Wetzlar, Germany) and SEM (JEOL, JSM 5600, Tokyo, Japan). Before SEM analysis, hair samples were stabilized on SEM stamps and were coated gold. Then images were taken in different parts of hair samples by both microscopes with different magnifications values.

RESULTS

Hair Structure in Badger

Microscopic examination of the hair color revealed that the two colors along the hair were transitions (shades of black and white). The hair is dominated by the white color from the root to the upper body, and after the upper body dark (black-brown) transition has been observed. The dark portion dominates the upper body and the lower region of the tip, and the color of the tip is observed to be white as you move to the upper part of the tip (Fig. 1).

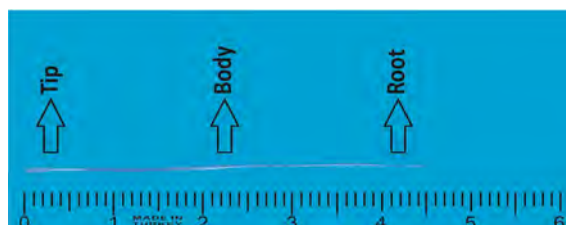


Figure 1. General structure of a guard hair examined in badger.

Different color regions were determined in the hair. The guard hairs were determined to have a 32-35 mm off-white or straw-whitish basal portion followed by a 21-23 mm dark black band and a 9-11 mm long white or slightly grayish white tip. It was found that the base of the hairs on the side of the body was more dense. It has been observed that in adult individuals, the amount of graying increases in protection hairs compared to young individuals. The macroscopic examination of the hair in the badger revealed that the tip of the hair was white, the body was blackish dark brown, and the body to the root was white. In the adult samples, the increase in the white area of the protection hair was also observed. It has also been found that the hairs on the side form a fringed image. This can be used to distinguish adult individuals from young and offspring.

Macroscopic Examination of Hair in Badger

In microscopic examination of the hair sample taken from the dorsal part of the badger, the length of the hair from the tip to the lower tip point (white part) is 0.5 cm, from the bottom point of the upper body (dark part) is

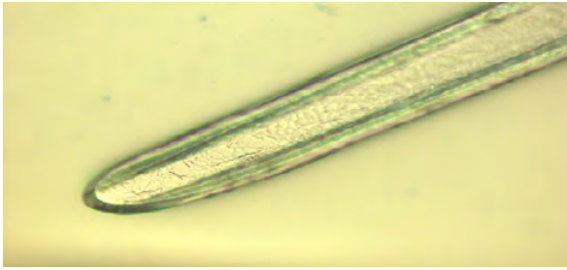


Figure 2. Examination of the tip of the hair at 50 μm under a light microscope.

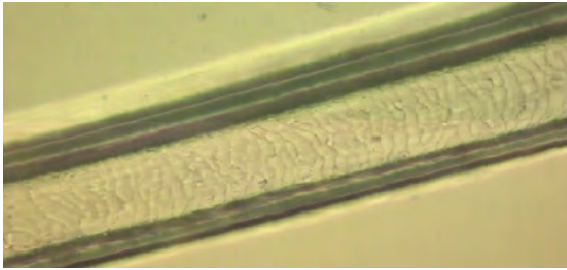


Figure 3. Examination of the body of the hair under a light microscope at 50 μm .

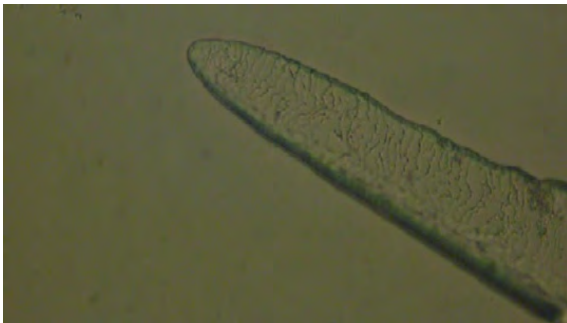


Figure 4. Examination of the root of the hair with a light microscope.

1 cm, from the upper body to the root (over skin) (white part) is 3 cm long. In other words, from the tip of the hair to the root (over skin), the length of the hair was found to be 4.5 cm. Other protection hairs have been found to be about these dimensions.

Examination of The Hair in The Badger By Using Light Microscope

The light microscope examination of the hair showed thinning and fluctuations in the rough structure along the hair (Fig. 2, Fig. 3, Fig. 4).

Investigation of Hair in Badger with SEM

The root, the body and the tip of the hair were examined with SEM and images which were taken were illustrated in Fig. 5, Fig. 6 and Fig. 7. In SEM of the badger's guard hair, the examined hair grew by folding from the root and the width of the hair was narrower than the body at the tip and root. At X500 magnification, thickening was observed as the width of the hair at the root portion

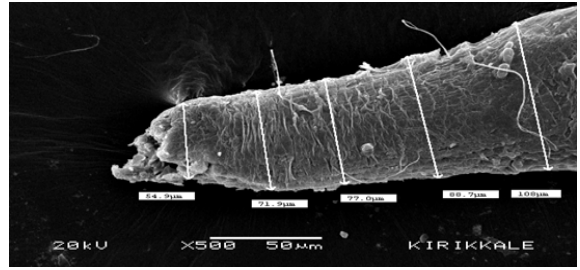


Figure 5. Thickening of the guard hair examined with SEM from the root to the body.

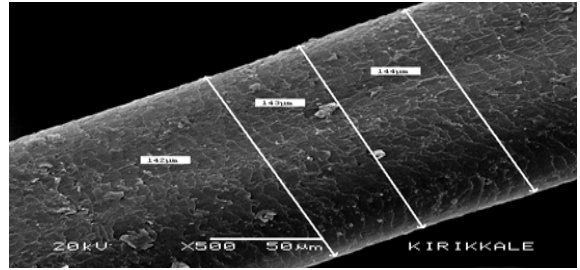


Figure 6. Continuous thickening of the body of the guard hair examined with SEM.

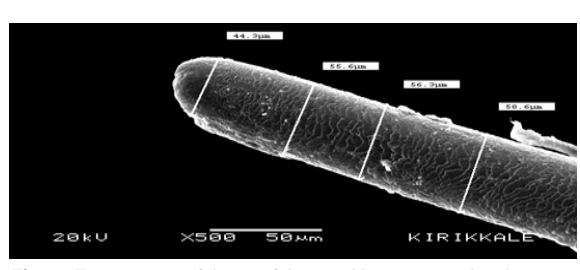


Figure 7. Narrowing of the tip of the guard hair examined with SEM.

of the hair progressed towards the body measuring 54.9 μm 71.9 μm -77.0 μm -88.7 μm -108 μm . These thickening continued in the body as 142 143m-143 μm -144 μm . But unlike the root and body as it reaches the tip of the hair, it is measured in the size of 58.6 μm -56.3 μm -55.6 μm -44.3 μm as it moves towards the of the hair.

Profile of Guard Hair Examined with SEM

The pieces in the cuticular layer at the tip of the hair are small and consist of smaller pieces than the root and the body (Fig. 8). The width of the pieces on the cuticular layer is higher than their length. In other words, the hair segments according to their longitudinal position are "transverse".

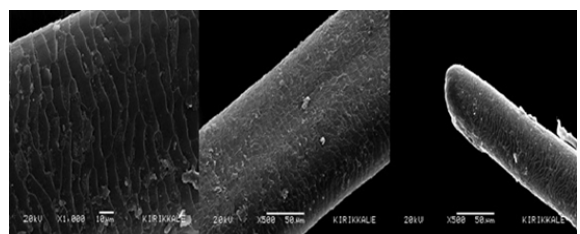


Figure 8. Thickening of the guard hair examined with SEM from the root to the body.

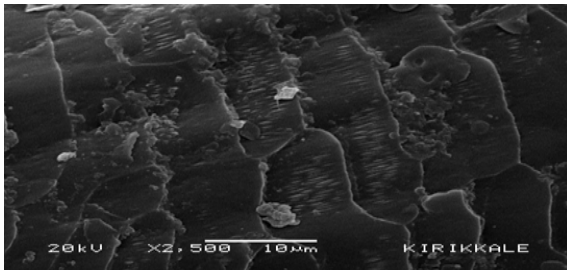


Figure 9. Diamond crown pattern view of the cuticular structure of the root portion of the hair examined with SEM.

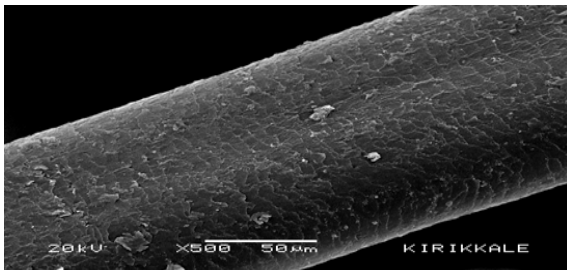


Figure 10. Diamond crown pattern of cuticular structure of the body part of hair examined with SEM.

It was seen that the cuticle structure was the diamond crown pattern (Fig. 9, Fig. 10). In addition, irregular wave pattern was found at the tip (Fig. 11).

The part margin structure on the root is “smooth”. In other words, the margin is protruding. The part margin structure on the body and is “wrinkled” (Fig. 12, Fig. 13, Fig. 14). So there are small indentations on the margin, and usually the distance between them is close.

The distance between the part margin is “close” pattern on the root, the body and the tip on a quantity basis.

The Structure of Medullar in Cross Section of Guard Hair Examined in SEM.

The medulla of the badger hair is more difficult to visualize than the cuticular structure. The medullary structure was examined by taking a cross section from the shield which is the thickest part of the hair (Fig. 15).

Guard Hair Deformations Examined in SEM

In some adult hair samples, SEM showed some deformed regions (Fig. 16, Fig. 17). Deformation was generally encountered in the tip and body parts of the hair and the body parts of hair was manifested in the form of tearing and irregular thickening-thinning, while the tip was directed towards breaking and bifurcation.

DISCUSSION AND CONCLUSION

It was found that the features indicated by some research-

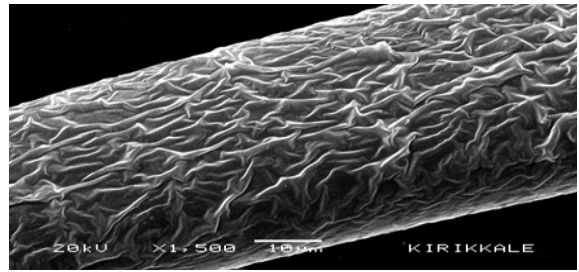


Figure 11. Irregular wave pattern of the cuticular structure of the tip of the hair examined with SEM.

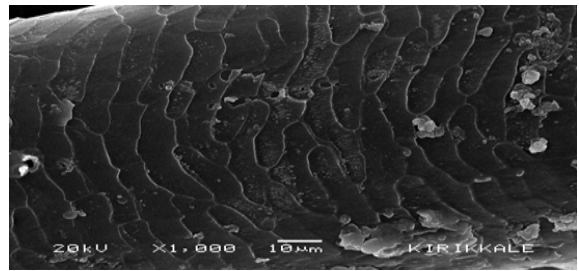


Figure 12. Smooth structure of the part margin of the root portion of the hair examined with SEM.

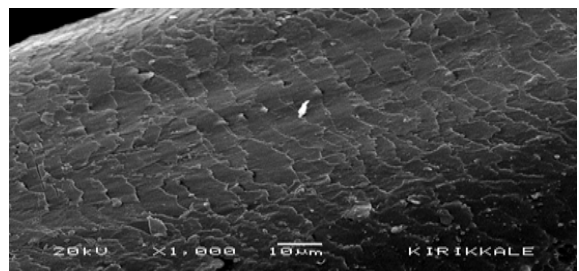


Figure 13. Wrinkled structure of the part margin of the body part of the hair examined with SEM.

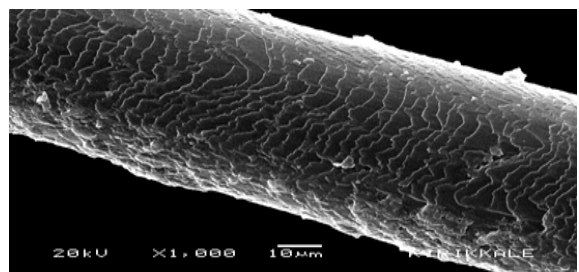


Figure 14. Wrinkled structure of the piece margin of the tip of the hair examined with SEM.

ers for instance Miller [20] and Ognev [7] almost coincided with our samples. In addition to the characteristics of Ognev [7], it was observed that the fur had longer hairs in the adult individuals among our samples and the age-related graying increased. As Huş [8, 21] stated, the hairs on the abdomen were thin and sparse and in addition, bare skin was seen due to sparse hairs. As Erençin [9] stated, our specimens were found to have frequent and hard hairs. Turan [10] stated that the long and drooping hairs on the side appeared as an age-related variation in our samples. Pamukoğlu [14], Özen and Uluçay [12], Pamukoğlu and Albayrak [15] were found to be similar to

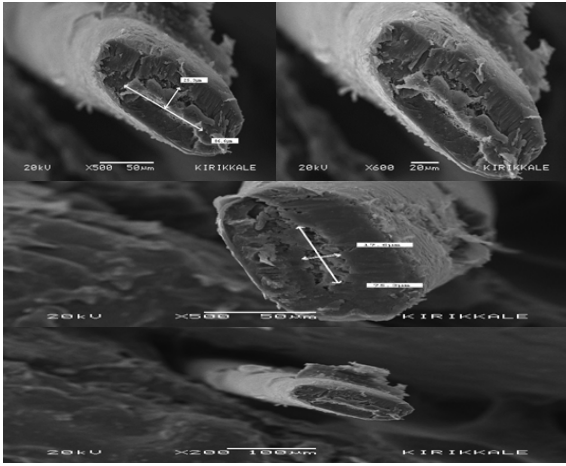


Figure 15. Medullary structure of hair examined with SEM.

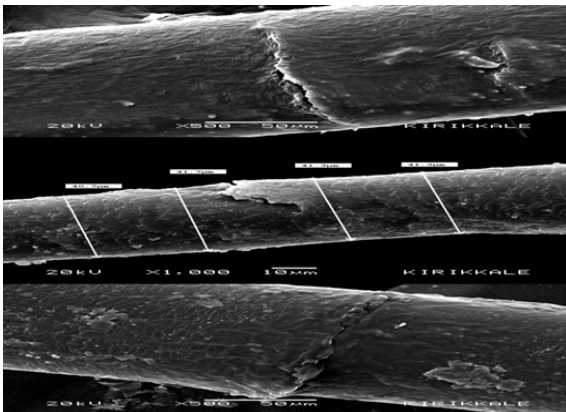


Figure 16. Bifurcation and fracture deformation of the tip of the hair.

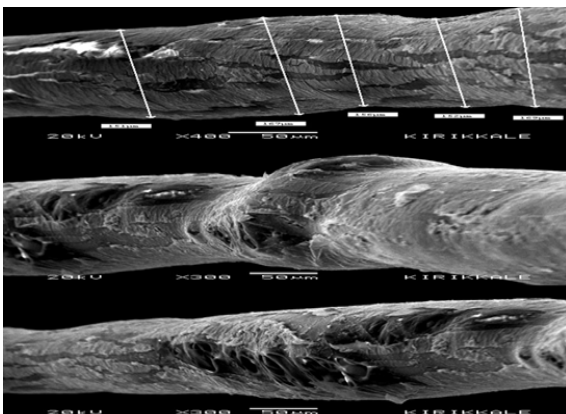


Figure 17. Tearing and irregular thickening-thinning deformation on the body part of the hair.

the results of our research.

The root of the guard hairs on the back and sides was dirty white, the body was brownish black and the tip was white. In particular, the hairs on the back and sides were found to be approximately 75 mm long. It was found that 21 of the samples had summer fur, the dorsal part consisted of brown and transitional hairs, the ventral part consisted of dark brown hairs, 4 of them had winter fur and the dorsal part had grayish color and the ventral part had blackish light

brown tone. Winter fur was more often covered with long guard hairs.

It was observed that the part pattern was the diamond crown pattern as the cuticles in the protection bristles examined in the scanning electron microscope (SEM). In addition, irregular wave pattern was found at the tip.

It has been determined that the age of the individual, the decrease in the amount of keratin substance, climatic change and nutrition can cause deformations in the hair structure, and these deformations may occur in the form of tearing in the body of hair and bifurcation by breaking at the tip of hair.

ACKNOWLEDGEMENT

This study is a part of Didem ATASEVER's Master Thesis. We would like to thank Prof. Dr. Dinçer GÜLEN from Istanbul University Science Faculty and Asst. Prof. Dr. Oya ÖZULUĞ, who is responsible for the Zoology Museum of Biology Department and Prof. Dr. Tuğrul MOL, Istanbul University, Faculty of Forestry.

References

1. Kondo K. The Diversity of Mammalian Pelage. J. Fac. Agr. Hokkaido Univ., 2000;70 (1):9-17.
2. Tupinier Y. Morphologie des poils de Chiropteres d'Europe occidentale par etude du microscope electronique à balayage. Rev. Suisse Zool. 1973;80:635-53.
3. Kondo K, Watanabe F. The Identification to the hair Japanese Insectivora. 81st. Annual Meeting of Japanese Society of Zootechnical Science, 1989;85.
4. Kondo K, Nishiumi, T. The pelage development in young mink (*Mustela vison*). J. Fac. Agr. Hokkaido Univ. 1991;64 :247-255.
5. Teerink BJ. Hair of West European Mammals: Atlas And Identification Key. Cambridge University Press. First paperback edition 2003.
6. Blackler W. On Two New Carnivores From Asia Minor. Ann. Mag. Nat. Hist. 1916;18 (VIII):73 -77.
7. Ognev SI. Mammals of Eastern Europe and Northern Asia. Vol. 2, Carnivora, Fissipedia. Moscow, 1931.
8. Huş S. Av Hayvanları ve Avcılık, Kutulmuş Matbaası. İstanbul, 1967.
9. Erençin Z. Av Hayvanları ve Av. Ankara Üniversitesi Veteriner Fakültesi Yayınları. Ankara, 1977.
10. Turan N. Türkiye'nin Av ve Yaban Hayvanları (Memeliler). Ongun Matbaacılık Sanayii Ankara, 1984.
11. Albayrak İ, Çoban N. Hair Morphology Of Some Mammalian Species in Turkey. Communication Fas. Des. Scien. De L Univ. D-Ankara Series C, 1997; 15:21-39.
12. Özen AS, Uluçay İ. Kütahya İli Meles meles Linnaeus, 1758 (Mammalia: Carnivora)'in Bazı Ekolojik, Biyolojik ve Taksonomik Özellikleri. Dumlupınar Üniversitesi Fen Bilimleri Enstitüsü Dergisi, Kütahya, 2010;21:9-20.
13. Baydemir NA, Demirbaş Y, Ilker A. Contributions To The Biology Of Wolves (Mammalia: Carnivora) In Turkey. International Journal Natural And Engineering Sciences 2011;5 (2): 33 -36.
14. Pamukoğlu N. "Porsuk Meles meles (L., 1758)'de Kıl Morfolojisinin

- İncelenmesi (Mammalia: Carnivora)". 22. Ulusal Biyoloji Kongresi, 23-27 Haziran 2014, Eskişehir Osmangazi Üniversitesi, Eskişehir, Türkiye. HB – Hayvan Biyolojisi (Sözlü Sunum), 2014;HB-S2-14:237.
15. Pamukoğlu N, Albayrak İ. The Taxonomy and Ecology of Meles Meles (L., 1758) in Western Turkey. Hacettepe J. Biol. & Chem., 2014;42(4):451-458.
 16. Pamukoğlu N, Tunçer S. Çanakkale İli Kepez Bölgesinde Porsuk Meles Meles (L., 1758) Üzerine Bir Araştırma. Tabiat ve İnsan Derg. 2014;3(3):17-21
 17. Demirbaş Y. Studies on the Hair Characteristics of European Hare, Lepus europaeus (Lagomorpha: Leporidae) in Turkey. Pakistan J. Zool., 2014;46(2):371-376.
 18. Day MG. Identification of hair and feather remains in the gut and faeces stoats and weasels. J.Zool., London, 1966;155:458-497.
 19. Hayat MA. Basic electron microscopy techniques. Van Nostrand Reinhold Company, New York, 1972.
 20. Miller GS. Catalogue Of The Mammals Of Western Europe. British Museum Pub., London, 1912.
 21. Huş S. Av Hayvanları ve Avcılık. İ.Ü.Orman Fakültesi Yayınları No: 1971. O.F. Yayın No: 202. İkinci Baskı. Kutulmuş Matbaası. İstanbul, 1974.

Inventory of Large Mammal Species in the Ilgaz Mountains (Cankiri): A Major Ecological Corridor in Anatolia

Burak Akbaba¹  Safak Bulut² 

¹Hacettepe University, Department of Biology, Ankara, Turkey

²Hitit University, Department of Molecular Biology and Genetics, Corum, Turkey

ABSTRACT

In order to understand the processes engendered by different faunal elements in natural systems, and to plan how such systems should be managed and conserved, it is essential to start by determining the presence of those faunal elements, even large mammals. The entire range of North Anatolian Mountains provides suitable sheltering and feeding habitats for large mammals. The region stretching between Koroğlu Mountains (west) and Ilgaz Mountains (east) is one of the most important Anatolia's wildlife corridors. We located and identified the species of large mammals in the Ilgaz Mountains, as well as specific habitats used by them. Field studies carried out in this region during April–August 2017 resulted in 180 records of nine different species of large mammals: *Lepus europaeus*, *Ursus arctos*, *Canis lupus*, *Vulpes vulpes*, *Lynx lynx*, *Meles meles*, *Sus scrofa*, *Cervus elaphus* and *Capreolus capreolus*. To obtain those records took 621 days of studying with camera traps. Among those species, European hare was the most frequently recorded herbivore (101), and brown bear was the most frequently recorded carnivore (19). Both hare and roe deer displayed clustered distribution patterns in the region. The analysis of our records showed that lynx, boar, and fox were strictly nocturnal; whereas hare and wolf were predominantly nocturnal. We also obtained records of the cubs of many large mammal species (bear, lynx, boar, red deer, roe deer) although we did not encounter any large mammal nests during the study.

Keywords:

Mammal, Camera trap, Çankırı, Ilgaz, Anatolia.

INTRODUCTION

Mammal species with a weight of over one kilogram are known as large mammals [1]. In most ecosystems, species of large mammals living on land play prominent roles. Among these, large herbivores act as considerable modifiers of primary production, as well as nutrient cycles and soil properties, and even regimes of wildfires and bushfires [2]. Likewise, large carnivores play a major part in shaping the ecosystems they live in, by directly and indirectly effecting the species they prey on [3, 4]. Home range sizes of large mammal species are relatively bigger than those of other vertebrates, and thus they require large, uninterrupted ecosystems for feeding and breeding [5]. They are also known to be very sensitive to disturbance, and show considerable intolerance against it [6]. In Anatolia, many of the ecosystems that large mammals may find favourable have either become fragmented, or they are completely destroyed as a result of human activities – a serious threat to the continuity of large mammal populations. Identifying

the presence of different species in a given area and determining the habitats preferred by large mammals were the two key precautions in investigating the effects of habitat fragmentation and producing alternative solutions for the conservation of species [7].

As pointed out by Can and Togan [8], there was considerable lack of information on large mammal species living in Turkey, and there were no reliable systematic field surveys for most of them. This statement still remained valid for the majority of large mammal species in 2017. Therefore, it is clearly necessary to conduct more studies on large mammal in different parts of Anatolia for the purpose of protecting their habitats and the species themselves.

North Anatolian Mountains start with Koroğlu Mountains in the west and continue with Ilgaz Mountains towards the east, constituting a transition zone between the geographic regions of Central Anatolia

Article History:

Received: 2019/12/26

Accepted: 2020/02/13

Online: 2020/03/26

Correspondence to: Burak Akbaba,
Hacettepe University, Department of
Biology, 06800, Ankara, TURKEY
E-Mail: akbabab@hacettepe.edu.tr
Phone: +90 533 357 32 31

and Western Black Sea, and thus is a very important location in terms of biological diversity. Forests extending from the Çamlidere-Gerede border towards Çankırı province are thought to be of great importance as an ecological corridor. Ilgaz Mountains are a notable part of this corridor, as they still contain habitats that are not fragmented. The region also hosts an adequate vegetation cover, which provides shelter and food for large mammals, while also supporting the local and long-distance movements of these species between the Northwest and Northeast Anatolia. Preservation of such transition zones is crucial for the presence of large mammals in Anatolia.

We demonstrated the outcomes of our study that focused on determining the inventory of large mammal species in the Ilgaz Mountains. The number of records and the daily activity patterns of spotted species were all based on camera trap records. With these results, we aimed to provide scientific data and insight for future conservation efforts on the large mammals in the region, and to support feasible management plans involving the area.

MATERIALS AND METHODS

Study Area

We carried out our study in a part of Ilgaz Mountains in northern Turkey (coordinates: 41.016198°-32.916474°, 40.844273°-33.100230°, 41.048360°-34.052563°, 41.138825°-33.785055°, Fig. 1).

Ilgaz Mountains define a wide geography, stretching between and beyond the borders of Kastamonu and Çankırı provinces. This study covered different parts around the Çankırı province. Ilgaz Mountains lie in the second row of North Anatolian Mountains, along the west-east plane. Il-

gaz Mountains reach 2587 metres at the peak, and our study was carried out at 1000-2500 metres of altitude. Biogeographically, the mountains extend into two different floristic regions: the Mediterranean and the Euro-Siberian phytogeographical regions. The region has a dominant forest vegetation, which contains communities of *Pinus sylvestris* L., *Pinus nigra subsp. pallasiana* (Lamb.) Holmboe, and *Abies nordmanniana subsp. equitrojani* (Asc. & Sint. ex Boiss.) Coode & Cullen. Ilgaz Mountains form a transition zone between the geographic regions of Central Anatolia and Western Black Sea, therefore having a climate influenced by both regions' typical characteristics. The summers are dry and cool, with snowy and rainy winters. The study area (along the southern slopes of the mountains) is dominated by an atypical Mediterranean climate, with extreme colds and limited rainfall [9, 10].

A section within the study area (approx. 1088.61 ha; 337.75 ha of which is within the borders of Çankırı province) was declared a "Ilgaz Dağı National Park" in 1976 [11].

Camera Trapping

In order to determine and identify the large mammal fauna, we carried out camera trap surveys between April 2017 and August 2017. We used of five cameras, all of which were passive infrared (Keepguard Wildlife Cameras, Keepway Industrial, Asia Co., Ltd). Based on interviews previously conducted with the locals living in the area, we targeted large mammal species belonging to the orders of Lagomorpha, Carnivora, and Cetartiodactyla: European hare (*Lepus europaeus* Pallas, 1778), brown bear (*Ursus arctos* L. 1758), wolf (*Canis lupus* L. 1758), golden jackal (*Canis aureus* L. 1758), red fox (*Vulpes vulpes* L. 1758), Eurasian lynx (*Lynx lynx* L. 1758), wild cat (*Felis silvestris* Schreber, 1777), European badger (*Meles meles* L. 1758), European pine marten (*Martes martes* L. 1758) and/or beech marten (*Martes foina* Erxleben, 1777), wild boar (*Sus scrofa* L. 1758), red deer (*Cervus elaphus* L. 1758), and roe deer (*Capreolus capreolus* L. 1758).

Trap spacing was known to have a significant effect in density studies [12]. The distances between camera traps have to be decided according to both the target species and the characteristics of the study area. In relative abundance studies that rely on presence-absence data, maximizing the possibility of photographing all species in the area is the main purpose, but camera spacing seemed to have little effect on the successful documentation of these species [13]. However, it is still important to adjust the distance between camera traps –the distances should be far apart enough to record an adequate number of individuals in the sampling area, but at the same time, close enough to avoid missing any individuals in the sampling area [14]. For our study, we



Figure 1. Location of the study area (Ilgaz Mountains, Çankırı Province, Turkey) - camera trap stations (F).

decided to place the camera traps approximately 5-10 km apart in order to maximize the coverage area, but kept the distance between the traps at <10 km in order to avoid missing species that have relatively small home ranges (e.g. marten species). Trap locations were fixed throughout the entire period of our study. Cameras were only replaced if one got stolen or broken for any reason.

One month prior to the beginning of our sampling efforts, we scouted the area for any possible clues indicating the presence of large mammal species (e.g. faeces, tracks). We placed the camera traps on paths and trails, where we detected and identified such clues. All cameras were positioned at 50-70 cm of height on average, and the focal range was set to 5–7 metres. All the cameras and sensors were protected with weather-resistant covers mounted on rigid vegetation. We visited the traps every month in order to get the captured visuals and to check if battery replacement was necessary. By using Garmin GPSMAP 60 CSX (Garmin International, Inc., Olathe, KS, USA), we recorded the geographic positions of all camera trap stations and plotted them (Fig. 1). The triggering mechanism for camera traps relied on sensors that can detect heat and/or motion within the range of a conical infrared beam. An approximate lag of 0.3 seconds was observed from the time the sensor detects an animal and the time the camera is triggered. Consecutive shots had a 10 second delay in between.

Data Analysis

We assumed that consecutive photographs of a specific species taken by the same camera trap in a relatively short period [within 1 hr; 15, 16] represented the same individual, keeping in mind that some species may linger around or in front of a camera for longer periods. Therefore, we filtered all such multiple visuals belonging to target species, and evaluated them as a single “record.” Photographs displaying a group containing individuals of the same species were also evaluated as single records for the given species. The capture rates for species were calculated by considering the number of records taken in 100 camera trap days (CTD), and this value was called the relative capture frequency (RCF). These RCF values were then used in determining the distribution patterns (random, regular, or clustered) of all species targeted within the area of study. To demonstrate the significant variations in the number of records among different camera trap stations for a given species, we performed χ^2 tests.

The number of records taken at different hours in a day was assumed to reflect the daily activity preferences of target species. To describe these activity patterns for all target species, we used the timestamps on the records. We then analysed these activity preferences by tabulating the

number of records for all species in 2-h intervals. In order to come up with results that can be evaluated as statistically significant, we performed this analysis only for species with the adequate number of records [17]. The records were later classified into three different daily activity preference groups (diurnal, nocturnal, or crepuscular) depending on the capturing period. The species were assumed to be diurnal if the records were taken during 06:00–17:59, nocturnal if the records were taken during 18:00–05:59, and crepuscular if the records were taken during 04:00–07:59 or 16:00–19:59. We performed χ^2 tests to determine the significant differences in the number of records belonging to particular daily activity preference groups for all our target species. The significance level was determined by using an α value of 0.05.

All statistical analysis and graphs were made by STATISTICA (v. 8.0; StatSoft, Inc., Tulsa, OK, USA).

RESULTS

We distributed the observation effort among camera trap stations according to how many days each one worked for (CTDs); F1: 142 (23%), F2: 120 (19%), F3: 96 (16%), F4: 121 (19%), and F5: 142 (23%). The total sampling effort of 621 CTDs yielded 311 independent camera trap records for further analysis, after filtering our photographs as described under the data analysis section. Among these 311 records, we found that 58% of the records (180 out of 311) belonged to the target species, whereas 42% (131 out of 311) were photographs of domestic animals, humans, small mammals, birds, and reptiles.

In the study area, we ended up capturing the photographs of 9 different species of large terrestrial mammals (see appendices for their photographs). Among our target species, the most frequently recorded was hare (101 times; 56.11% of all the records belonging to all target species), followed by roe deer (19 times; 10.56%) and bear (19 times; 10.56%), red deer (12 times; 6.67%) and lynx (12 times; 6.67%), wolf (nine times; 5%), boar (four times; 2.22%), badger (twice; 1.11%), and fox (twice; 1.11%). Table 1 shows the RCF values for each species, and how many days it took a trap to capture that species in the study area (first capture day: FCD).

Table 2 showed the distribution of RCF values for each species among all camera trap stations during the entire study period. The comparison of these values among camera trap stations gave statistically significant differences for hare and roe deer ($\chi^2=134.20$; $\chi^2=37.05$, respectively; $df=4$; $p<0.05$), but the comparison for all other species proved to be statistically insignificant ($p>0.05$).

We determined a statistically significant difference in the number of records taken during three designated daily

Table 1. Number of records, RCF values, and first capture days of target species.

| Order | Species | | Number of Records | RCF* | FCD* |
|-----------------|---------------|--------------------------------------|-------------------|-------|------|
| | English Name | Latin Name | | | |
| Lagomorpha | European hare | <i>Lepus europaeus</i> Pallas, 1778 | 101 | 16.26 | 2 |
| Carnivora | Brown bear | <i>Ursus arctos</i> L. 1758 | 19 | 3.06 | 13 |
| | Wolf | <i>Canis lupus</i> L. 1758 | 9 | 1.45 | 43 |
| | Red fox | <i>Vulpes vulpes</i> (L. 1758) | 2 | 0.32 | 121 |
| | Eurasian lynx | <i>Lynx lynx</i> (L. 1758) | 12 | 1.93 | 52 |
| | Badger | <i>Meles meles</i> (L. 1758) | 2 | 0.32 | 38 |
| Cetartiodactyla | Wild boar | <i>Sus scrofa</i> L. 1758 | 4 | 0.64 | 30 |
| | Red deer | <i>Cervus elaphus</i> L. 1758 | 12 | 1.93 | 18 |
| | Roe deer | <i>Capreolus capreolus</i> (L. 1758) | 19 | 3.06 | 43 |
| Total | | | 180 | 28.98 | |

*RCF: Relative capture frequency, FCD: First capture day

activity preference periods for hare, lynx, wolf, boar, and fox ($\chi^2=108.59$; 200.02; 107.43; 200.02; 200.02; $df=2$; $p<0.05$, respectively), and this was interpreted as an indication that these five species were nocturnal. Camera traps yielded an equal number of records during all periods for badger; and there was no statistically significant difference in number of records taken during each period for bear, red deer, and roe deer ($p>0.05$, Table 3).

We analysed the daily activity patterns of carnivorous large mammals that were recorded at least nine times. The results revealed that bear was active from 12:00 to 08:00, frequently between 22:00 and 04:00; that lynx preferred being active during 20:00–00:00 and from 02:00 to 04:00; and that wolf was active both from 20:00 to 02:00 and from 04:00 to 08:00 (Fig. 2).

Table 2. Distribution of RCF values for each species among all camera trap stations

| Species | Camera Trap Stations | | | | | Total |
|---------------|----------------------|-------|-------|-------|------|-------|
| | F1 | F2 | F3 | F4 | F5 | |
| European hare | 0.70 | 9.17 | 66.67 | 19.00 | 1.41 | 16.26 |
| Roe deer | 2.82 | 0.00 | 0.00 | 11.57 | 0.70 | 3.06 |
| Brown bear | 2.11 | 1.67 | 2.08 | 7.44 | 2.11 | 3.06 |
| Red deer | 1.41 | 0.83 | 4.16 | 1.65 | 2.11 | 1.93 |
| Eurasian lynx | 1.41 | 3.33 | 5.20 | 0.83 | 0.00 | 1.93 |
| Wolf | 0.70 | 5.00 | 1.04 | 0.00 | 0.70 | 1.45 |
| Wild boar | 0.00 | 1.67 | 0.00 | 0.00 | 1.41 | 0.64 |
| Badger | 0.00 | 0.00 | 1.04 | 0.83 | 0.00 | 0.32 |
| Red fox | 0.00 | 0.83 | 0.00 | 0.00 | 0.70 | 0.32 |
| Total | 9.15 | 22.50 | 80.21 | 41.32 | 9.15 | 28.98 |

Daily activity patterns of herbivorous large mammals, on the other hand, were analysed for species that had a minimum of 10 records. These results revealed a consistent presence of roe deer and red deer during all time periods, showing no clear preference for a specific activity pattern; whereas hare was active from 20:00 to 08:00, frequently between 20:00 and 04:00 (Fig. 3).

Although we did not encounter any nests belonging to any of the large mammal species during our study, our camera traps captured photographs of the cubs of several target species (Fig. 4).

DISCUSSION AND CONCLUSION

We revealed by evaluating the camera trap data that the habitat provided suitable habitats for large mammals sin-

Table 3. Daily activity preferences of the target species.

| Species | Daily Activity Preference* | | |
|---------------|----------------------------|---------|-------------|
| | Nocturnal | Diurnal | Crepuscular |
| European hare | 88.12 | 11.88 | 20.79 |
| Roe deer | 42.11 | 57.89 | 52.63 |
| Brown bear | 74.68 | 26.32 | 31.58 |
| Red deer | 75.00 | 25.00 | 50.00 |
| Eurasian lynx | 100.00 | 0.00 | 0.00 |
| Wolf | 88.89 | 11.11 | 33.33 |
| Wild boar | 100.00 | 0.00 | 0.00 |
| Badger | 50.00 | 50.00 | 50.00 |
| Red fox | 100.00 | 0.00 | 0.00 |

*Percentages (%) for daily activity patterns

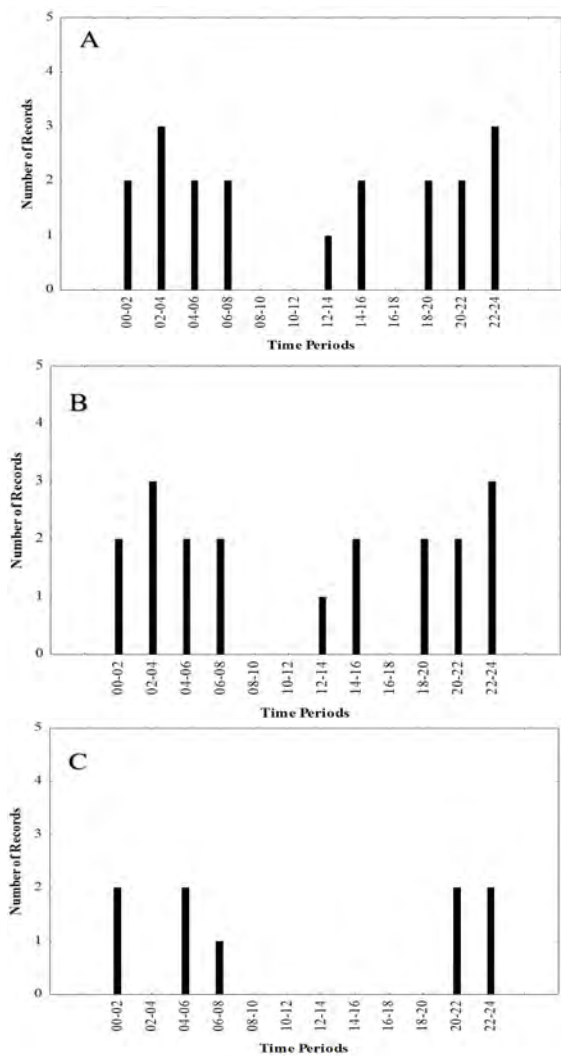


Figure 2. Daily activity patterns of carnivorous large mammals with minimum nine records: brown bear (A), Eurasian lynx (B), and wolf (C). The number of records from all five stations are shown with bars for each period.

ce we observed several large mammal species with high ecological requirements. This was the first time that a systematic camera trap study recorded the presence of hare, bear, wolf, fox, lynx, badger, boar, red deer, and roe deer in the Ilgaz Mountains. We determined that at least five of these species bred in the area, as indicated by the photographs of their cubs captured by our camera traps, further supporting the assumption about the area's potential importance.

Among the species we targeted were marten species, jackal, and wild cat, but we could not capture any of them. The questionnaire surveys conducted with the local people pointed out that no findings on the presence of jackals in the region. Accordingly, we did not encounter a single clue to indicate a jackal's presence during our field studies. Nevertheless, we identified footprints and faeces belonging to at least one marten species during our study, and encountered

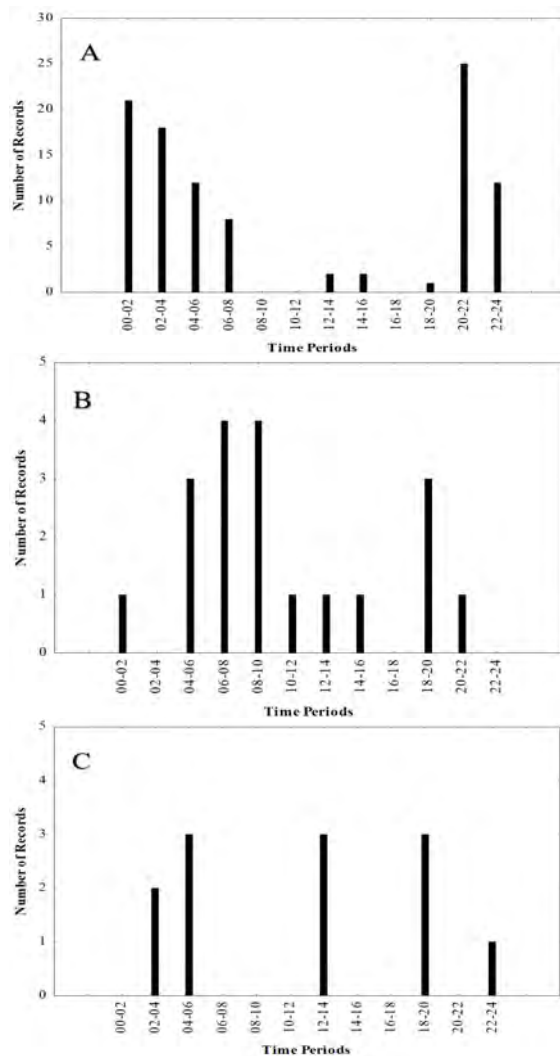


Figure 3. Daily activity patterns of herbivorous large mammals with minimum ten records: European hare (A), roe deer (B), and red deer (C). The number of records from all five stations are shown with bars for each period.

a wild cat in close proximity of the area. Photograph capturing rates may be affected by the animal size, as reported in recently conducted studies [13]. For our study, we placed the camera traps approximately 50 cm above the ground level in order to ensure capturing the species with large body sizes. This precaution, in return, might have led to missing the relatively smaller and rare species like marten and wild cat, both of which can move faster than other large mammals in the study area.

Hare was known to occur in almost all Turkey [18, 19]. In this study, it was the most common species with 101 records, and it took only two days for our cameras to capture this species. Unexpectedly, boar and fox, which were known to be two other common species in Anatolia [18], were encountered with much lower frequency in the area. Fox was also the last captured large mammal species (after 121 days). The low density of human population in the study area, and

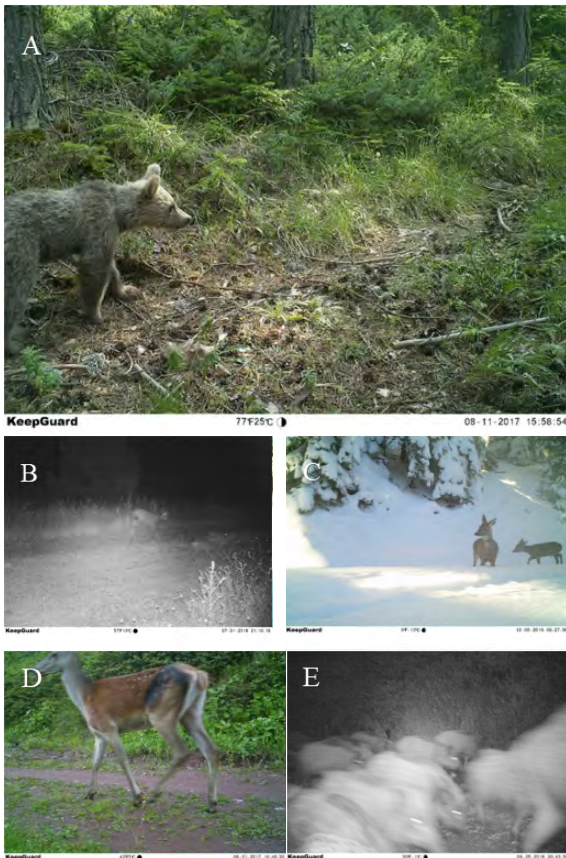


Figure 4. Cubs of target animals recorded during the study: brown bear (A), Eurasian lynx (B), roe deer (C), red deer (D), and wild boar (E).

therefore a significant lack of anthropogenic factors, might have encouraged sensitive species such as bear, lynx, and wolf to use the area more comfortably for feeding and breeding. Lynx preys on foxes [20], although their encounters did not always end with foxes being eaten [19]. Fox, by its generalist nature, can exploit resources efficiently in a variety of habitats, and could move to a different habitat in order to avoid predators that were relatively larger than itself [21]. We claimed that foxes dispersed to regions closer to human settlements located elsewhere, possibly due to the presence of bear, lynx, and wolf in the study area. The best possible explanation for the low RCF for boar was the predation by wolves [22]. Other reasons affecting the RCF values for boar might be the difference in climate (and accordingly, the availability of food), certain diseases, or hunting exploitation - although hunting was prohibited in the majority of the region.

Even though Tobler et al. [23] proposed that the abundance of a species might affect its RCF values, this correlation might not be useful for comparing the relative abundance of different species. This was due to numerous reasons including the relationship between the size of a species and the probability of a camera trap to capture this species, as well as differences in behaviour or home range size among

species. Therefore, the RCF values we obtained during our study could not be used as actual indicators to make a deduction regarding the abundance of a species in comparison with others in the study area. The RCF values of species were used only for determining if they had random, regular, or clustered distribution in the study area. Roe deer and hare were evaluated to show clustered distributions in the region. Roe deer was concentrated particularly in Eksik village (Ilgaz district, F4 camera trap station), using this area especially in the post-breeding period. Hare was observed to intensely use the open lands inside the forest area between Kırışlar and Kayı villages (Ilgaz district, F3 camera trap station). The distributions of other target species were relatively homogeneous throughout Ilgaz Mountains, which extend approximately 60 km into Çankırı province.

We determined that wolves, lynxes, and hares showed similar activity preferences. The majority of the activities of these three species took place during the night; while bear, red deer, and roe deer showed activity in both daytime and twilight (fox, badger, and boar records were not analysed due to insufficient number of data). As we did not have a single capture for lynx during day hours, we could indicate that it was a strictly nocturnal species. The daily activity preference of lynx was indisputably related to its hunting behaviour [24]. As shown in recent studies, the primary prey of Anatolian populations of lynx was hare [25, 26]. Thus, it makes sense that the activity periods preferred by lynx were in correlation with the nocturnal habits of its primary food source. Wolf was thought to have accommodated nocturnal behaviour in order to avoid encountering humans [19, 27], and the findings of our study also supported this.

The study area, along with the surrounding regions, was not subjected to heavy human activity. The region hosts very little human settlement. As a result, a good amount of high vegetation covers as well as abundant food might play a role in making the study area a favourable habitat for this cryptic species –indicators for the area's ecological significance. Our results provided scientific data and insight for future conservation efforts and management studies concerning the large mammal species in Ilgaz Mountains. Noteworthy records of large mammal species from the study area signified both the importance of our study, and the necessity of better management plans to ensure efficient protection of the region and the species it hosts.

ACKNOWLEDGEMENT

Camera traps and legal permissions were provided by The Ministry of Agriculture and Forestry, General Directorate of Nature Protection and National Parks (Turkey), and Çankırı Provincial Directorate of Nature Protection and National Parks. We are grateful to DOKAY

Environmental Consultancy Company for providing the necessary support to realize this study, as well as our colleagues Dr. Tarkan Yorulmaz and Dr. Barış Özüdoğru for their assistance in the field. This study was supported by Hacettepe University's Scientific Research Projects Coordination Unit (Project Number: FHD-2017-13111).

References

- Chiarello AG. Density and population size of mammals in remnants of Brazilian Atlantic Forest. *Conservation Biology* 14, no. 6 (2000) 1649–1657.
- Gordon IJ. Restoring the functions of grazed ecosystems, in: Danell K, Bergström R, Duncan P, Pastor J (Eds.). *Large herbivore ecology, ecosystem dynamics and conservation*, Cambridge University Press, New York, pp. 449–467, 2006.
- Sinclair ARE, Mduma S, Brashares JS. Patterns of predation in a diverse predator – prey system. *Nature* 425 (2003) 288–290.
- Dalerum F, Somers MJ, Kunkel KE, Cameron EZ. The potential for large carnivores to act as biodiversity surrogates in southern Africa. *Biodiversity and Conservation* 17, no. 12 (2008) 2939–2949.
- Rocha EC, Brito D, Silva PM, Silva J, Bernardo PVS, Leandro J. Effects of habitat fragmentation on the persistence of medium and large mammal species in the Brazilian Savanna of Goiás State. *Biota Neotropica* 18, no. 3 (2018) e20170483.
- Cheyne SM, Sastramidjaja WJ, Muhalir, Rayadin Y, Macdonald DW. Mammalian communities as indicators of disturbance across Indonesian Borneo. *Global Ecology and Conservation* 7 (2016) 157–173.
- Andrade-Núñez MJ, Mitchell Aide T. Effects of habitat and landscape characteristics on medium and large mammal species richness and composition in northern Uruguay. *Zoologia* 27, no. 6 (2010) 909–917.
- Can ÖE, Togan I. Camera trapping of large mammals in Yenice Forest, Turkey: local information versus camera traps. *Oryx* 43, no. 3 (2009) 427–430.
- Akman Y, Yurdakulol Y, Demirörs M. The vegetation of the Ilgaz Mountains. *Ecologia Mediterranea* IX, no. 2 (1983) 137–165.
- Akman Y. İklim ve Biyoiklim, Palma Yayın Dağıtım, Ankara, 1990.
- T.C. Çankırı Valiliği Çevre ve Şehircilik İl Müdürlüğü. Çankırı İli 2016 Yılı Çevre Durum Raporu, Çankırı, 2017.
- Dillon A, Kelly MJ. Ocelot (*Leopardus pardalis*) in Belize: the impact of trap spacing and distance moved on density estimates. *Oryx* 41, no. 4 (2007) 469–477.
- Kelly MJ. Design, evaluate, and refine: camera trap studies for elusive species. *Animal Conservation* 11 (2008) 182–184.
- MEEK PD, Ballard G, Claridge A, Kays R, Moseby K, O'Brien T. Recommended guiding principles for reporting on camera trapping research. *Biodiversity and Conservation* 23, no. 9 (2014) 2321–2343.
- Bowkett AE, Rovero F, Marshall AR. The use of camera trap data to model habitat use by antelope species in the Udzungwa Mountain forests, Tanzania. *African Journal of Ecology* 46, no. 4 (2007) 479–487.
- Rovero F, Marshall AR. Camera trapping photographic rate as an index of density in forest ungulates. *Journal of Applied Ecology* 46, no. 5 (2009) 1011–1017.
- Sanderson JG. Camera phototrapping monitoring protocol, The Tropical Ecology, Assessment and Monitoring (TEAM) Initiative, The Center for Applied Biodiversity Science, Conservation International, Washington, DC, pp. 18, 2004.
- Demirsoy A. Türkiye Omurgalıları: Memeliler, Çevre Bakanlığı,

- Çevre Koruma Genel Müdürlüğü, Meteksan A.Ş., Ankara, pp. 292, 1996.
- Aulagnier S, Haffner F, Mitchell-Jones AJ, Moutou F, Zima J. *Mammals of Europe, North Africa and the Middle East*, Delachaux et Niestle SA, Paris, pp. 272, 2008.
 - Jobin A, Molinari P, Breitenmoser U. Prey spectrum, prey preference and consumption rates of Eurasian lynx in the Swiss Jura Mountains. *Acta Theriologica* 45, no. 2 (2000) 243–252.
 - Fedriani JM, Palomares F, Delibes M. Niche relations among three sympatric Mediterranean carnivores. *Oecologia* 121, no.1 (1999) 138–148.
 - Jedrzejewska W, Jedrzejewska B, Okarma H, Schmidt K, Zub K, Musiani M. Prey selection and predation by wolves in Białowieża Primeval Forest, Poland. *Journal of Mammalogy* 81, no.1 (2000) 197–212.
 - Tobler MW, Carrillo-Percegué SE, Leite Pitman R, Mares R, Powell G. An evaluation of camera traps for inventorying large and medium sized terrestrial rainforest mammals. *Animal Conservation* 11, no. 3 (2008) 169–178.
 - Jedrzejewski W, Schmidt K, Milkowski L, Jedrzejewska B, Okarma H. Foraging by lynx and its role in ungulate mortality: the local (Białowieża Forest) and the Palearctic viewpoints. *Acta Theriologica* 38, no. 4 (1993) 385–403.
 - Mengüllüoğlu D, Ambarlı H, Berger A, Hofer H. Foraging ecology of Eurasian lynx populations in southwest Asia: Conservation implications for a diet specialist. *Ecology and Evolution* 8, no. 6 (2018) 9451–9463.
 - Soyumert A, Ertürk A, Tavşanoğlu Ç. The importance of lagomorphs for the Eurasian lynx in Western Asia: Results from a large scale camera-trapping survey in Turkey. *Mammalian Biology* 95 (2019) 18–25.
 - Theuerkauf J, Jedrzejewski W, Schmidt K, Okarma H, Ruczynski I, Sniezko S, Gula R. Daily patterns and duration of wolf activity in the Białowieża Forest, Poland. *Journal of Mammalogy* 84, no.1 (2003) 243–253.

APPENDIX

Record samples of large mammal species captured during the study: 1. *Ursus arctos*, 2. *Canis lupus*, 3a-3b. *Lynx lynx*, 4. *Vulpes vulpes*, 5. *Meles meles*, 6. *Capreolus capreolus*, 7. *Cervus elaphus*, 8. *Sus scrofa*, 9. *Lepus europaeus*.





